ON THE ORIGIN OF CLOSE-RANGE *E* REGION ECHOES OBSERVED BY SUPERDARN HF RADARS IN THE MID- AND HIGH LATITUDES

A Thesis Submitted to the
College of Graduate Studies and Research
in Partial Fulfillment of the Requirements
for the degree of Doctor of Philosophy
in the Department of Physics and Engineering Physics
University of Saskatchewan
Saskatoon

By
Blessing Iserhienrhien

©Blessing Iserhienrhien, 2016. All rights reserved.

Permission to Use

In presenting this thesis in partial fulfilment of the requirements for a Postgraduate degree from the University of Saskatchewan, I agree that the Libraries of this University may make it freely available for inspection. I further agree that permission for copying of this thesis in any manner, in whole or in part, for scholarly purposes may be granted by the professor or professors who supervised my thesis work or, in their absence, by the Head of the Department or the Dean of the College in which my thesis work was done. It is understood that any copying or publication or use of this thesis or parts thereof for financial gain shall not be allowed without my written permission. It is also understood that due recognition shall be given to me and to the University of Saskatchewan in any scholarly use which may be made of any material in my thesis.

Requests for permission to copy or to make other use of material in this thesis in whole or part should be addressed to:

Head of the Department of Physics and Engineering Physics
163 Physics Building
116 Science Place
University of Saskatchewan
Saskatoon, Saskatchewan
Canada
S7N 5E2

Abstract

The Super Dual Auroral Radar Network (SuperDARN) is a global network of coherent high frequency (HF) radars located in the polar, high- and mid-latitudes of both the Northern and Southern hemispheres. This thesis deals with close-range SuperDARN echoes (oblique HF backscatter from the lower part of the ionosphere). The aim of this thesis is to shed light on the origin of these echoes. Previous studies have been content to propose explanations for the origin of these echoes without thorough checking of the proposed mechanisms against constraints available from various radars and other important information. For the purpose of clarifying the situation, a chain of SuperDARN radars in the Northern and Southern hemispheres and several years of daily statistics have been used. This has allowed for several findings. Notably, the close-range SuperDARN echoes show diurnal and seasonal variations and their properties with respect to signal-to-noise-ratio, Doppler velocity and Doppler width vary. Three distinct populations of close-range HF backscatter have been established: (1) a morning population (0400–0700 LT), (2) a midday summer population (0800–1300 LT) and (3) a pre-midnight (2100–2300 LT) population. The morning population is associated with meteor trails which are observed to be peaking near local dawn as expected, and already suggested by previous research. High latitude SuperDARN radars also had echoes (pre-midnight population) with higher Doppler velocities than the others yet the Doppler velocities are smaller than that expected from auroral E region echoes. Given the time and location of this population of echoes, it has been concluded that they are a special class of high latitude E region echoes at high aspect angle which have been termed "high aspect irregularity region" echoes in the past. Lastly, the midday summer population was found to be too high for polar mesosphere summer echoes and too early for plasma instabilities. It is proposed that these SuperDARN echoes are produced either from contribution from meteors trails or by neutral turbulence which is suspected (from other work) to be present near 100 km. The properties of the midday summer population resembles those of meteor trails as they have the same power, and the same altitude and have high summer occurrence as expected for meteors. Their late morning occurrence could be due to particular look direction of individual radars which may change the occurrence statistics in the presence

of meteor showers. With respect to neutral turbulence, the drift of the midday summer population is similar to that of neutral wind.

Acknowledgements

I want to first thank Prof. Jean-Pierre St.-Maurice especially for his advice and guidance in the course of my studies and for helping me understand the necessaryphysics of the ionosphere and the operations of the radar system. I am most grateful to him for his constant kindness, enthusiasm, informative assistance and helpful suggestions during my Ph.D program. His outstanding patience in supervision and guidance have been invaluable! Without his support and generous funding for this research, this thesis would not have been completed and for all these I am forever grateful!

I would like to also thank Dr. Pasha Ponomarenko for his continual help during this entire work. His support in helping me understand the physics of the ionosphere as well as the SuperDARN radar operations and also the physics behind its operation is greatly appreciated! Also, I thank him for his invaluable technical support with respect to programming. His patience in discussing programming techniques is deeply appreciated!

I thank my Advisory Committee members, Prof. Alan Manson, Prof. Tom Steele, Prof. Raymond Spiteri for their helpful suggestions, comments, advice and guidance.

I am much indebted to Dr. Jean-Baptiste Kikwaya and Dr. Mohammed Kedir Osman for their timely advice and motivation to "never give up". Their encouragements and genuine concern towards me and my academic life have been of great help and are forever cherished!

I greatly appreciate the support and assistance of Dr. Dieter André for his technical assistance, and the informative discussion and help in understanding of SuperDARN radar operations. The concern shown to me by Cindy Jelinski will never be forgotten. Her genuine concern shown by asking *"How are you doing?"* (academically and/or healthwise) brightens my everyday with smiles and I am grateful for her empathy! Thanks to Dr. Kathryn McWilliams for appointing me as one of her Teaching Assistants (TA) in the General Engineering (GE) labs. The opportunity to supervise those laboratory classes built up my confidence in lecturing and improved my teaching skills. The added TA hours that GE labs provided have really helped me a lot when things were rough. I appreciate that.

My thanks also go to the entire members of the Institute of Space and Atmospheric Studies, especially the SuperDARN group at the University of Saskatchewan, for making

my workplace an academic and friendly atmosphere to work in. I would like to thank the department of Physics and Engineering Physics department for the various funding provided through scholarships and/or Graduate Teaching opportunities. Thank you Debbie Parker and Marj Granrude for being my friends and also for your administrative support and assistance in providing the required degree information and right documentation. Thanks to Dr. Stan Shadick, Laverne Sander and Brian Zulkoskey for all the Physics and Engineering Physics laboratory training.

Special thanks go to a number of friends and colleagues who have turned family: Dr. Oluyele Makinde and family, Dr. Elmarie Du Toit, Dr. Ivan Teofilov, Mariana Teofilov, Bassey Bassey and family, Sandeep Kaur Litt, Zahra Abooalizadeh, Adeola Igbalojobi, Gail Paquette and family, Nelly Musamu, Donatien Musamu, Funmi and Tope Owoeye, Philomena Johnson, Rachel Ngnitang, Prof. Kanthi Kaluarachchi, Clara Buma, Jodi Guthrie, Dan Okezie, Tsola Ekpokai and family, Fedelia (UD) and Fred Uwaechie, Lanre and Juliana Gidado, Kenneth K. E. Ziegler (LLP), Karl W. Martens (LLP) and Nikunj I. Mistry for immigration issues. I appreciate all your friendship, help and assistance.

Finally, I owe it to my entire loving family - my late father, Mathew Aiyamenkhue Iserhienrhien, my mother, Margaret Enorongho Iserhienrhien, my husband, Dr. Joseph Chinye Obirai, and my siblings (and their spouses): Dr. Ruth Iserhien-Emekeme (a.k.a Aunty) (and Lucky Oghenovo Emekeme), Sarah Iserhien-Ezenwa (and Ezra Ezenwa), Endurance Aiyamenkhue (and Gonny Hazelhoff), Rebecca Ojobor (and Karo Ojobor), Racheal Izebvuwa (and Michael Izebvuwa), Amos Aiyamenkhue (and Winifred Aiyamenkhue) and Abigail Iserhienrhien. Thanks to my nieces and nephews: Kadmiel Emekeme, Keziah Emekeme, Keren-happuch Emekeme, Kemuel Emekeme, Endurance (Jr.) Aiyamenkhue, Faith Aiyamenkhue, Jason Ojobor, Lemuel Aiyamenkhue and Amaziah Izevbuwa, for always being ready to talk to me on the phone and telling me that they miss me and want me to visit home in Nigeria. Thanks to them all for their invaluable moral support, tolerance and understanding throughout the course of my education in Canada. I would never have been here without the love and support shown over the years. When times were tough for me, you all stood by me and always encouraged me to keep my head high with my chin up. I am grateful for everything! My thanks also go to my paternal and maternal uncles, Dr.

Francis Omoruyi (in Toronto) and Dr. Osadiaye Osadolor (a.k.a. DEWOSCO - in Nigeria) respectively for standing by me before coming to Canada for my Masters and also while in Canada. When I was refused visa in the year 2006, you both stood by me and motivated me not to give up, but apply again, and you also urged my family to take a lawyer in Canada to appeal and support my new application for a study permit. And because of the appeal by the lawyer, I was eventually granted a Canadian visa and my Study Permit was issued. I am most grateful for everything. May God bless you all and I love you all!

Dedication

To Jehovah God, the Giver and Preserver of my Life

To my Father and Mother

Contents

List of Tables

List of Figures

List of Abbreviations

ACF	autocorelation function
CVE	Christmas Valley East
CVW	Christmas Valley West
EISCAT	European Incorent Scatter Scientific Association
EUV	extreme ultraviolet
FAI	field-aligned-irregularities
FB	Farley-Buneman
FHE	Fort Hays East
FHW	Fort Hays West
FOV	field-of-view
GD	Gradient Drift
GNRE	Grainy Near Range Echoes
HAIR	high aspect irregularity region
HF	high frequency
INV	Inuvik
KH	Kelvin-Helmholtz
LOS	line-of-sight
LT	local time
MST	mesosphere-stratosphere-troposphere
MLT	mesosphere ad lower thermosphere
NLC	noctilucent clouds
NRE	near-range echoes
PGR	Prince George
PMSE	Polar Mesosphere Summer Echoes
PolarDARN	Polar Dual Auroral Radar Network
RG	range gate
RKN	Rankin Inlet
UHF	ultra high frequency
UV	ultraviolet
UT	Universal Time
SAS	Saskatoon
SNR	signal-to-noise-ratio
SOUSY	SOUnding SYstem
SuperDARN	Super Dual Auroral Radar Network
TIG	TIGER
TIGER	Tasman International Geospace Environment Radars

Chapter 1

INTRODUCTION

The region of the Earth's atmosphere with a "significant " number of ionized particles is referred to as the ionosphere. The ionosphere is often structured and these structures are usually field-aligned. The structures range from small-scale size of a few centimeters to large-scale of tens of kilometers. Between 100 and 120 km, these structures or field-aligned-irregularities (FAI) are produced by plasma instabilities. The high mobility of electrons along the magnetic field is responsible for the field alignment. This means that plasma instabilities only have a chance to grow with fairly modest departures from equilibrium if they are FAI, that is, highly extended along the magnetic field.

The scattering of radio waves is the most common means of observing the ionospheric irregularities. Radio waves can cover large areas and provide high time resolution of the ionosphere. The radar technique involves transmitting radio waves into the ionosphere. In the most standard geometry, radars detect radio waves backscattered from the ionospheric irregularities. The signals received as wavefronts from each irregularity are weak, but because there are many of them, the signals from parallel structures can all contribute coherently so that a strong enough signal may be detected (below noise level). The Super Dual Auroral Radar Network (SuperDARN) system of coherent high frequency (HF) radars is the main instrument used for the present study. SuperDARN radars are high frequency (8-12 MHz) "coherent-scatter radars" with backscatter from the E and F regions of the ionosphere. The radars from an international network are capable of providing broad latitudinal coverage from mid to high latitude in both the Northern and Southern Hemispheres, with appropriate variation in longitude. The operations of the radars are based on a single design and run coordinated observational sequences with standard data processing techniques, which in turn ensures consistency in data between the instruments (*Arnold et al.*, 2001).

As eluded above, SuperDARN normally detects field-aligned-irregularities (FAI). High frequency is used by SuperDARN because we wish to study FAI at high latitudes where the magnetic fields are nearly vertical. That means that reasonably strong refraction is required in order to bend the rays as they approach the structures, so as to hit perpendicularity to the magnetic field. Not only must SuperDARN look obliquely, but it also needs to be in the HF range.

Besides the ionospheric backscatter (or echoes) from ranges beyond 500 km, an unexpected class of ionospheric reflections, known as close-range echoes, have been observed for a long time from the beginning of operations of individual radars. These close-range echoes also must occur in the lower part of the ionosphere. In this work, the terms "close-range", "near-range" and "short-range" are somewhat used interchangeably. These echoes are detected very frequently and independently in the first 3 range gates (<500 km) of the SuperDARN radars. These structures generating near-range echoes are likely not field-aligned, as the range is too close for ionospheric refraction to be sufficient to bend the HF signal to achieve perpendicularity with the magnetic field.

Hall et al. (1997) suggested that at least some of the near-range echoes (NRE) are from meteor trails. The way that works is that there is a long trail of ionization inherent in the meteor with a radius that is comparable to the wavelength of the radar. This produces Bragg scattering, but in this case, the structures are not field-aligned. Meteor trails, as expected, peak by 0600 local time (*Hall et al.*, 1997). However, other studies have reported close-range echoes in the evening and in the middle of the day. For the evening case, studies have shown that when the geometry of the experiment does not allow FAI to be detected, the auroral regions will sometimes provide echoes that are not as strongly field-aligned as the stronger echoes. This particular case of echoes have been termed *high aspect irregularity region* (HAIR) echoes (*Milan et al.*, 2004). The midday echoes observed in summer have been attributed to polar mesosphere summer echoes (PMSE) (*Hosokawa et al.*, 2005; *Ogawa et al.*, 2002) since PMSE are observed from zenith looking (vertical incidence) radars. From other radars systems looking at the zenith, this type of echoes would come from 80 to 90 km altitude, by contrast with reflections from meteor trails which are from higher altitudes. However, recalling that SuperDARN looks obliquely, the altitude of the SuperDARN midday

summer echoes has never been verified and the notion that they are PMSE has never been systematically checked in other ways either, for instance by comparing results from radars at various latitudes. A systematic study will allow direct identification and comparative analysis of different backscatter populations.

1.1 Thesis Objectives and Outline

This thesis has for its purpose clarification of the origin of near-range echoes by considering a large statistical data base using chains of radars; also by using interferometry to query the altitude of the oblique NRE seen by SuperDARN. It aims to establish whether or not NRE are formed by the three mechanisms that have been brought up in the past or if there is a need to come up with different explanations for them, based on various properties seen in the observations. To accomplish the above, the following are carried out:

1. Investigation of the diurnal and seasonal dependence of close-range HF echo occurrence in various radar stations. That is, for different seasons, what is the pattern or morphology of echo occurrence with respect to time? We also want to investigate the difference in echo occurrence between the polar cap radars, (PolarDARN- Rankin Inlet, Inuvik and Clyde River), high latitudes radars (e.g. Saskatoon and Prince George), and lower mid-latitude radars (e.g. Fort Hays East and West, Christmas Valley East and West). Results from a Southern hemisphere radar are also considered. Any relationship observed between the radars will be studied and discussed.

2. Compare and note any differences in echo detection rate for radars whose antennas are directed at different directions. The properties of NRE with respect to their signal-to-noise-ratio, Doppler velocity and spectral width are also to be considered. In this sense, we will determine criteria for identifying the SuperDARN close-range HF echoes.

3. Investigation of the altitude distribution of NRE (with respect to where they originate). Thus the study/investigation includes the estimation of the height of close-range HF echoes.

In order to put the study in proper context, the present introductory Chapter is followed by a description of the ionospheric medium in Chapter 2, with particular focus on the lower part of the E region of the ionosphere. The cooling mechanism that is needed to create the background atmospheric situations leading to PMSE, and which involves gravity waves originating in the lower atmosphere is also discussed in this chapter. The description of radars and how the Fourier analysis of data from the atmospheric regions that are scrutinized are discussed in Chapter 3. A brief survey of plasma instability mechanisms leading to FAI are discussed in Chapter 4, since the evolution of FAI could lead to weak echoes that are not strongly field-aligned, and might therefore be the origin of at least some of the NRE. Following that discussion, Chapter 5 describes meteor trails and how they lead to structures that are not field-aligned. Chapter 5 describes the morphology, origin and expected properties of PMSE for oblique HF radars. After these chapters on background, the thesis proceeds with a presentation of the data used for this study (in Chapter 6), followed by Chapter 7 that contains discussions of the results. The thesis ends with a summary in Chapter 8.

Chapter 2

THE IONOSPHERE AND THE UPPER ATMOSPHERE

The ionosphere is that region of the Earth's upper atmosphere, from 60 to 1000 km, that is ionized by solar radiation, resulting in a population of ions and electrons that form a plasma. Solar extreme ultraviolet (EUV), ultraviolet (UV) and x-ray radiation are primary sources of plasma and energy for the ionosphere. The impact of EUV and x-rays photons from the Sun ionize neutral atoms and molecules such as N_2, N, NO, O_2, O, H and He (*Chapman*, 1931a). The distribution of plasma densities and temperature in the ionosphere is controlled by radiative, chemical and dynamical processes (*Schunk and Nagy*, 2000). The ionosphere is composed of different regions and it is instructive to discuss their formation and origin.

2.1 Processes Shaping the Ionospheric Composition and Density Profile

A good description of the layering of the ionosphere was first discussed by Sydney Chapman in the 1920s. He developed a theory based on the simplest model of the atmosphere and the incident flux (*Chapman*, 1931a,b). The main idea behind the Chapman theory is to model the flux of solar radiation that enters the neutral atmosphere and is eventually fully absorbed by it. The radiation is absorbed by the neutral atmosphere so that an exponential density distribution with altitude results. This photoionization process continues until a depth is reached where the photoionization production drops for a lack of photons. A layer of ionization near the altitude of maximum production is created and is known as the

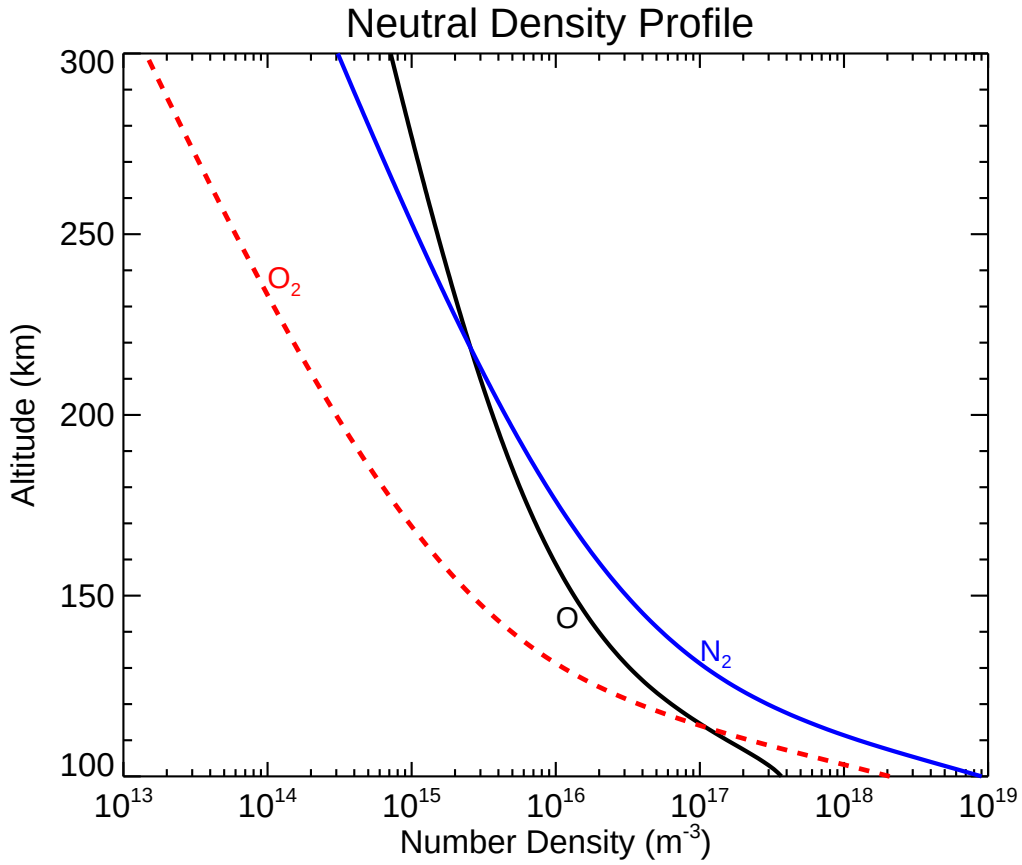

Figure 2.1: Neutral density profile for O, O_2, and N_2 plotted with respect to altitude in April 3, 2000. The data are obtained from VITMO (Virtual Ionosphere, Thermosphere, Mesosphere Observatory), with courtesy of MSIS-90 Atmospheric Model.

Chapman layer. Examples of photoionization reactions are (*Wayne*, 1991):

$$O_2 + h\nu \longrightarrow O_2^+ + e \tag{2.1}$$

$$O + h\nu \longrightarrow O^+ + e \tag{2.2}$$

$$N_2 + h\nu \longrightarrow N_2^+ + e \tag{2.3}$$

The Earth's neutral atmosphere consists mainly of O, N_2 and O_2 below 500 km. Figure 2.1 gives the distribution of these three neutrals with respect to altitude. The lower atmosphere is predominantly N_2, while O dominates atmosphere regions above 200 km. Large quantities of O_2 are only found below 105 km. The rate at which the radiation is absorbed is proportional to the neutral density and the energy of the radiation reaching that height. When the particles are ionized, they begin to recombine to once again form neutrals, at a rate determined by the density of particles at that height (*Hargreaves*, 1979).

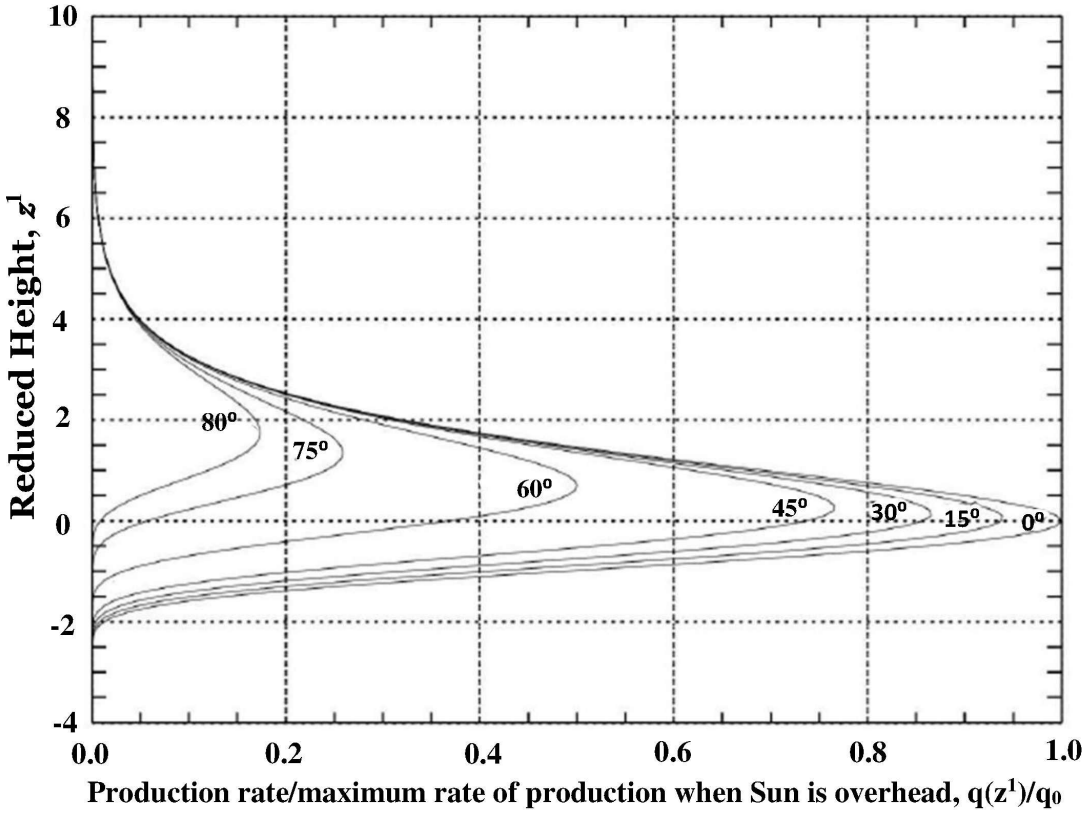

Figure 2.2: The rate of light absorption as a function of altitude using the Chapman function. The peak height of ionization rates increases with larger zenith angle, χ, but the maximum production rate decreases in the process.

A simple explanation of the Chapman theory may be theoretically given based on the following examples and the assumptions that go with it (*Hargreaves*, 1979):

1. An exponential atmosphere with only the O_2 gas component of constant scale height ($H = kT/mg$). Its photodissociation reaction can follow Equation (2.1).

2. Plane stratification.

3. Solar radiation absorption in proportion to the number density of gas particles.

4. Radiation is monochromatic with single absorbing component.

At high altitudes, few ion-electron pairs are produced because there are fewer neutrals around. As the altitude decreases, however, more ion-electron pairs are produced because there is plenty of neutrals. But because of the exponential increase in atmospheric density with decreasing altitude, there comes a point where there are so many neutrals around that

the photons are basically all absorbed (used up). Suddenly no more ion-electron pairs are formed as we go down in altitude. The production function therefore rapidly reaches a peak at an altitude just above where the photons are all used up (Figure 2.2).

To describe this process in quantitative terms, we can start with a connection between the photon flux and chemical production rates. Let us assume the photons collide with O_2 molecules so that n_{O_2} gives the density of O_2. The intensity or energy flux per unit area is $I_\lambda(\infty)$ above the atmosphere and I at altitude z, corresponding to slant distance l from the ground. For n_{O_2} absorbing atoms per unit volume, and each having an absorption cross-section σ, the intensity of the radiation is given by (*Hargreaves*, 1979):

$$\frac{dI_\lambda}{dl} \;=\; -I_\lambda \sigma n_{O_2} \tag{2.4}$$

The probability of producing molecular oxygen ions out of the interaction of the photon with an oxygen molecule is η. Therefore the rate of ionization is:

$$q \;=\; I_\lambda \sigma n_{O_2} \eta \tag{2.5}$$

If the Sun's rays are locally oblique (not overhead) and enters the atmosphere at a zenith angle χ, we must relate l to the altitude. For a flat Earth, $dl = -dz \sec\chi$. We can write Equation (2.4) (while integrating) as:

$$d \ln I_\lambda \;=\; -\sigma n_{O_2} dl \tag{2.6}$$

which results to:

$$I_\lambda \;=\; I_\lambda(\infty) e^{-\tau} \tag{2.7}$$

The optical depth is τ and is given by:

$$\tau \;=\; \sigma n_{O_2} H \sec\chi \tag{2.8}$$

Equation (2.8) is obtained from the fact that $n(z) = n_0(z_0) \exp(-z/H)$ for an isothermal atmosphere (where H is the atmospheric scale height). Therefore,

$$\int_{z_0}^{\infty} n(z) dz \;=\; n(z_0)\, H \tag{2.9}$$

For a reference height, z_0, we therefore have that:

$$n_{O_2}(z) \;=\; n_{O_2}(z_0)e^{-z'} \tag{2.10}$$

where z' is the reduced altitude given by:

$$z' \;=\; \frac{z - z_0}{H} \tag{2.11}$$

We can relate the production function, q to a function of altitude z. Let us substitute Equation (2.7) into Equation (2.5) for I_λ to obtain:

$$q \;=\; I_\lambda(z)\sigma n_{O_2}\eta \;=\; I_\lambda(\infty)\sigma n_{O_2}\eta e^{-\tau} \tag{2.12}$$

Next, let us choose z_0 such that $\tau = 1$ at z_0. Hence, Equation (2.8) becomes:

$$\sigma n_{O_2}(z' = 0)H \sec\chi \;=\; 1 \tag{2.13}$$

In that case, we can substitute Equations (2.10) and (2.13) into Equation (2.12), obtaining this:

$$q \;=\; I_\lambda(\infty)\sigma n_{O_2}(z' = 0)\eta \exp\left(-z' - e^{-z'}\right) \tag{2.14}$$

Note that

$$q(z' = 0) \;=\; I_\lambda(\infty)\sigma n_{O_2}(z' = 0)\eta\, e^1 \tag{2.15}$$

Therefore,

$$q(z') \;=\; q(0)\exp\left(1 - z' - e^{-z'}\right) \tag{2.16}$$

This is the Chapman function. It has the shape presented in Figure 2.2. Typically, the production rate is limited by a lack of ionization molecules at high altitude and a lack of ionizing radiation at low altitude. It can be shown that the electron density in a Chapman layer varies with height and solar zenith angle as the square root of the ion production q. To show this, we use the *continuity equation* which gives the density, n, of a species:

$$\frac{\partial n}{\partial t} + \frac{\partial nv}{\partial z} \;=\; q \;-\; L \tag{2.17}$$

The second term on the left hand side of Equation (2.17) is the diffusion flux. The rate of recombination, L can be written as:

$$L \;=\; \alpha_{rc}n^2 \tag{2.18}$$

where α_{rc} is the recombination coefficient. Ignoring transport by diffusion, equilibrium is reached when a balance exist between the production and loss processes, and the steady state continuity equation (Equation (2.17)) becomes:

$$\frac{\partial n}{\partial t} = 0 = q - \alpha_{rc} n^2 \tag{2.19}$$

Therefore at equilibrium,

$$q = \alpha_{rc} n^2 \tag{2.20}$$

and thus,

$$n = \sqrt{q/\alpha_{rc}} \tag{2.21}$$

where q is given by the Chapman production function. Thus,

$$n = \left(\frac{n_0}{\alpha_{rc}}\right)^{1/2} \exp\left\{\frac{1}{2}\Big[(1 - z - \sec\chi\ e^{-z})\Big]\right\} \tag{2.22}$$

where each quantity has its usual meaning. Thus, Equations (2.21) and (2.22) show that the electron density in the E region varies with height and solar zenith angle as the square root of the ion production rate, q.

At higher altitude, diffusion plays an important role in creating electron density profile than the production rate. Between about 100 and 250 km, the electron density profile results from balance between production and recombination rates through molecular diffusion. The density in this region steadily increases with altitude, despite the decrease in production rate with altitude. This is due to the rapid decrease with altitude of the recombination rate through molecular neutrals. Above 250 km altitude, transport processes becomes more rapid than chemistry. It is at that point that the density finally starts to decrease with altitude through diffusion.

2.2 The Regions of the Earth's Ionosphere

Historically, the vertical layered structure in electron density of the ionosphere has been described in terms of three main regions (also called layers): D, E and F. Each layer represents a change in the effects of the solar ionizing radiation on the changing neutral atmospheric constituents as the altitude increases. The vertical structure of these layers

Table 2.1: Characteristics of Daytime Ionospheric Layers, (*Hargreaves*, 1992)

Region	**Height (km)**	**Plasma Composition**	**Maximum Electron Density** (m^{-3})
D	60 – 90	Hydrated protons, Negative ions	10^6 – 10^{10}
E	90 – 150	O_2^+, NO^+ and N_2^+	10^{11}
F1	150 – 180	O^+, NO^+, O_2^+, N_2^+	10^{11} – 10^{12}
F2	300	O^+, N^+, H^+, He^+	Up to a few 10^{12}

varies continuously during the day, with the season of the year, with latitude and with the phase of the solar cycle. The F region is divided into two regions: $F1$ and $F2$ (depending on the time of day). Table 2.1 depicts the typical heights, electron densities and the chemical compositions of these regions. Figure 2.3 shows a typical vertical profile of the electron density for different conditions.

The formation and separation of the Earth's ionosphere into different distinct regions, the D, E, $F1$, and $F2$ layers, results from four major factors:

1. The deposition of energy by the ionizing solar radiation at various heights depending on the absorption characteristics of the atmosphere.

2. The rate of recombination (of electrons with ions and of atomic ions with molecules) depends on the atmospheric density, which changes with altitude.

3. The chemical composition of the atmosphere, which changes with altitude.

4. Atomic or molecular diffusion which dominates above 250 km.

The peak densities come from the balance that exists between production of electrons by ionization, recombination, and the transport of the charged particles.

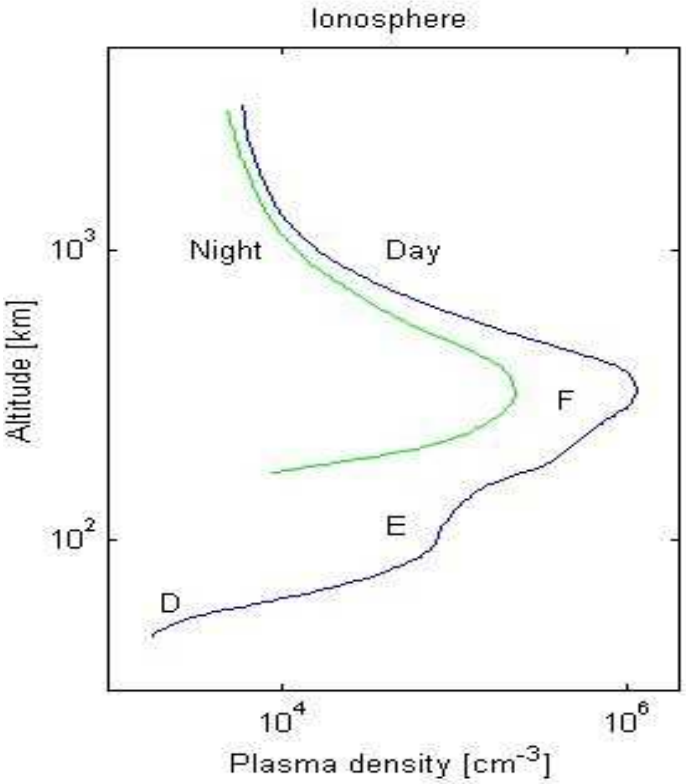

Figure 2.3: Typical profile of ionspheric plasma density with the various layers for day and night, (*Bauer*, 1973).

2.2.1 *D* Region

The *D* region is the lowest of the identifiable ionospheric regions and is located in the altitude range from 60 to 90 km. It is produced by the most penetrating of solar ionizing radiation including Lyman-α acting on NO. During the day, the electron density ranges from 10^6 to 10^{10} m^{-3} to almost zero at night. This region like the *E* region is controlled by chemical processes and molecular ions and neutrals are the dominant species. The electrons in this region can attach themselves to the neutrals to form negative ions at night while during the day, ordinary photons will dissociate the negative ions. During noctilucent cloud events, cluster ions which are prominent in the form of hydrated protons (e.g $[H_2O]_n \cdot H^+$) in the *D* region have been detected by rocket-borne mass spectrometer experiments (Figure 2.4).

The water cluster ions are dominant below ∼80 km. This makes the *D* region unlike the *E* region, to be mostly composed of both positive and negative ions and water clusters ions (*Schunk and Nagy*, 2000; *Wayne*, 1991). Diurnal variations dominate both the seasonal and

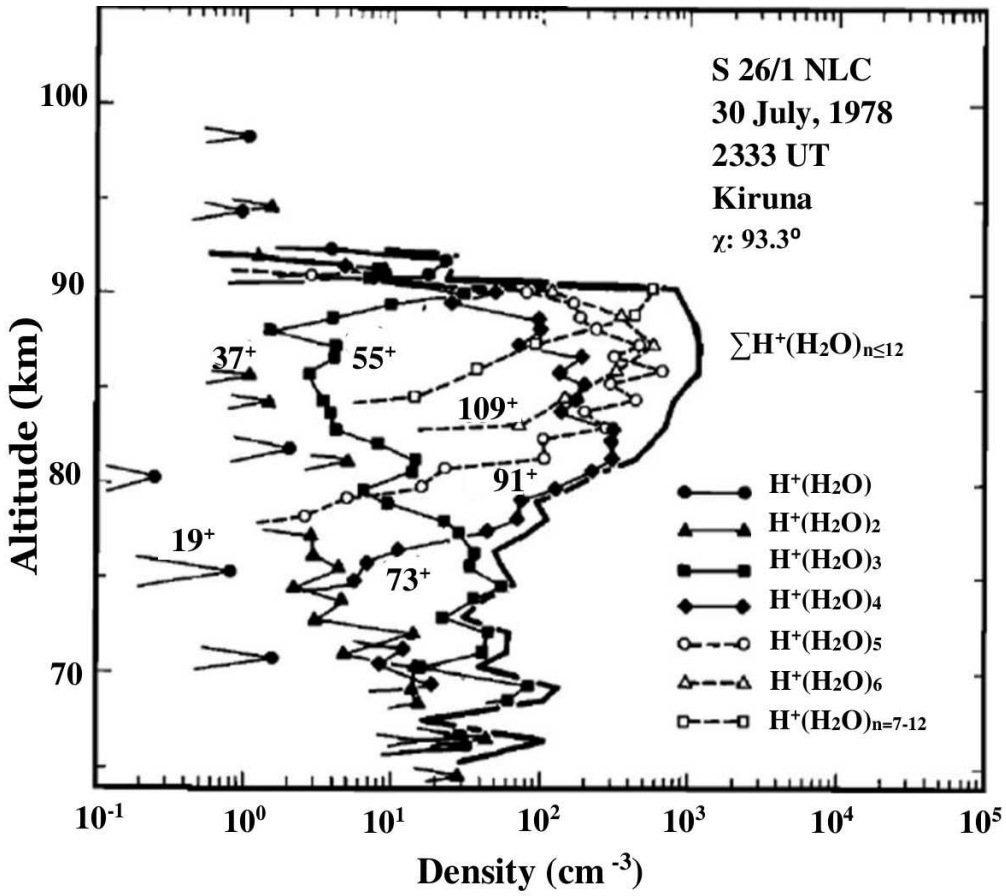

Figure 2.4: Results of rockets-borne mass spectrometric determinations of ion composition in the D region during noctilucent cloud events. The main proton hydrates are shown (*Kopp et al.*, 1985).

solar activity cycle dependence in the D region. This region affects the attenuation of radio waves propagating through this altitude range. The reason for this is due to the high rate of collision between electrons and the neutral atmosphere at these low altitudes. The radio waves force the electrons to oscillate with the wave frequency. For each collision, the radio wave loses a fraction of its energy. So, the higher the electron density is at the D region heights, the more energy is extracted from radio waves (*Hargreaves*, 1992).

2.2.2 E Region

The E region is located between 90 and 150 km altitude and the ions in this layer are mainly O_2^+, NO^+ and N_2^+ that have been produced together with O^+ ions by ultraviolet radiation in the 100-150 nm range and solar X-rays in the 1-10 nm range (*Kivelson and Russell*, 1995;

Schunk and Nagy, 2000). The electron density during the daytime is of the order of 10^{11} m^{-3} and peaks at ∼110-115 km where molecules dominate the neutrals (*Kelley*, 1989). This layer is strongest during sunlit hours, local summer and at the solar activity maximum. At sunset, the E region electron density drops by a factor of 10 or more in a short period (less than tens of minutes) before reaching a nighttime equilibrium density. The ionic recombination rate for this layer is rather rapid after sunset. As a result, this layer has densities less than 10^{10} m^{-3} by midnight. The nighttime E region ionization densities occur at higher latitudes, where particles precipitation penetrates and maintains the electron density (auroral E).

2.2.3 F Region

The F region extends upwards from an altitude of about 160 km. This region can be distinguished into two layers during the day: a small layer known as $F1$ and above it a more highly ionized dominant layer called $F2$. Very often, the difference is ignored and the entire region is referred to as the F region. The $F1$ layer, located around 150 to 200 km, is a daytime ledge at the bottom of the $F2$ layer, and the electron density peaks around 10^{11} - 10^{12} m^{-3} near 200 km. The $F1$ layer shows solar control and is most pronounced in the summer and during sunspot maximum. The $F2$ layer has the largest electron density in the ionosphere of up to 10^{12} near 300 km and like the E and $F1$ regions, this layer is solar produced. So at night both $F1$ and $F2$ merge at the level of the $F2$ layer, known as the Appleton layer. Atomic oxygen is the dominant neutral atom at F region heights. Since the number of the heavier molecules, N_2 and O_2 decreases with altitude, the loss rate for O^+ is very low above 175 km altitude. By 250 km, the loss rate becomes so small that diffusion (which speeds up with increasing altitude) takes over.

2.3 Ionospheric Electric Field and Conductivities

Sources of solar radiation and particle precipitation can play significant roles in the auroral E region. The electric field, **E** in this region is additionally, typically much larger than at other latitudes. Electric fields play a major role in the ionospheric plasma. The collisions between charged particles can be neglected for the E region. In this framework, the plasma

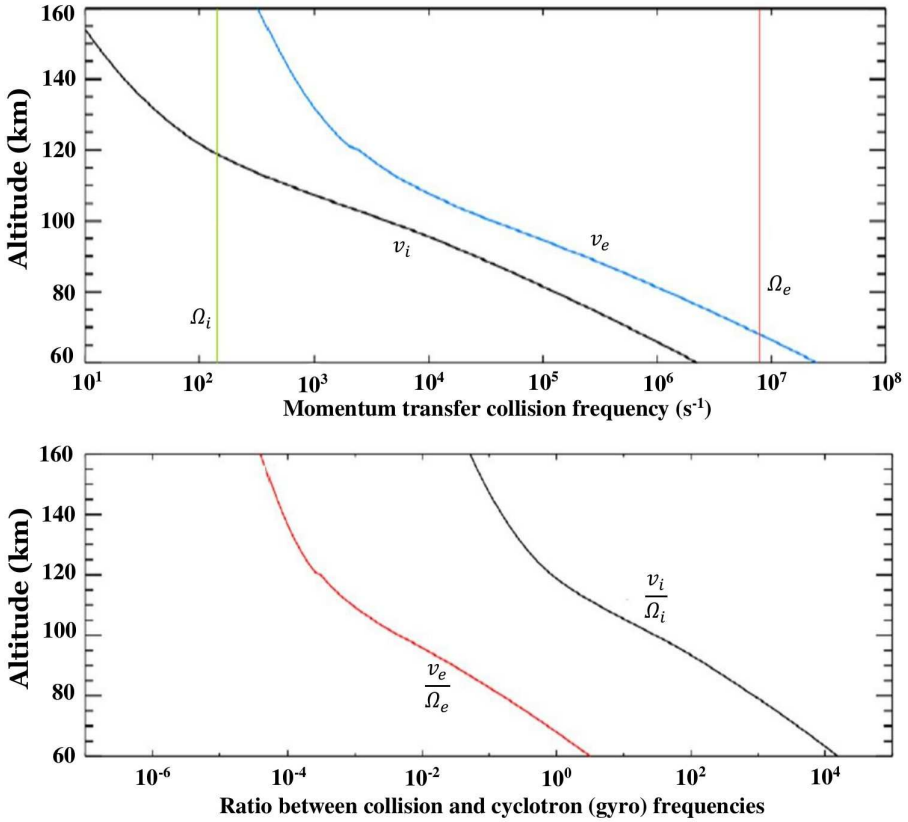

Figure 2.5: Top panel: ion-neutral (ν_i) and electron-neutral (ν_e) collision frequencies and ion and electron gyro-frequencies (or cyclotron frequencies) (Ω_i, Ω_e) as a function of altitude. Bottom panel: ratios between ion-neutral collision frequency and gyro-frequency (ν_i/Ω_i) and between electron-neutral collision frequency and gyro-frequency (ν_e/Ω_e) as a function of altitude for the March equinox, 2002. The equations used for neutral collision frequencies are from *Schunk and Nagy* (2000) and neutral density and temperature data are obtained from VITMO (Virtual Ionosphere, Thermosphere, Mesosphere Observatory), with courtesy of MSIS-90 Atmospheric Model.

is described as a two-particle fluid (electrons and ions), controlled by neutrals. In the auroral (high-latitude) E region, the Earth's magnetic field is inclined to about 10° to the vertical direction and with magnitude of 0.45 Gauss (4.5×10^{-5} Tesla). The frequency at which charged particles gyrate about the magnetic field lines is called the gyro-frequency of the particle. The collision frequency with neutrals and gyro-frequency of electrons and ions are presented in Figure 2.5 (top panel). The gyro-frequency of the electrons and ions is given by:

$$\Omega_e = \frac{eB}{m_e} \sim 10^7 s^{-1} \tag{2.23}$$

$$\Omega_i \;=\; \frac{eB}{m_i} \;\sim\; 150 s^{-1} \tag{2.24}$$

where e is the electron charge, m_e is the electron mass and the mass of ion, m_i is $\simeq 30 m_p$ (where $m_p \;=\; 1.6726 \times 10^{-27}$ kg is the proton mass). The electron-neutral, ν_e and ion-neutral, ν_i collision frequencies for the lower E region are approximately 10^4 s^{-1} and 10^3 s^{-1} respectively (Figure 2.5 (top panel)). This satisfies the relation $\nu_e/\Omega_e \ll 1$ and $\nu_i/\Omega_i > 1$ for the region between 100 and 120 km altitudes (Figure 2.5 (bottom panel)). In that region, the ions can thus be treated as unmagnetized or partially magnetized, while the electrons are magnetized.

2.3.1 Momentum Balance in the E Region Ionosphere

The plasma species (electrons and ions) are subject to many types of forces. The forces include the plasma pressure gradient, gravity, magnetic field, atmospheric winds, etc. In the plane perpendicular to $\mathbf{B}$, the balance between collisions and electro-magnetic forces are the only things that matter on scales >10 m. Therefore, the steady-state perpendicular component of momentum equation of motion for electron and ion reduces to (*Schunk and Nagy*, 2000):

$$0 \;=\; \frac{q_i}{m_i}\mathbf{E}_\perp + \mathbf{v}_{i\perp} \times \vec{\Omega}_i \;-\; \nu_i(\mathbf{v}_{i\perp} - \mathbf{v}_{n\perp}) \tag{2.25}$$

and

$$0 \;=\; -\frac{q_e}{m_e}\mathbf{E}_\perp + \mathbf{v}_{e\perp} \times \vec{\Omega}_e \;-\; \nu_e(\mathbf{v}_{e\perp} - \mathbf{v}_{n\perp}) \tag{2.26}$$

where $\vec{\Omega}_i = e\mathbf{B}/m_i$ are vectors in the magnetic field direction with magnitude given by the ion and electron cyclotron frequecies; $\mathbf{v}_{e\perp}, \mathbf{v}_{i\perp}$ are the zero-th order velocities of electron and ion. The perpendicular relative ion-neutral speed, $\mathbf{v}_{in}$, is defined as:

$$\mathbf{v}_{in} \;=\; \mathbf{v}_{i_\perp} - \mathbf{v}_{n\perp} \tag{2.27}$$

and the electric field in the frame of reference of the neutral gas as:

$$\mathbf{E}'_\perp \;=\; \mathbf{E}_\perp + \mathbf{v}_{n_\perp} \times \mathbf{B} \tag{2.28}$$

That is,

$$\mathbf{E}_\perp \;=\; \mathbf{E}'_\perp - \mathbf{v}_{n_\perp} \times \mathbf{B} \tag{2.29}$$

We can find $\mathbf{v}_i$, but first let's begin by substituting Equation (2.29) into Equation (2.26) (while using Equation (2.27) for $\mathbf{v}_{in}$), we get:

$$\begin{aligned}
\nu_i \mathbf{v}_{in} &= \frac{q_i}{m_i}(\mathbf{E}'_\perp - \mathbf{v}_{n\perp} \times \mathbf{B}) + \mathbf{v}_{i\perp} \times \vec{\Omega}_i \\
&= \frac{q_i}{m_i}\mathbf{E}'_\perp - \frac{q_i}{m_i}\mathbf{v}_{n\perp} \times \mathbf{B} + \mathbf{v}_{i\perp} \times \vec{\Omega}_i \\
&= \frac{q_i}{m_i}\mathbf{E}'_\perp - \mathbf{v}_{n\perp} \times \vec{\Omega}_i + \mathbf{v}_{i\perp} \times \vec{\Omega}_i \\
&= \frac{q_i}{m_i}\mathbf{E}'_\perp + \mathbf{v}_{in} \times \vec{\Omega}_i \\
&= \Omega_i \frac{\mathbf{E}'_\perp}{B} + \Omega_i \frac{\mathbf{v}_{in} \times \mathbf{B}}{B}
\end{aligned} \tag{2.30}$$

Therefore,

$$\frac{\nu_i}{\Omega_i}\mathbf{v}_{in} = \frac{\mathbf{E}'_\perp}{B} + \frac{\mathbf{v}_{in} \times \mathbf{B}}{B} \tag{2.31}$$

To get motion perpendicular to the magnetic field, the cross product of Equation (2.31) is taken, that is, $\mathbf{v}_{in} \times \mathbf{B}$, we obtain after a few algebrai steps:

$$\frac{\mathbf{v}_{in} \times \mathbf{B}}{B} = \frac{\Omega_i}{\nu_i}\frac{\mathbf{E}'_\perp \times \mathbf{B}}{B^2} - \frac{\Omega_i}{\nu_i}\mathbf{v}_{in} \tag{2.32}$$

Equation (2.32) can be substituted into the second term on the right hand side of Equation (2.31) to get:

$$\frac{\nu_i^2}{\Omega_i^2}\mathbf{v}_{in} = \frac{\nu_i}{\Omega_i}\frac{\mathbf{E}'_\perp}{B} + \frac{\mathbf{E}'_\perp \times \mathbf{B}}{B^2} - \mathbf{v}_{in} \tag{2.33}$$

$$\mathbf{v}_{in}\left(1 + \frac{\nu_i^2}{\Omega_i^2}\right) = \frac{\nu_i}{\Omega_i}\frac{\mathbf{E}'_\perp}{B} + \frac{\mathbf{E}'_\perp \times \mathbf{B}}{B^2} \tag{2.34}$$

Or

$$(\mathbf{v}_{i_\perp} - \mathbf{v}_{n_\perp})\left(1 + \frac{\nu_i^2}{\Omega_i^2}\right) = \frac{\nu_i}{\Omega_i}\frac{\mathbf{E}'_\perp}{B} + \frac{\mathbf{E}'_\perp \times \mathbf{B}}{B^2} \tag{2.35}$$

Therefore,

$$\mathbf{v}_{i_\perp} = \mathbf{v}_{n_\perp} + \frac{\nu_i/\Omega_i}{1 + \nu_i^2/\Omega_i^2}\frac{\mathbf{E}'_\perp}{B} + \frac{1}{1 + \nu_i^2/\Omega_i^2}\frac{\mathbf{E}'_\perp \times \mathbf{B}}{B^2} \tag{2.36}$$

A similar expression can be obtained for electrons by repeating the above steps and we get:

$$\mathbf{v}_{e_\perp} = \mathbf{v}_{n_\perp} - \frac{\nu_e/\Omega_e}{1 + \nu_e^2/\Omega_e^2}\frac{\mathbf{E}'_\perp}{B} + \frac{1}{1 + \nu_e^2/\Omega_e^2}\frac{\mathbf{E}'_\perp \times \mathbf{B}}{B^2} \tag{2.37}$$

Equations (2.36) and (2.37) clearly show the strong relationship between the electron and ion motion and the ν_e/Ω_e and ν_i/Ω_i ratios. Lower down in the ionosphere, say below 110

km, the ions are collisional and are unmagnetized and as a result ν_i/Ω_i is very small (Figure 2.5). The electrons on the other hand are magnetized all the way down to 80 km and ν_e/Ω_e is very small. Therefore, the approximate expressions for ion and electron velocities between 90 and 110 km are:

$$\mathbf{v}_{e_\perp} \approx \mathbf{v}_{n_\perp} + \frac{\mathbf{E}'_\perp \times \mathbf{B}}{B^2} = \frac{\mathbf{E}_\perp \times \mathbf{B}}{B^2} \tag{2.38}$$

$$\mathbf{v}_{i\perp} \approx \mathbf{v}_{n_\perp} + \frac{\Omega_i}{\nu_i}\frac{\mathbf{E}'_\perp}{B} \tag{2.39}$$

The electrons $\mathbf{E}_\perp \times \mathbf{B}$ drift and the ions follow the neutrals, with an additional weak Pedersen drift in the direction of $\mathbf{E}'$. While the ions drift along the electric field, the electrons drift in the opposite direction so that there is a relative drift between the electrons and ions. The difference in ion and electron velocities results in an important current (Hall current) in the $\mathbf{E} \times \mathbf{B}$ direction. The Hall current is one source of free energy that can be used for the excitation of waves in order to help dissipate the currents.

2.4 Thermal Structure of the Neutral Atmosphere And Atmospheric Dynamics

Based on the variations of temperature with height, the neutral atmosphere can be classified accordingly as: the *troposphere*, *stratosphere*, *mesosphere*, *thermosphere*. The vertical distribution of the temperature for a neutral atmosphere is given in Figure 2.6.

The atmospheric layer closest to the Earth is the troposphere. Its boundary starts from the surface of the Earth at the ground and extends to an altitude of 9 km to 17 km (its upper boundary, called the tropopause). The temperature decreases rapidly with altitude and the major atmospheric mass (about 80%) is contained in this region (*Wallace and Hobbs*, 2006). It is in the troposphere that weather phenomena occur.

Above the troposphere is the stratosphere extending from the tropopause to about 50 km. The temperature increases with altitude in this region, reaching a maximum close to 280 K. This is the second densest layer of air in the atmosphere. The total atmospheric mass in both the troposphere and stratosphere is up to 99% (*Wallace and Hobbs*, 2006). The ozone layer

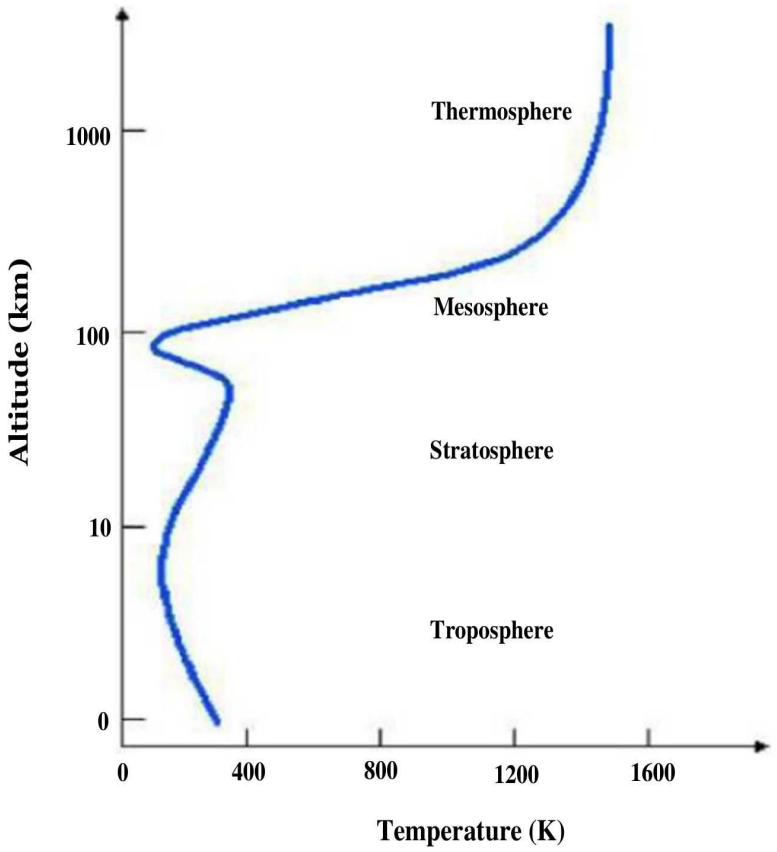

Figure 2.6: Classification of the Earth's neutral atmosphere altitude region by temperature, (adapted from *Kelley* (1989).

responsible for regulating the thermal regime is in this region and the temperature rises as the ozone concentration increases (*Kelley*, 1989). The stratopause is the boundary between the stratosphere and the next layer, the mesosphere. In the mesosphere (from 50 to about 85 km), the temperature decreases again with altitude and reaches the lowest temperature in the atmosphere in the mesopause. It is in the upper part of the mesosphere layer that most meteorites burn up while entering the Earth's atmosphere. The summer mesopause is the coldest place on Earth and its temperature may be sometimes lower than 150 K and since the temperature is frigid, water vapor freezes here thus forming ice clouds. More of this process leading to formation of ice is discussed in subsection 2.5.2. The stratosphere and mesosphere are referred to as the middle atmospheric regions.

In the summer of the polar mesopause region (say between 80 and 90 km), ice (noctilucent clouds) particles are allowed to form and grow. These noctilucent cloud ice particles are immersed in the D region plasma of the ionosphere, and the electrons attach to the ice surfaces so that they become charged. The reason for cold temperature in the summer mesosphere have been attributed to atmospheric gravity waves that propagate from below, grow unstable and produce atmospheric expansion through turbulence. Radar echoes could be detected from the ground when irregularities scatter the radar waves at a height close to the summer mesopause. These echoes are known as polar mesosphere summer echoes (PMSEs). More of this phenomenon will be discussed later.

The thermosphere (above the mesosphere) is the outermost layer of the Earth's atmosphere and extends to outer space. This layer is characterized by an increase in temperature with altitude until 250 km, due to absorption of energetic solar radiation involved in the ion chemistry. The temperature in this layer can get up to 1500°C (*Wallace and Hobbs*, 2006).

2.5 Dynamics of Atmospheric Gravity Waves

A gravity wave is an oscillation that is caused when an air parcel is displaced from its initial position and is restored to its initial position by gravity. The lifting force is buoyancy and gravity is the restoring force. In the atmosphere, gravity waves exist when the atmosphere is stably stratified, that is, the atmosphere has the ability to support and propagate wave

Figure 2.7: A sketch of atmospheric gravity waves. (From *The Upper Atmosphere in Motion*, (*Hines*, 1974)).

motion. The waves are triggered by events that cause a lifting of localized regions of the atmosphere. The dominant sources of gravity waves for the atmosphere include topography (i.e. passage of wind over a mountain range), flow triggered by convective clouds and adjustment of unbalanced flows around the polar jet stream (*Fritts and Alexander*, 2003).

Suppose there is a possibility to see these waves, and to speed up their motions, then a wide variety of wave shapes moving in many direction would be seen, as depicted by the famous cartoon by *Hines* (1974) in Figure 2.7. The cartoon is meant to illustrate that in general, most of the waves propagate diagonally upwards or downward. We see some waves propagating much like snake wiggling rapidly in frequency and magnitude and then suddenly reflected downward. Some of these waves seem to break apart into countless smaller waves which gradually fade from view. Hence some waves can last only a few minutes, while others last for hours. Some can have large amplitude while others can go nearly unnoticed (*Nappo*, 2002).

Each wave causes velocity, pressure and density fluctuations and these waves carry energy and momentum flux with them as they propagate. If such a wave loses no energy as it

propagates, then the exponential decrease of atmospheric density with increasing height results in an exponential increase of amplitude with increasing height. Thus waves that start at ground level with amplitudes of say a few centimeters per second will attain amplitudes of several tens of meters per second at altitudes of about 70 km and above. The waves do in fact lose some energy and momentum as they rise in height, the most dramatic losses occurring in the regions above 70 km altitude.

2.5.1 The Importance of Atmospheric Gravity Waves

Gravity waves have been recognized for decades to play a major role in transporting energy and momentum, and to explain the origins of turbulence and mixing (*Hines*, 1960). Studies done by *Lindzen* (1981) and *Holton* (1982) examined the gravity waves influence on general circulation and thermal structure of the middle atmosphere. The generation of gravity waves at a point source, say a mountain, can dissipates elsewhere, thus resulting in energy and momentum transfer from the first/source point to the second. This transfer of energy and momentum can in turn alter the mean flow in the dissipation region. In the mesosphere, the directions of the mean winds can be reversed relative to the expected wind directions deduced without inclusion of gravity waves. This phenomenon occurs because the waves deposit momentum and energy as they dissipate; the momentum and energy are deposited in the atmosphere and affect both the mean winds and the temperature distribution. In particular, the momentum and energy deposited by the waves alter the mean eastwards (zonal) winds, in some cases even reversing them compared to the direction expected on the basis of radiative theory alone. This changed zonal wind then drives a north-south (meridional) wind circulation, and this in turn causes upwelling at some latitudes and down-welling at others. As a result, the temperatures in the upper atmosphere are also substantially altered relative to their radiative situation (*Holton*, 1982, 1983). One important result of note is the phenomenon of the polar summer mesopause becoming much colder than the winter polar mesopause. Thus, gravity waves are major transporters of thermal energy and momentum in the atmosphere. They continue to represent a significant portion of small-scale atmospheric variability. For all these reasons, and more, they are important phenomena that merit further study. More details about the way in which these waves modify the mean circulation

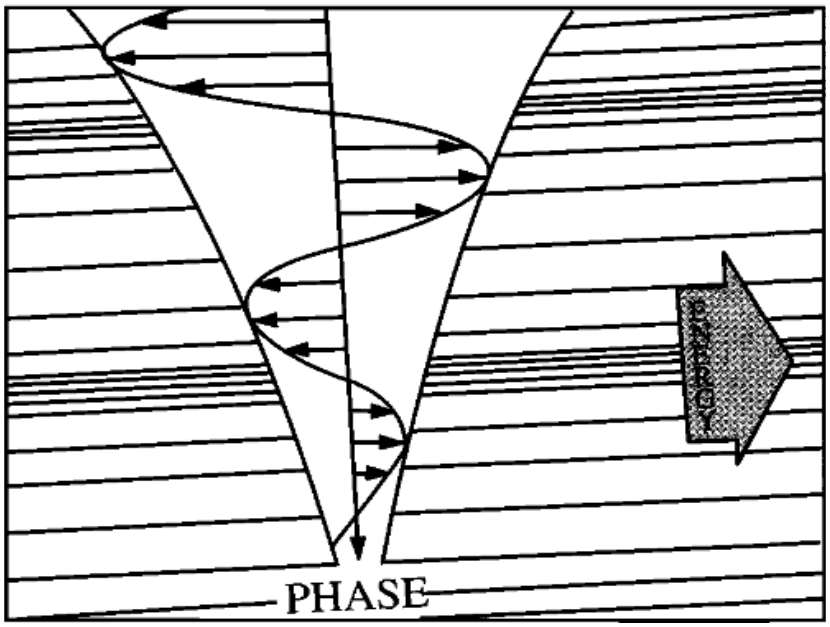

Figure 2.8: Schematic representation showing the growth of gravity wave propagating nearly vertically. The arrows indicate the neutral velocity variation with height, whereas the nearly horizontal lines show the density variation. Also shown are the directions of the group velocity (i.e energy) and the phase velocity of the gravity wave (from *Hines*, 1960).

and the latitudinal temperature distribution are considered next.

2.5.2 Gravity Wave Growth With Height and How They Affect the General Circulation of the Middle Atmosphere

Gravity waves grow exponentially with height. That means that a small gravity wave generated in the troposphere can grow one hundred times in amplitude as it propagates to the mesosphere. Gravity wave's amplitude grows as the inverse square of the density (*Brasseur and Solomon*, 2006). We can understand this by taking into account that for the kinetic energy (*Brasseur and Solomon*, 2006):

$$KE \;=\; \frac{1}{2}\rho\,|v(z)|^2 \tag{2.40}$$

to remain constant, the amplitude of the wave must grow as:

$$|v(z)| \;=\; C\,[\rho(z)]^{-\frac{1}{2}} \tag{2.41}$$

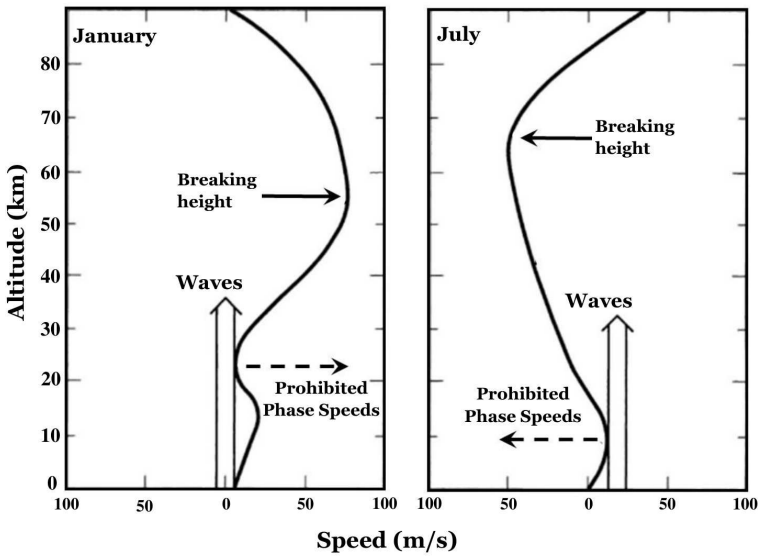

Figure 2.9: Altitude profiles of mean zonal winds at a typical mid-latitude (45○) location in winter (left panel) and summer (right panel) with respective hemispheres with wave breaking heights indicated. Wind directed to the right of zero are eastward and to the left of zero westward, (adapted from *Lindzen* (1981)).

where ρ is the density and v is the wave's velocity and C is a constant. Since the atmospheric density decreases exponentially with height as $\rho_0\, e^{-z/H}$ (where z is altitude and H is the atmospheric scale height), we will have that:

$$|v(z)| \;=\; \frac{C}{\rho_0}\,\exp\left(\frac{z}{2H}\right) \tag{2.42}$$

where ρ_0 is the reference density at the surface ($z = 0$). Equation (2.42) implies that, in order to conserve energy, the amplitude of the wave will grow exponentially with increasing altitude as the wave propagates upward. So a gravity wave generated at say 10 km altitude can grow up to 100 times in amplitude by the time it reaches the mesosphere. An illustration showing the growth of gravity wave with height is given in Figure 2.8. The wavefronts of such waves are almost horizontal as shown and as a result of this, the group velocity has a slightly upward tilt, while the phase velocity has a sharply downward tilt (*Schunk and Nagy*, 2000).

Figure 2.8 leaves one with the impression that the wave continues to grow with altitude, but like an ocean wave which eventually breaks on the beach, gravity waves break in the middle and upper atmosphere. Gravity waves propagation through the atmosphere depends on thermal structure and wind distribution, which considerably changes with season (*Brasseur*

and Solomon, 2006; *Lindzen*, 1981).

To understand gravity waves effects, we can picture the middle atmosphere at solstice for instance. The ozone heating provides high temperature right around 15-20 km altitude over the northern hemisphere summer. As a result, the ozone heating at higher latitudes and in the polar region of summer is lower than in the equatorial regions. The reason is simply because the tropopause is relatively higher in the equatorial regions, due to large starting temperatures near the ground, followed by convection driving the more humid air higher up in the equatorial regions. This means that over an altitude range of 20–40 km, the pressure is higher over the summer pole than over the equator. The ozone heating from the stratosphere occurs in the summer hemisphere, but only to lower latitudes in winter ($< 65°$). The equatorial pressure gradient through the Coriolis force produces a westward geostrophic wind. By contrast, the winter hemisphere at 20 km is relatively colder and the stratopsheric jet is in the same direction as the tropospheric jet.

As illustrated in Figure 2.9, large geostrophic winds are produced above 50 km in response to the seasonal pressure gradients. In addition, as just explained above, due to the pressure difference that is set up by a contrast between winter and summer hemispheres, the stratospheric zonal flow during summer is from east to west (easterly) in a large anti-cyclonic weather system but in winter, it blows from west to east (westerly) within the polar vortex. The upward propagating gravity waves whose horizontal components of the phase velocity match those of the zonal wind speed (i.e. $\omega/k = \bar{u}$, where ω is the angular frequency, k is the wavenumber and $\bar{u}$ is the mean zonal wind speed) are absorbed (eventually at "critical levels") (*Brasseur and Solomon*, 2006) and become a source of east (westerly) momentum in summer at those critical levels. Waves that are not taken away by the mean flow continue to move upward and gain amplitude proportionally to $\exp(z/2H)$. At some point, their amplitude saturates. The waves might even crash (breaking point or height as illustrated in Figure 2.9). Ultimately, energy and zonal momentum have to be fed to the mesosphere.

A remarkable consequence of the circulation pattern (meridional flow) introduced by gravity waves is that the ascending air is expanding adiabatically at the summer mesopause and therefore cooling as it moves to replace the air that is being pulled towards the other hemisphere. The resulting temperature can be as low as 150 K in the summer hemisphere

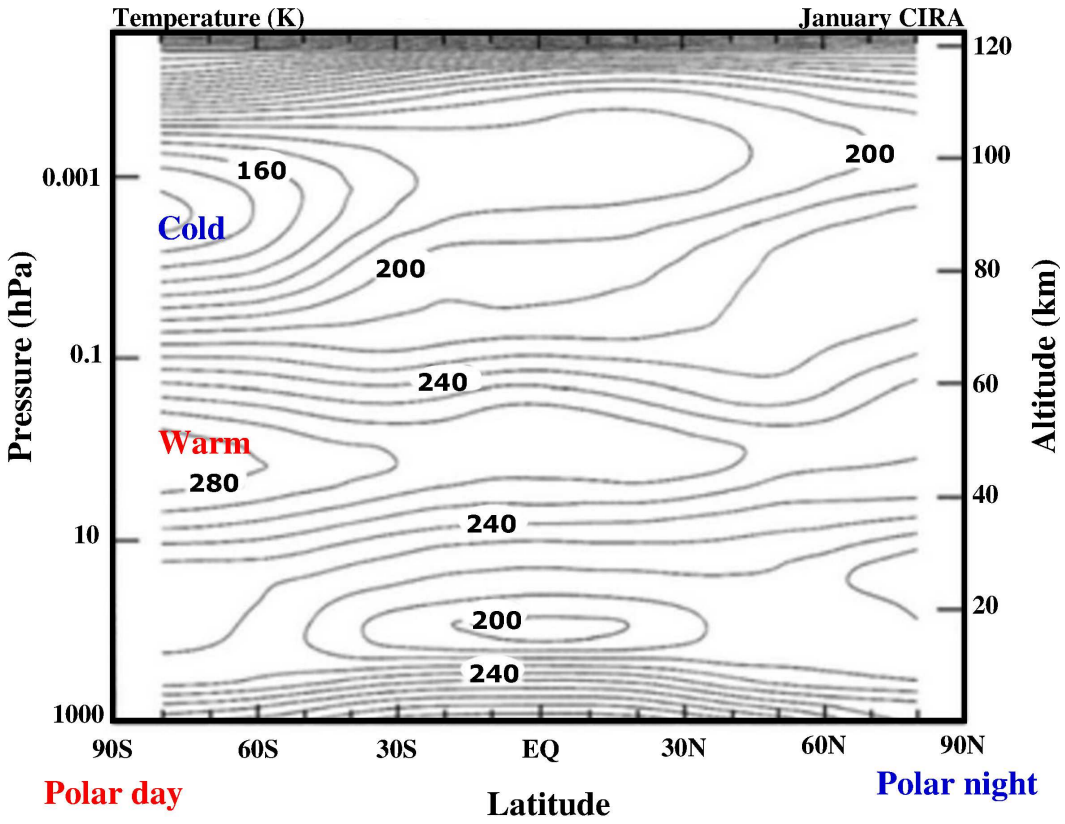

Figure 2.10: Latitude versus pressure/height and zonal average temperature from the surface to approximately 120 km altitude in January. Note the temperature mininum (< 200 K) at the tropical tropopause, the temperature maximum (280 K) at the summer stratopause and the temperature minimum (< 140 K) at the summer mesopause. The height of mesopause increases from approximately 90 km in summer to 100 km in winter, (adapted from *Brasseur and Solomon* (2006) based on *Fleming et al.* (1988)).

(conversely, over the winter hemisphere, the air gets heated around 80 km because of the compression). This dynamics explains why the polar mesopause is much colder in the summer than in winter. Figure 2.10 shows the cross section of the zonal mean temperature in January. The air in the summer hemisphere can get cold enough to condense whatever little water is present near 80 to 90 km. As the temperatures decrease to extremely low values during summer in the mesosphere, ice particles form. These ice particles sediment and grow until they become visible to the naked eye as notilucent clouds.

Chapter 3
INSTRUMENTS

This chapter briefly describes the basic principles behind coherent radar operations. The SuperDARN radar operation is discussed in detail and the mode of wave propagation is described.

3.1 Coherent Radar Methods

A coherent radar transmits radio waves to the atmosphere and higher up in the ionosphere and the information obtained in the returned echo is carefully analyzed. The physical principle behind the coherent radar operation is based on momentum conservation applied to the incident wave vector, $\mathbf{k}_{inc}$, the scattered wave vector, $\mathbf{k}_s$, and the ionospheric irregularities wave vector, $\mathbf{k}_{irr}$ (*Fejer and Kelley*, 1980; *Haldoupis*, 1989; *Schlegel*, 1996). From Figure 3.1, we find:

$$\mathbf{k}_s \;=\; \mathbf{k}_{inc} \;+\; \mathbf{k}_{irr}, \tag{3.1}$$

Equation (3.1) follows the Bragg condition for wavelengths of radar waves and irregularities under consideration. This means that:

$$\lambda_{radar} = 2\lambda_{irr}\sin(\theta_s/2) \tag{3.2}$$

If $|\mathbf{k}_{inc}| = |\mathbf{k}_s| = 2\pi/\lambda_{radar}$, we have $|\mathbf{k}_{irr}| = 2\pi/\lambda_{irr}$. The scattering angle is given as θ_s. When multiple scatterers with scale size of λ_{irr} are regrouped (Figure 3.1), the Bragg condition implies a constructive interference which can result in a maximal backscatter amplitude (*Booker*, 1956). It follows also from Figure 3.1 that the scale size of the scatterers that can be detected by the radar is determined by the radar's wavelength, λ_{radar}. Thus,

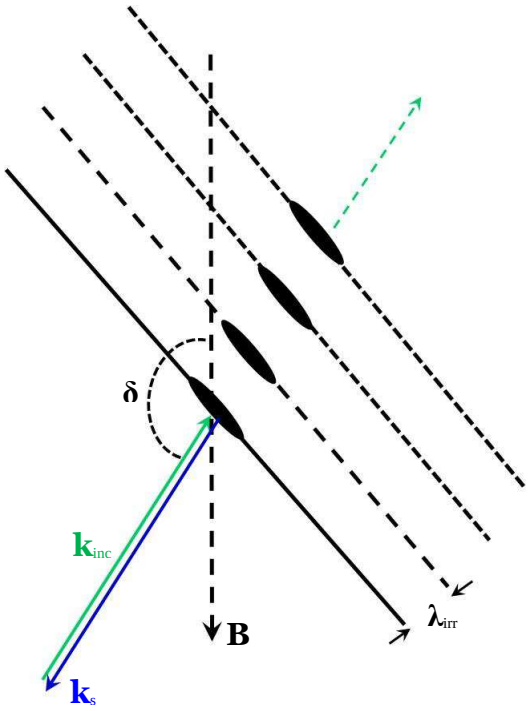

Figure 3.1: A sketch showing the radar backscatter from field-aligned irregularities. $\mathbf{k}_{inc}$ stand for the incident radar wavevector and $\mathbf{k}_s$ for the scattered wavevector. $\delta = 90 + \alpha_a$, where α_a gives the aspect angle. The scale size of the irregularities is denoted by λ_{irr}.

for a monostatic backscatter (with $\theta_s = 180°$), which is commonly applied by ionospheric experiments, the condition in Equation (3.2) produces:

$$\lambda_{irr} = \frac{\lambda_{radar}}{2} \tag{3.3}$$

Equation (3.3) implies that the wavelength of the irregularity should be half the radar's wavelength. The rate of change with time in the phase of the scattering irregularity can be used to obtain the Doppler shift of the received signal. Typically, the parameters investigated are power, Doppler velocity and spectral with of the returned echoes. This thesis focuses on measurements obtained from ten SuperDARN radars.

3.2 Super Dual Auroral Radar Network and Operations

The Super Dual Auroral Radar Network (SuperDARN) system is an array of ground-based, coherent, HF, Doppler radars that is used to monitor ionospheric echoes from the mid- to high-latitude ionosphere and information about global ionospheric convection maps are provided from the Northern and Southern hemispheres (*Chisham et al.*, 2001; *Greenwald et al.*, 1995). The SuperDARN radars can provide impressive statistics of the ionospheric echoes and we know for a fact that close-range echoes (with properties different from the rest) are present (e.g. *Hall et al.*, 1997).

SuperDARN has been very useful in providing models that can creat and operate a large scientific instrument infrastructure, and within the past two decades, over 33 radars have been built, thus making SuperDARN a unique international operation. SuperDARN is capable of operating in the 8-20 MHz range. It transmits radio pulses and receives echoes from the ionosphere. The echoes occur because the radar waves have been backscattered by the ionospheric irregularities or waves generated in the ionosphere. In order for scattering from a field-aligned irregularity to occur, the radar waves must propagate perpendicularly to the magnetic field. The reason why SuperDARN radars produce oblique beams while operating in HF band of 8-20 MHz is that the radio rays can be refracted in the ionosphere and become perpendicular to the magnetic field lines at some point along their trajectory. In the high-latitude ionosphere, the perpendicularity condition can only be achieved if the ray path is refracted toward the horizontal as the wave enters the ionosphere, (Figure 3.5). Radar backscatter can occur, if the radar wavelength is twice that of the scattering ionospheric irregularity (Equation (3.3)), implying that the SuperDARN radars monitor irregularities with scale sizes of about 10 m. The amount of refraction depends upon the electron density of the plasma and this varies diurnally, annually and with geomagnetic activity. Therefore the SuperDARN radars must be capable of operating over extended HF frequency bands (*Greenwald et al.*, 1985).

The SuperDARN radars typically operate in pairs with common viewing areas providing

drift information that are contained in the returned signals. As of the time when the study of this thesis was carried out, SuperDARN comprised 22 radars in the Northern Hemisphere and 11 radars in the Southern Hemisphere. The fields-of-view (FOV) of these SuperDARN radars are presented in Figure 3.2.

A typical SuperDARN radar setup is presented in Figure 3.3. The field-of-view of each radar consists of 16 sequentially scanned beam positions separated in azimuth by $\sim$3.24° providing a full field of view of 52°. This is schematically illustrated in Figure 3.4. In the standard operating mode, a total of 75 range gates are sampled for each beam. Detected echoes are gated into 300 μs. Assuming that the HF wave travels at the vacuum speed of light c (3×10^8 m s^{-1}), this corresponds to a 45 km gate length. The lag to the first gate is 1200 μs, which corresponds to the 180 km for the nearest range from the radar site, and the last gate is usually at 3555 km, giving a total of 3375 km range span. Each SuperDARN radar consist of a main array (16 antennas) and an interferometer array (4 antennas). The latter is used for angle of arrival measurements (*André et al.*, 1998). The standard dwell time for each beam is 3 or 7 seconds depending on the scan mode, which enables a full 16-beam sweep every 1 or 2 minutes, respectively. This short dwell time is one of the primary benefits of these coherent radars. As already stated above, the radar receives ionospheric signals from the scattering of radar signals from ionospheric irregularities that are usually aligned with the geomagnetic field lines. Ionospheric parameters such as the Doppler shift, power and spectral width are determined from the autocorrelation function.

3.3 Determination of Ionospheric Parameters

SuperDARN transmits radio wave pulses in order to determine spectral properties such as the Doppler shift, spectral width and backscattered power of the ionospheric plasma. SuperDARN uses an irregularly spaced multipulse sequence in order to localize targets and ensure a sufficiently long decay time for the autocorrelation function (ACF). When each pulse is sounded, the information received is converted into a complex ACF, a digitalized signal that is of the form $Ae^{i(\omega t-\phi)}$. Each pulse in the sequence is 300 μs in duration and at intervals of t =0, 14, 22, 24, 27, 31, 42, 43 μs, with a standard pulse separation (lag)

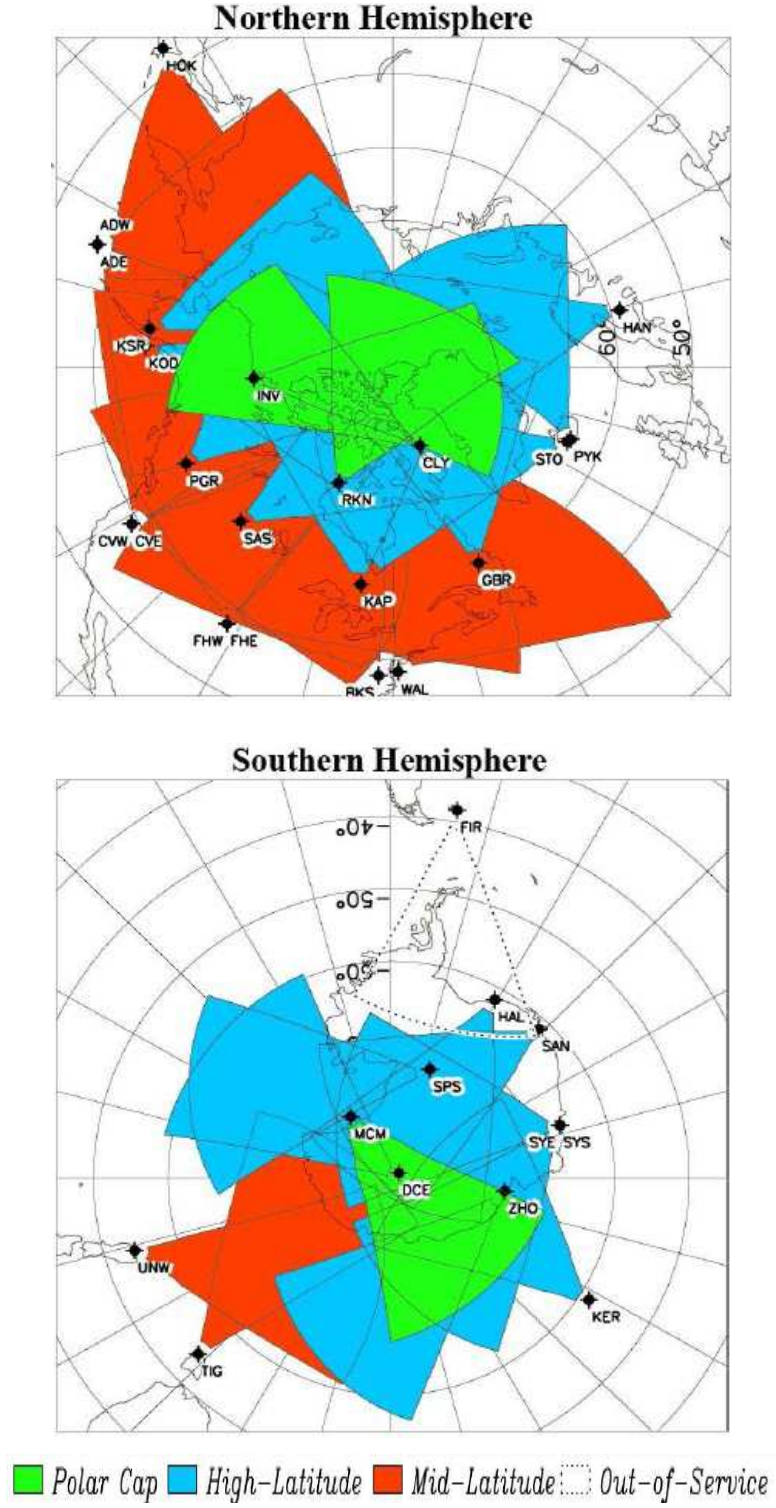

Figure 3.2: Fields-of-view in geomagnetic coordinates for the Northern and Southern Hemisphere SupeDARN radars.
(*http://vt.superdarn.org/tiki-index.php?page=radarFoV*).

Figure 3.3: The Saskatoon radar showing the main and interferometer arrays.

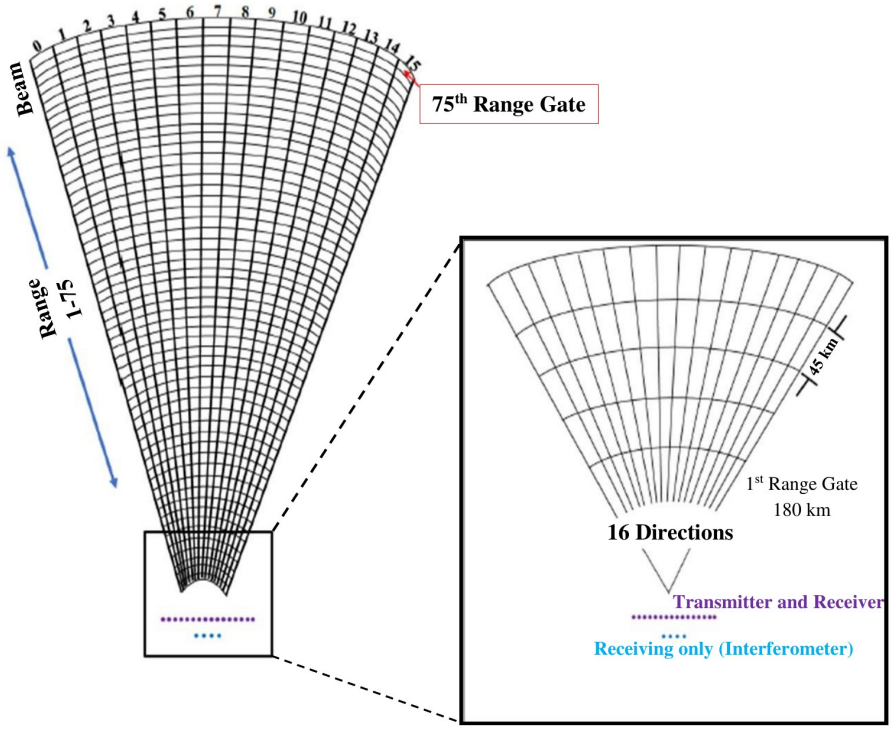

Figure 3.4: Schematic illustration of beams from 0 to 15 for the 75 range gates (left) and expanded view to show range gate resolution of 45 km with the first range gate at 180 km from the radar (right).

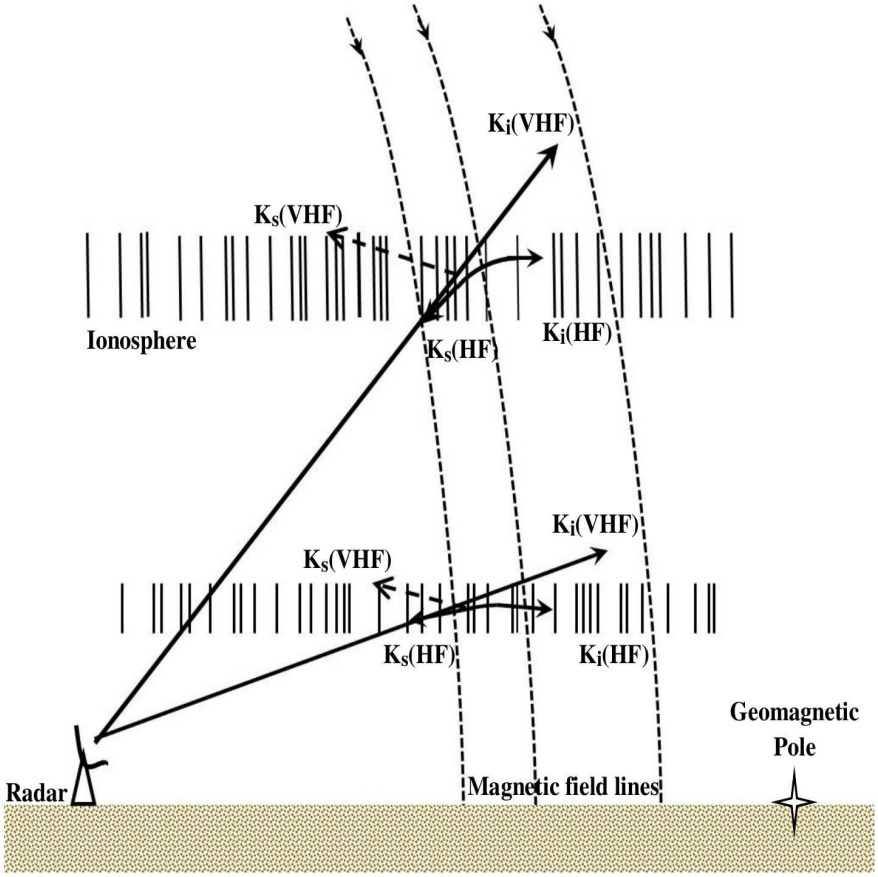

Figure 3.5: Illustration of the manner in which VHF and HF radar signals are scattered into space by high-latitude E and F region ionospheric irregularities. (Adapted from *Greenwald et al.*, 1985)

giving by some multiples of $\tau = 1.8$ ms. Figure 3.6 illustrates this pulse sequence and lag determination.

The autocorrelation function approach is based on the correlation of signals transmitted at different times but received from the same range. It is generated from the sampled and processed pulses returned from the ionosphere, for various time delays between them and for all ranges between 180 and ∼3600 km (gate 75). The time delay between pulse sequences allows the antenna to receive echoes from the first pulse for all range gates before transmitting the next pulse. Before describing the procedure involved in deriving the velocity, power and spectral width of the returned signal, it is important to note that the generation of ACFs is unfortunately not always easy to accomplish. Consider for example, the ACF generation for a simple case of two-pulse transmission. Figure 3.7 illustrates some features for time t_0

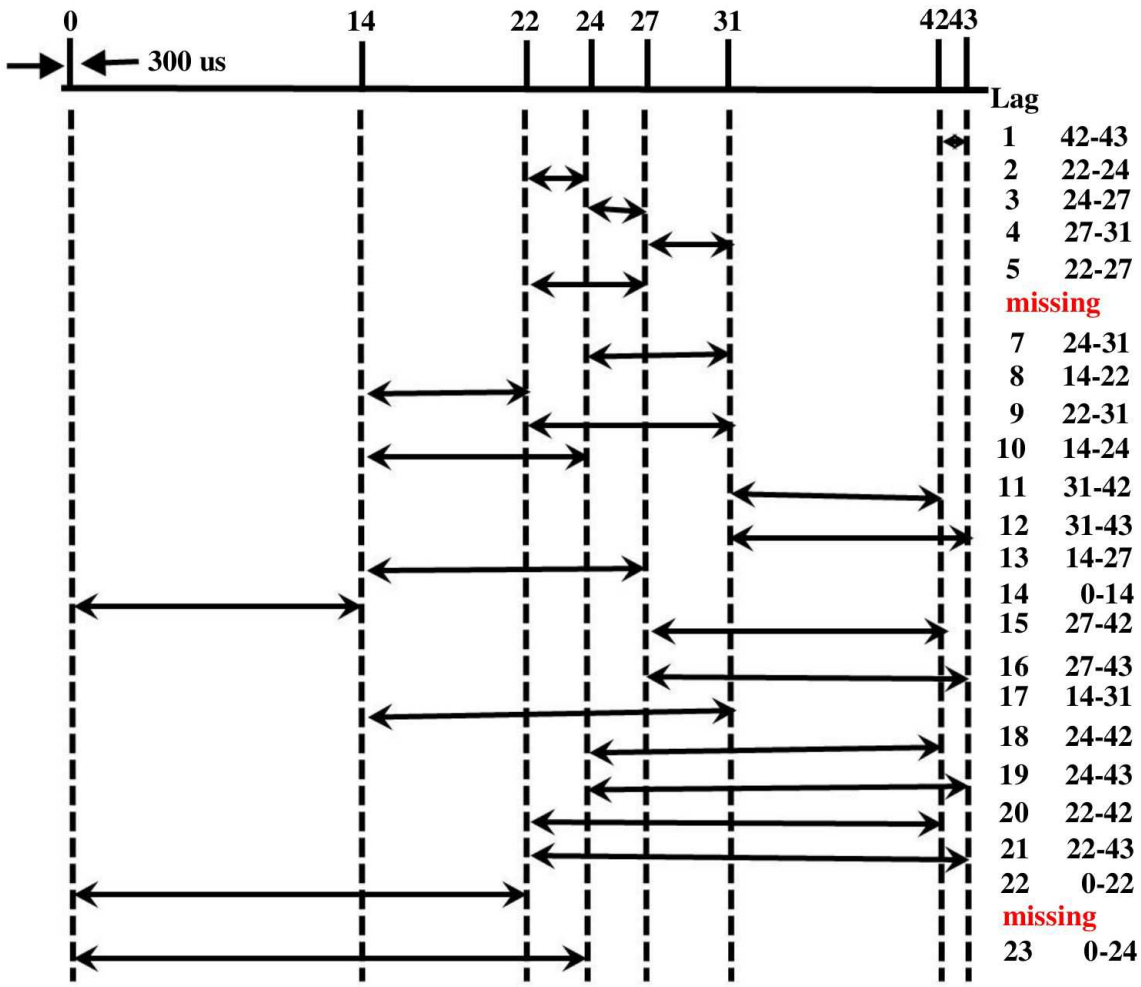

Figure 3.6: 8-pulse sequence currently used by SuperDARN. Transmission time between pulses (shown by vertical lines) is represented in μ seconds, progressing from left of the page to right, and lag time increases from top of plot to bottom. The pulse duration is 300 μs.

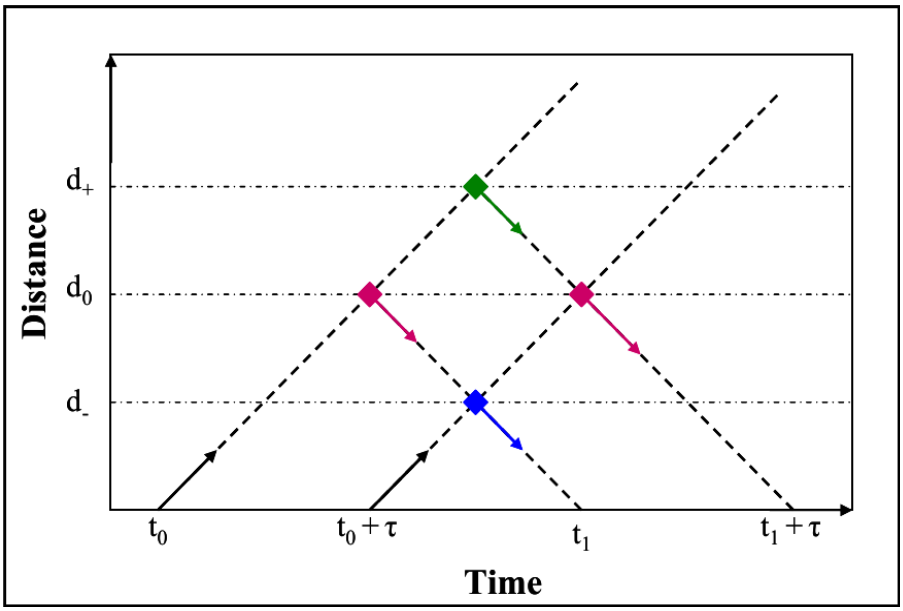

Figure 3.7: Schematic illustration of a of 2-pulse sequence.

for first pulse and time $t_0 + \tau$ for second pulse transmission with the scattering assumed to occur at three different ranges: d_0, d_- and d_+.

Echo 1 arrives at $t_1 = t_0 + 2d_0/c$, and that is also the time when echo 2 returns from d_-, so that the total amplitude is (*Baker*, 1988):

$$A(t_1) \;=\; A_1(d_0) \;+\; A_2(d_-). \tag{3.4}$$

At time $t_1 + \tau$, the echo 2 returns from range d_0 with an amplitude of $A_2(d_0)$, and also echo 1 returns with amplitude $A_1(d_+)$, so that at this time, the total amplitude is:

$$A(t_1 + \tau) \;=\; A_1(d_+) \;+\; A_2(d_0). \tag{3.5}$$

Averaging these amplitudes over a number of pulse sequences gives the ACF as:

$$< A(t_1)A(t_1+\tau) > = < A_1(d_0)A_2(d_0) > \;+\; < A_1(d_0)A_1(d_+) > \;+\; < A_2(d_0)A_2(d_-) > \\ + < A_1(d_+)A_2(d_-) > \tag{3.6}$$

After averaging over a sufficiently large number of "events", the last three terms become uncorrelated time-average signals and are removed from the procedure, so that Equation

(3.6) simply reduces to:

$$< A(t_1)A(t_1+\tau) > = < A_1(d_0)A_2(d_0) > . \tag{3.7}$$

Equation (3.7) contains information about the lag τ and d_0. The above consideration thus shows that measurements at a certain range could be affected by signals from other ranges if the time-average of the last three terms of Equation (3.6) is not exactly equal to zero, or if there are not enough "events" to remove cross-range noise. Cross-range noise is an example of 'bad lags' (strong scatter influence from 'unwanted' ranges) and is excluded in ACF computation. The other bad lags happen when the SuperDARN radar receives and transmits signals at the same time. The radar must not be transmitting when it receives first echoes from pulse 1 (Lag 0). Also, ACFs are generally bad when there is no data at lag 0. The position of the gaps depends on the lag to the first range, pulse length and the lag separation.

In order to ensure a sufficiently long decay time for the ACF, SuperDARN uses an irregularly spaced multi-pulse sequence. Once the ACF is obtained, a program known as 'fitacf' is used to determine spectral parameters such as the line-of-sight (LOS) velocity, (i.e. the component of the plasma drift along a radar beam), backscattered power and spectral width.

The real and imaginary components of a good ACF is shown in Figure 3.8a, having a shape of a decaying sinusoid, with the real and imaginary components plotted against lag. The LOS velocity is determined from the slope (rate of change) of the phase angle (ϕ) of the ACF. The phase angle is assumed to be: $\phi =< \omega_d > k\tau$ (where the lag number is k). The phase have a linear relationship with lag, the slope of which is the mean Doppler frequency of the echo (Figure 3.8c). The relationship between the Doppler frequency and the Doppler velocity (velocity of irregularity) is:

$$V_{irr} = \frac{c\omega_D}{4\pi f_T}. \tag{3.8}$$

where c is the speed of light. To derive Equation (3.8), it is important to take into account two shifts in the frequency of radio waves due to Doppler Effect. If f_T is assumed to be the frequency that is transmitted by the radar wave, the radio wave frequency received by the

radar as $f_R \approx f_T(1 + 2V_{irr}/c)$ and V_{irr} the velocity of irregularity, then the frequency, f_I captured by a moving irregularity would be:

$$f_I = f_T(1 + V_{irr}/c), \tag{3.9}$$

due to Doppler Effect. When the signal is returning, there is another Doppler shift (since the irregularity is moving with respect to the radar) which leads to radar-measured frequency of:

$$f_R = f_I(1 - V_{irr}/c). \tag{3.10}$$

Substituting for f_I in Equation (3.10) by using Equation (3.9), we obtain the leading order result:

$$f_R \;=\; f_T\left(1 + 2\frac{V_{irr}}{c}\right) \tag{3.11}$$

$$f_D \;=\; f_R - f_T \;=\; 2f_T\left(\frac{V_{irr}}{c}\right) \tag{3.12}$$

where f_D is related to the Doppler frequency as: $\omega = 2\pi f_D$. Substituting this into Equation (3.12) and solving for V_{irr}, we have:

$$V_{irr} \;=\; \frac{c}{2}\left(\frac{f_D}{f_T}\right) \tag{3.13}$$

We can substitute for f_D in Equation (3.13), to obtain Equation (3.8) for the Doppler velocity. The directions of the scatterer motion (i.e. away (negative velocities) and toward (positive) the radar) are accounted for in Equation (3.8).

It should be noted however that the change in the phase with time is not always as simple as the above explanation. An additional complication is if the plasma density changes while a ray is passing through the ionosphere. Also, the index of refraction may introduce a modification to the Doppler shift. In those cases, the more general description of the Doppler frequency shift should be used (*Scoular*, 2013):

$$\Delta\omega \;=\; -2k_0\left[\int_A^B \frac{\partial n}{\partial t}ds + \frac{\partial B}{\partial t}n(B) - \frac{\partial A}{\partial t}n(A)\right] \tag{3.14}$$

where A and B are the positions of the transmitter and of the target respectively, and backscatter was assumed. The refractive index is n and k_0 is wave number in free space. Since the position of the radar is fixed, the third term on the right hand side of Equation

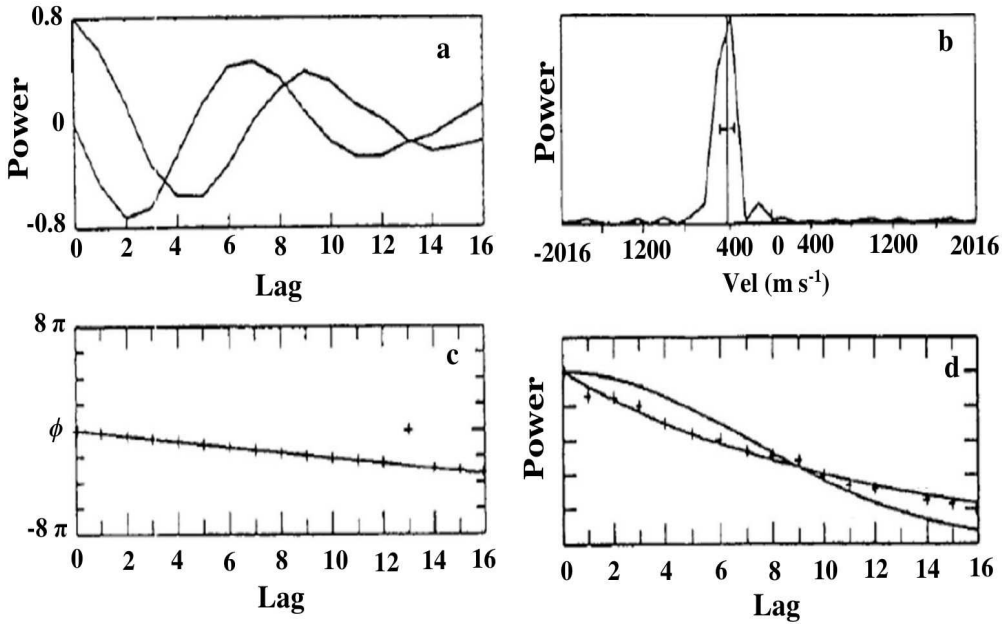

Figure 3.8: An example of radar signal processing techniques. (a) Real and imaginary parts of the ACF. (b) Doppler spectrum obtained through FFT of the ACF. (c) Phase angle as a function of lags and its linear squares fit. (d) Power variation of the ACF as a function of lag with exponential (λ) and Gaussian (σ) least square fits. (From *Villain et al.* (1987)).

(3.14), $\partial A/\partial t = 0$. Also, the contribution from the first term is usually small compared to that from the local drift but with due exceptions in the aurora (*Scoular*, 2013). The Doppler frequency shift, f_D, then gives the line-of-sight velocity, v_D (that is, the middle term on the right hand side of Equation (3.14)), and is given by (*Ponomarenko et al.*, 2009):

$$v_D \;=\; -\frac{\Delta f_D \lambda_{radar}}{2} n \tag{3.15}$$

where $\Delta f_D = \Delta\omega/2\pi$ and λ_{radar} is the radar's wavelength (the reader is referred to *Ponomarenko et al.* (2009) for detail on the above description and assumption).

The backscattered power and the spectral width are extracted from the time variation of the ACF. Power as a function of lag can be determined from the decay of the ACF (Figure 3.8b). For a determination of spectral width, the signal decay is assumed to follow either a Gaussian (σ) or exponential (λ) distribution. An example of the ACF power fitted with both exponential and Gaussian approximations can be seen in Figure 3.8d. In terms of $P(\tau)$, the spectrum associated with the exponential distribution is given by:

$$P(\tau) = P_\lambda e^{-\lambda\tau} \tag{3.16}$$

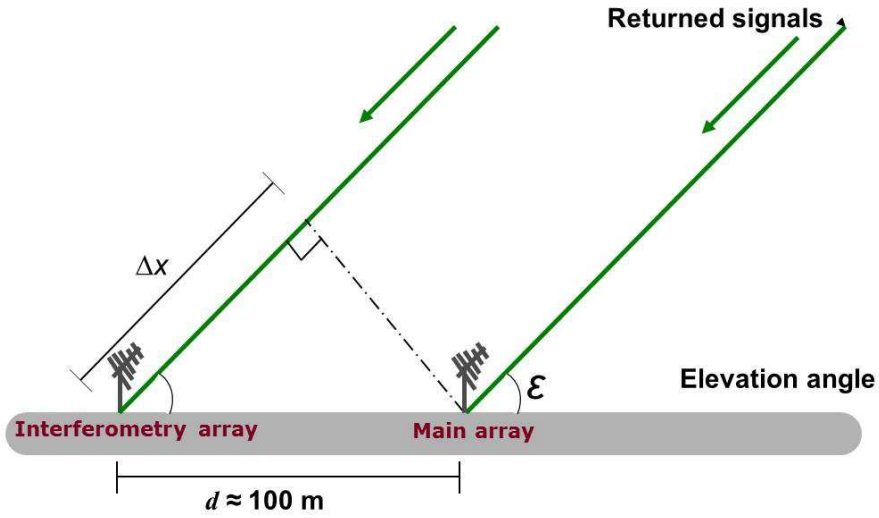

Figure 3.9: The geometry showing the interferometry technique used to measure the angle of elevation.

where P_λ is the maximum power. The constant λ (which is not to be confused as wavelength) is determined using a least square fit and thus used to calculate the Doppler spectral width:

$$width = \frac{c\lambda}{2\pi f_{radar}} \tag{3.17}$$

3.4 HF Radio Wave Propagation and Modes

3.4.1 Measurement of Elevation Angle Using the Interferometry Technique

The angle of arrival of the returned signal when measured with respect to the ground is known as the elevation angle. It is important to determine the elevation angle, as it provides information of the ionospheric region from which the backscattered signal is coming. An interferometry technique has been employed by the SuperDARN radars for determining the elevation angle (*Milan et al.*, 1997a). The additional interferometry array is located at the back of the main array and parallel to it. While the main array comprises 16 antennas that are capable of transmitting and receiving radio signal, the interferometry array consists of 4 receiving antennas only (*André et al.*, 1998).

Figure 3.9 schematically describes the method involves in the measurement of elevation

angle. The backscattered signal received at an elevation angle ε by the main and interferometer arrays have a path length difference of $\Delta x = d \cos \varepsilon$, where $d \approx$100 m (i.e. the distance between the interferometer and main arrays). The phase shift due to the path length difference, Δx, is given as $\Delta\phi = (2\pi/\lambda)\,\Delta x$. The phase can be obtained by measuring the time difference between the backscattered signals received by the main and interferometry arrays. Thus, the elevation angle can then be written as:

$$\varepsilon = \cos^{-1}\left(\frac{\lambda}{2\pi d}\Delta\phi\right) \tag{3.18}$$

3.4.2 Propagation Modes

The propagation of HF radio waves is supported by the E and F region whereas in the D region, ionospheric absorption tends to be strongest. The ionosphere is a changing medium and its characteristics vary with solar zenith angle, magnetospheric conditions, solar cycle, season and even time of year. Therefore, HF propagation conditions are highly variable and some adjustment of the frequency may be required. Hence, the SuperDARN radars are frequency agile over the HF band. In the simplest sense, the ionosphere can be considered to be comprised of several thin layers that has different refractive index (Figure 3.10). The index of refraction for radio waves in the HF band is less than 1 and given by (*Hargreaves*, 1979):

$$n_r^2 = 1 - \left(\frac{\omega_p}{\omega_f}\right)^2 \tag{3.19}$$

where ω_p, the plasma frequency is equal to $\sqrt{n_e e^2/\varepsilon_o m_e}$, ω_f is the angular frequency, e is the electron charge, n_e is the number density, ε_o is permittivity of free space and m_e is the electron mass. The plasma frequency increases with height as does the electron density, so Equation (3.19) tells us that the refractive index, n_r, becomes smaller with height and thus the path of ray gradually bends towards the horizontal until reflection occurs. To yield the required condition for reflection, we can apply the Snell's law (Equation (3.20)) to the boundary of layers shown in Figure 3.10:

$$n_r = \sin i_o \tag{3.20}$$

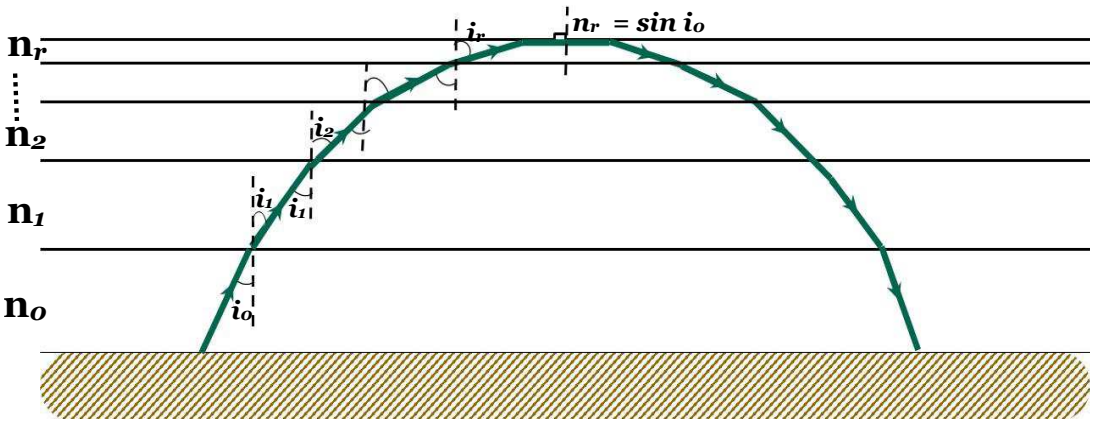

Figure 3.10: Schematic illustration to show HF radio waves bending in the ionosphere.

The angle of incidence of the wave as it enters the ionosphere is i_o. Let us substitute Equation (3.20) into Equation (3.19), and we obtain:

$$\sin^2 i_o = 1 - \left(\frac{\omega_p}{\omega_f}\right)^2 \tag{3.21}$$

$$\cos^2 i_o = \left(\frac{\omega_p}{\omega_f}\right)^2 \tag{3.22}$$

$$\omega_p = \omega_f \cos i_o \tag{3.23}$$

Therefore, for $i_o = 0$ (vertical incidence), the plasma frequency ω_p, of the medium becomes equal to the frequency of the radio wave at the reflection level. In other words, when $n = 0$, reflection of radio wave occurs. For $\omega_f < \omega_p$, the index of refraction takes an imaginary component and the wave is absorbed and (if thick layer) vanishes.

At close ranges of the radar's FOV, SuperDARN relies on ionospheric waves and structures generated not only by plasma instability but on scattering from sources like meteors and neutral turbulence. This thesis aims to find the causes of non-field-aligned-irregularity scattering observed at short ranges.

Chapter 4

BRIEF SURVEY OF THE THEORY OF *E* REGION IONOSPHERIC IRREGULARITIES

Ionospheric irregularities are density variations that have been enhanced over thermal levels, often by plasma instability processes (*Fejer and Kelley*, 1980). Studies have shown that when small scales are concerned, with wavelength less than 1 km in the direction perpendicular to the Earth's magnetic field, various plasma instabilities (*Fejer and Kelley*, 1980; *Kelley*, 1989; *Tsunoda*, 1988), namely, Farley Buneman (FB) and the gradient drift (GD) plasma instabilities are produced (*Buneman*, 1963; *Farley*, 1963). These instabilities primarily are excited by the relative background drift between electrons and ions.

Radars rely on these irregularities for the generation of echoes (scattered) from within the ionosphere. Plasma instability is one such process that can cause irregularities observed by radars. Meteors and neutral turbulence below 110 km are other processes. As stated in Chapter 1, the irregularities at near ranges are not field-aligned and the echoes detected may not always be generated by plasma instabilities. While this is the case, it is important nevertheless to consider all possibilities. For instance, *Dimant and Sudan* (1995a,b, 1997) have argued that plasma instability as low as 90 km is possible. This chapter discusses the major theories of the generation of plasma wave-like irregularities.

4.1 E Region Irregularities: Farley-Buneman and Gradient Drift Mechanisms

Farley (1963) and *Buneman* (1963) have shown that the plasma is unstable against the modified two-stream instability, which was later termed the Farley-Buneman (FB) instability, if there is a strong enough background electric field. The motion of the electrons is assumed to be very fast compared to that of the ions that are collisionally dominated. Thus the relative velocity drifts that exists between electrons and ions is given by:

$$\mathbf{v}_d = \mathbf{v}_e - \mathbf{v}_i \tag{4.1}$$

Early works of *Farley* (1963) and *Buneman* (1963) have shown that the excitation of the modified two-stream instability occurs when the drift velocity of electrons relative to ions (Equation (4.1)) exceeds a threshold value in the order of the ion-acoustic velocity:

$$C_s \;=\; \sqrt{[k_B(T_e + T_i)/m_i]} \tag{4.2}$$

where k_B is the Boltzmann's constant, the ion mass is m_i, and T_e is the electron temperature while T_i is the ion temperature.

4.1.1 Dispersion Relation for FB and GD Instabilities

For the mathematical treatment of plasma instabilities, the medium is initially considered homogeneous when a small sinusoidal wave perturbation is introduced. It becomes possible to derive the phase velocity and the growth rate of the wave. In the isothermal fluid approximation (where temperature fluctuations are neglected), the continuity and the momentum equations for both electrons and ions (*Fejer et al.*, 1984; *Sudan et al.*, 1973) are:

$$\frac{\partial n_e}{\partial t} \;+\; \nabla \cdot (n_e \mathbf{v}_e) \;=\; 0 \tag{4.3}$$

$$\frac{d\mathbf{v}_e}{dt} \;=\; -e\,(\mathbf{E} + \mathbf{v}_e \times \mathbf{B}) - \frac{K_B T_e}{m_e}\frac{\nabla n_e}{n_e} - \nu_e \mathbf{v}_e \tag{4.4}$$

$$\frac{\partial n_i}{\partial t} \;+\; \nabla \cdot (n_i \mathbf{v}_i) \;=\; 0 \tag{4.5}$$

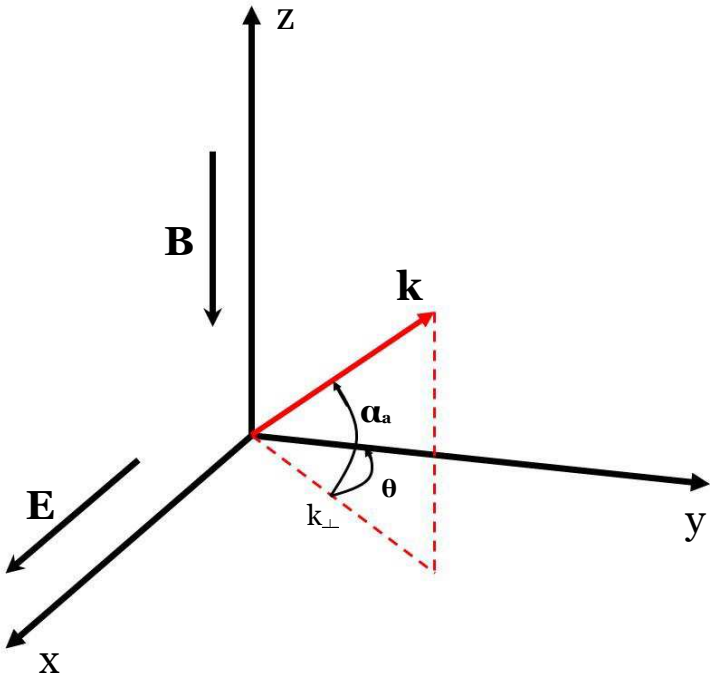

Figure 4.1: Geometry for the coordinate system used for the electric and magnetic fields. Electric field **E** is parallel to the x axis and the geomagnetic field **B** is anti-parallel to the z axis. α_a and θ are the aspect and flow angles respectively.

$$\frac{d\mathbf{v}_i}{dt} = e\mathbf{E} - \frac{K_B T_i}{m_i}\frac{\nabla n_i}{n_i} - m_i \nu_i \mathbf{v}_i \tag{4.6}$$

where n_e and n_i are the density of electrons and ions respectively; $\mathbf{v}_e$ and $\mathbf{v}_i$ are the drift velocities for electrons and ions, m_e and m_i are masses of electrons and ions, respectively; ν_e and ν_i are the electron and ion neutral-collision frequencies respectively; **E** and **B** are the electric and magnetic fields respectively. According to small perturbation theory, the density, velocity and electric field contain a background and a perturbed quantity. That is:

$$n_\alpha = n_{0\alpha} + n_{1\alpha};\ \ \mathbf{v}_\alpha = \mathbf{v}_{0\alpha} + \mathbf{v}_{1\alpha};\ \ \mathbf{E} = \mathbf{E}_0 + \mathbf{E}_1 \tag{4.7}$$

where α particle has as subscripts e, i for electrons and ions respectively. Equations (4.3) to (4.6) can be linearized using the assumption that the plasma is quasi-neutral, that is $n_e = n_i = n$; the electric field is electrostatic, that is, the fluctuations from the magnetic field are neglected, so no quantities depend on the field-aligned coordinate; the time derivative term in Equation (4.4) can be neglected, because to a good approximation, ion inertia is much larger than the electron inertia; deep in the E region, the ions are unmagnetized since their gyro-frequency, Ω_i, is much smaller than the ion-neutral collision frequency. We use

a Cartesian coordinate system according to Figure 4.1, with the magnetic field anti-parallel to the z direction, and the x axis is parallel to the electric field. The aspect angle α_a is the angle between $\mathbf{k}$ and $\mathbf{B}$-perpendicular plane and the angle between the drift velocity in y axis and the $\mathbf{k}$ vector is θ. The Cartesian components of $\mathbf{k}$ are given as:

$$k_x = k_\perp \sin\theta \tag{4.8}$$

$$k_y = k_\perp \cos\theta \tag{4.9}$$

$$k_z = k_\parallel = k \sin\alpha_a \tag{4.10}$$

$$k_\perp = k \cos\alpha_a \tag{4.11}$$

Using a wave decomposition of the form exp $i(\mathbf{k}\cdot\mathbf{r} - \omega t)$ on Equations (4.3) to (4.6) and linearizing, the perturbed ion and electron velocities can be solved to obtain the general dispersion relation (*Sudan et al.*, 1973):

$$\omega - \mathbf{k}\cdot\mathbf{v}_d = \frac{\Psi}{\nu_i}\left[\omega(i\omega - \nu_i) - ik^2C_s^2\right]\cdot\left(1 - \frac{i\Omega_e}{\nu_e k L}\right) \tag{4.12}$$

Here, $\mathbf{v}_d$ is the drift velocity of the electron in the y direction, $L = n_0(\delta n_0/\delta x)^{-1}$ is the scale length of the zeroth order density gradient. When the density gradient is ignored (i.e., $L \to \infty$) for a homogeneous plasma, the Farley-Buneman instability condition for growth rate is obtained:

$$\omega - \mathbf{k}\cdot\mathbf{v}_d = \frac{\Psi}{\nu_i}\left[\omega(i\omega - \nu_i) - ik^2C_s^2\right] \tag{4.13}$$

Therefore, in the gradient-free case ($L \to \infty$),

$$\omega(\omega + i\nu_i) + i\frac{\nu_i}{\Psi}(\omega - \mathbf{k}\cdot\mathbf{v}_d) - k^2C_s^2 = 0 \tag{4.14}$$

4.1.2 Expressions for Growth Rate and Threshold Condition, Flow and Aspect Angle Cones

The angles α_a and θ are given by:

$$\sin\alpha_a \equiv \frac{k_\parallel}{k} \tag{4.15}$$

and

$$\cos\theta = \frac{\mathbf{k}\cdot\mathbf{v}_d}{kv_d} \tag{4.16}$$

The parameter Ψ (from Equation (4.12)) depends on the ratio of local collision and gyro-frequencies and the aspect angle as (*Sudan et al.*, 1973):

$$\Psi \;=\; \psi\left(\frac{k_\perp^2}{k^2} + \frac{\Omega_e^2}{\nu_e^2}\frac{k_\parallel^2}{k^2}\right) \;\approx\; \psi\left(1 + \frac{\Omega_e^2}{\nu_e^2}\sin^2\alpha_a\right) \tag{4.17}$$

where $\psi = \nu_e\nu_i/\Omega_e\Omega_i$ is typically $\ll 1$. By setting $\omega = \omega_r + i\gamma$, (where ω_r is the real part and the imaginary part, γ is the growth rate (s^{-1})) in Equation (4.12) and assuming that the growth rate is slow (thus, restricting the consideration to $\gamma \ll \omega_r$) (*Sudan*, 1983a), the following is obtained:

$$\omega_r \;=\; \frac{\mathbf{k}\cdot\mathbf{v}_d}{(1+\Psi)} \;=\; \frac{k\,v_d\cos\theta}{(1+\Psi)} \tag{4.18}$$

and a solution for the growth rate is given as:

$$\gamma \;=\; \frac{\Psi}{1\;+\;\Psi}\left[\frac{1}{\nu_i}(\omega_r^2 \;-\; k^2\,C_s^2) \;+\; \frac{\Omega_e\omega_r}{\nu_e k L}\right] \tag{4.19}$$

The threshold condition for the instability is satisfied when $\gamma = 0$. According to Equation (4.19), the instability will grow when the wave's frequency is greater than the ion acoustic speed in the gradient-free case ($L \to \infty$). Thus, when v_d exceeds the threshold as:

$$v_d > C_s(1+\Psi), \tag{4.20}$$

or in terms of flow angle

$$v_d\cos\theta \;=\; C_s(1+\Psi), \tag{4.21}$$

the instability is excited. For a simplified case where aspect angle $\alpha_a = 0$, we have that $\Psi \equiv \psi[\cos^2\alpha_a + (\Omega_e^2/\nu_e)\sin^2\alpha_a]$ from Equation (4.17), which becomes $\Psi(\alpha_a = 0) = \psi$. It implies that for the smallest drift velocity ($v_d \propto E$) for which γ vanishes, the corresponding electric field

$$E \;=\; v_d B \tag{4.22}$$

This is called the Farley-Buneman threshold electric field for the background and the threshold velocity is given as $v_d^{th} \geq C_s(1+\psi)$. ψ is small at 100 km and using ion-acoustic velocity of 400 m s^{-1} in Equation (4.22), the electric field must be >20 mV m^{-1}.

The gradient-drift instability, unlike the Farley-Buneman mechanism does not need a strong electric field, and is therefore not related to a particular threshold electric field. The

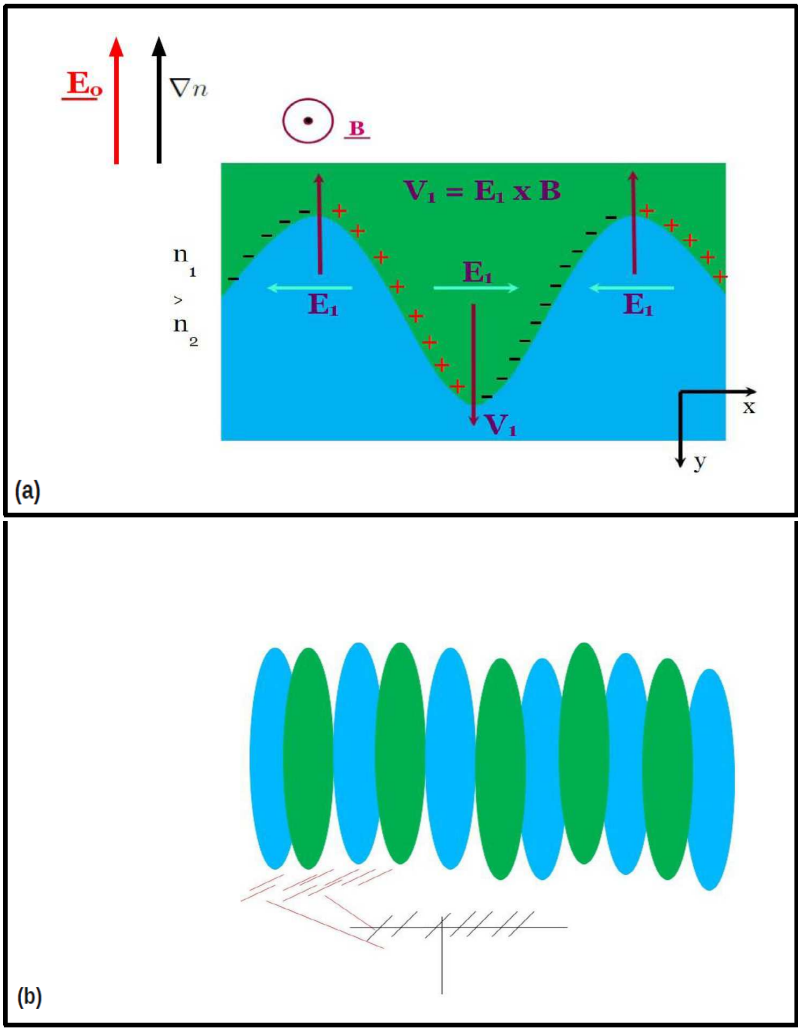

Figure 4.2: A simplified representation of the gradient drift instability showing the electric field, **E** and the density gradient, ∇n conditions (left) in the E region of the ionosphere. The magnetic field, **B** is out of the page. a). Two different regions of plasma density with $n_1 > n_2$ and the electric field is parallel to the density gradient. With small distortion applied to the plasma, a polarization electric field, $\mathbf{E}_1$ is created. Regions of low density are moved to regions of high density (and vice versa) result from ambient **B** and the $\mathbf{E}_1$ created. The plasma is disturbed after some time into elongated blob-like structures. b) Edges of blob-like structures scatter portions of the radio waves transmitted by coherent radars, (*Adapted from (Gillies, 2012)*).

growth rate however is controlled by the electron density gradient scale length. So this instability is excited whenever there is an electric field component that is parallel to the density gradient. The mechanism involve in generating the gradient drift instability in the E region is well explained with the help of the geometry presented in Figure 4.2. Let us examine the boundary between two regions of different densities n_1 and n_2, (heavy density (n_1) is on top of lighter density (n_2) and density gradient is ∇n). The magnetic field is out of the page (in the positive z direction). Assume that the ambient electric field, $\mathbf{E}_0$ is parallel to the density gradient ∇n, (the condition for instability growth in the E region is satisfied if the electric field is parallel to the plasma density gradient) (*Blix et al.*, 1994). If a small disturbance (or perturbation) is introduced in the plasma (wavy curve in Figure 4.2(a)), a polarization electric field $\mathbf{E}$ develops due to the charge separation owing to different drift velocities and directions between the electrons and ions. In the presence of the magnetic field, the resulting polarization electric fields will produce a perturbed $\mathbf{E} \times \mathbf{B}$ drift in a direction towards the bottom of the page in Figure 4.2. As shown from Figure 4.2(a), for an initial small distortion, the perturbed electric field within the structure will cause the higher density structure to break down into small fingers. After sufficient time, the finger-like elongated structures will separate and form blobs of high density in the low density regions and holes in the high density regions, leading to the growth of $\delta n/n$. With radars Fourier analyzing the plasma, these blobs with steeper slopes, will become more visible to the coherent radar systems (Figure 4.2(b)).

Equation (4.18) is also obeyed by the phase velocity of the irregularities, but their growth rate (Equation (4.19)) contains the additional term, L, that depends on the density gradient scale length. The density gradient term in Equation (4.19) is important at long wavelengths (i.e., with small k). We can return to the growth rate equation (Equation (4.19)) and neglect the FB term (i.e. for $v_d \ll C_s$) so that the necessary condition for this instability to occur ($\gamma(k) \geq 0$) is given by:

$$v_d \;\geq\; L\frac{\Omega_i}{\nu_i^2}(1+\psi)\psi k^2 C_s^2 \tag{4.23}$$

where we assumed that $\mathbf{k} \parallel \mathbf{v}_d$. Note that since this instability can only be excited when the gradient L has a component that is parallel to the electric field, L must be positive. Consider when the drifts are slightly below the FB instability threshold, i.e. $v_d < C_s(1+\psi)$.

There will still be instability (positive growth rates) if $1/L$ is quite large and positive. But for this case, we can learn from Equation (4.23) that the gradient drift instability will occur for a certain range of wave numbers k. When this equation was examined, typical values were used for different parameters involved at 100 km. With $\Omega_i = 180$ s^{-1}, $\Omega_e = 10^7$ s^{-1}, $\nu_i = 5.2 \times 10^3$ s^{-1}, $\nu_e = 5.2 \times 10^4$ s^{-1}, then $\psi = 0.15$ and $C_s = 360$ m s^{-1}. Assuming $v_d \ll C_s$, and that $v_d = 50$ m s^{-1}, the corresponding electric field is ∼2-3 mV m^{-1} (*Blix et al.*, 1994). Under these conditions for L values of say 10, 30, 60 km, the only waves that may be excited are those whose wavelengths are larger than ∼ 35, 60 and 85 m respectively. This goes to show that at larger wavelengths (scales of tens of meters or larger), the gradient drift instability becomes most effective with the density gradient component parallel to the electric field (*Blix et al.*, 1994).

4.1.3 Regarding Large Aspect Angle Effects

Non-field-aligned-irregularities related to plasma instabilities are observed a few degrees away from the perpendicularity, even though linear theory predicts that these modes should not grow. In particular, *Milan et al.* (2004) using SuperDARN radars observed *high aspect irregularity region* (HAIR) echoes at the same time as the normal echoes. This is not only observed by SuperDARN HF radars. Much higher frequency radars have reported aspect angles as large as 10° away from perpendicularity and these waves were also clearly related to the usual FB instability (e.g. *Jackel et al.*, 1997; *Moorcroft*, 1996). *Drexler and St Maurice* (2005) showed that the aspect angle of Farley-Buneman and gradient drift waves increases monotonically with time because of the systematic change in the eigenfrequency with position along the magnetic fields (or height, in the high latitude situation). This means that the evolution of the structures continues after they have reached a maximum amplitude; that is to say, they decay without having to suddenly crash once they have reached their maximum amplitude.

4.1.4 Lower E Region Instabilities and Related Processes

The concept behind the FB and GD instabilities has been discussed by various authors (e.g. *Buneman*, 1963; *Farley*, 1963). It was demonstrated that the strong gradients of background electron density can modify the properties of the waves for small electric fields. For altitudes above ∼100 km, $\psi \approx 0$ due to the small collision frequencies (ν_e, ν_i) with altitude. The Farley-Buneman instability is excited when $v_d \geq C_s(1 + \psi)$. Such velocities (through the action of $\mathbf{E} \times \mathbf{B}$), are achieved in the auroral E region in the presence of large electric fields. Note that ψ increases rapidly with decreasing altitude below 100 km due to increasing collision frequencies. In this case, the threshold condition in Equation (4.20) becomes difficult to fulfill. As a result of the enhanced collisions in the lower part of the E region of the ionosphere, the field-aligned ionospheric structures responsible for aspect-sensitive auroral backscatter are more difficult to excite (require stronger electric fields).

Dimant and Sudan (1995a,b, 1997) have stressed that, under strong electric field conditions, the lower E region between 90 and 100 km, can produce irregularities that are excited with Doppler shifts much smaller than the ion-acoustic speed. Therefore, for echoes at close ranges to the radar's field-of-view (FOV), these irregularities might be detected under unusual conditions, namely, strong electric fields and relativistic electron precipitation. This is something that could happen, but only very infrequently and only in auroral storm regions.

Regarding the slow growth rate of FB structures, *Drexler and St Maurice* (2005) found that the time scale involved is typically less than 1 second for the aspect angle to create decaying conditions owing to aspect angles that are becoming too large for growth. This implies that, unless the electric field is greater than 40 mV/m, we should not expect FB waves to grow at 10 m. This leaves gradient-drift waves as the mechanism of choice. In an attempt to account for the processes that saturate the wave amplitude, *Sudan* (1983a) suggested that electrons could be scattered by the perturbation electric field created by an irregularity, which effectively enhances the diffusion coefficient and provides a saturation effect. Concerning slowly growing instabilities, *Sudan* (1983b) reported that mode-coupling effects can govern the evolution of gradient drift instability. The mode-coupling should lead to cascading of energy towards smaller wavelengths which should in turn produce isotropic

turbulence in the plane perpendicular to the magnetic field (*Drexler et al.*, 2002). Therefore, not only are irregularities controlled by the linear instability mechanism which produces them, they are also influenced by interactions with waves at other wavelengths and directions.

In addition to non-field-aligned irregularities below 100 km altitudes, the motion of the neutral atmosphere can also be a possible source of energy for the generation of ionospheric irregularities. Studies in the past have hypothesized the possibility of excitation of plasma irregularities by turbulence within the neutral winds. This is reasonable as both the electrons and ions in th D region below 100 km are collision dominated, and they will carry the signal of any turbulent motion of neutrals. This theory was proposed by *Gurevich et al.* (1997) and was supported by some observations (*Rüster and Schlegel*, 1999; *Schlegel and Gurevich*, 1997).

Chapter 5
REVIEW OF PREVIOUS STUDIES ON CLOSE-RANGE ECHOES

As reported in the literature, radar returns or reflections from the lower ionosphere can be broken into three types, namely, meteor echoes, polar mesosphere summer echoes and unusual echoes from E region plasma instability echoes. This chapter discusses the three mechanisms in the light of previous efforts employed to understand and explain them.

5.1 Meteor Echoes Background Information

"Meteor trails" are caused by the entrance of macroscopic particles from space (meteoroids or space debris) into Earth's atmosphere. This phenomenon occurs as particles are heated up due to collisions with air molecules and when they reach high enough temperature, they lose atoms and molecules by evaporation and spallation. This process is called "ablation". Subsequent collisions between meteoroid atoms and air molecules produce ionization. As excited atoms lose energy, they emit light (Figure 5.1). In addition, the meteoroids produce long columns of ionization. We can therefore observe meteor trails by detecting the luminosity from these light-emitting meteoric atoms or by scattering radio waves from these ionization trails (*McKinley*, 1961).

Five stages of interaction can occur between the meteoroids and the Earth's atmosphere. First is *meteoroid motion* (orbital motion) which is followed by *preheating* stage. The preheating stage is a result of the meteoroid impacting the molecules of the gas in the Earth's atmosphere. This phenomenon only lasts for some seconds or tens of seconds. The meteoroid surface temperature rises rapidly. The third stage is the atmospheric penetration, known as

Figure 5.1: Meteor trail animation (*http://apod.nasa.gov/apod/ap011122.html*).

the *ablation* stage. This involves evaporation of molecules/atoms from the body and from its fragments; temperatures reaching about 2500 K. Most of the kinetic energy has been used in the ablation process and so no further increase in the temperatures occur. At the end, the gases around the body is not hot enough to emit visible light, so they undergo *dark-flight* which is the fourth stage. Finally, and very rarely, the residual debris of the large meteoroid may survive the fiery plunge and falls to the ground as a *meteorite*, usually breaking up into many small pieces (*Ceplecha et al.*, 1998; *McKinley*, 1961).

Meteors can be observed at any time of the day or night. However, more meteors can be seen around early dawn than any other time. A simple explanation for this has to do with the rotation of the Earth. The orbital motion of the Earth is in the same direction as the dawn sky, (Figure 5.2). Following sunset, the meteors are basically on the trailing edge of our planet as it moves around the Sun. After midnight, the Earth's rotation has now placed the meteors on the leading edge of our planet as it moves around the Sun. This means that the dawn sky is moving directly into the swarm of space dust surrounding our

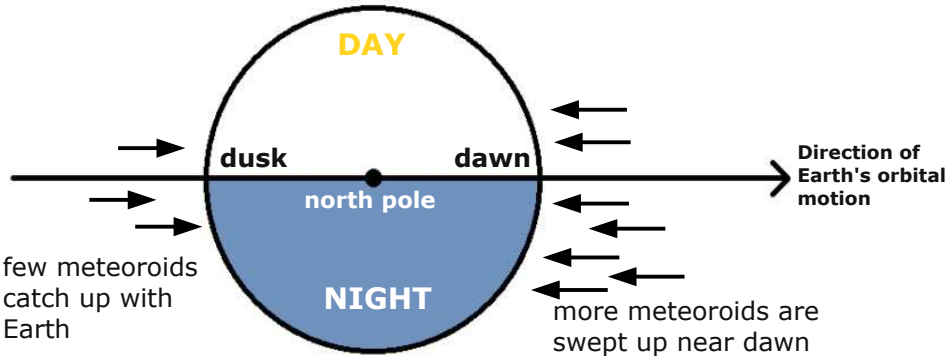

Figure 5.2: Illustration showing that more meteors are observed near dawn due to the orbital motion of the Earth in the direction of the dawn terminator. For Earth tend to scoop up meteoriods on the dawn side of the Earth and move faster than those on the dusk side.

planet. The Earth is now sweeping up the slow particles, while the faster particles moving toward the Earth are entering the atmosphere at much higher speed than before midnight. This is analogous to the splatter of bugs on the front windshield of a moving vehicle, with no bugs on the rear windshield. In the same way, lots of meteoroids strike the dawn sky but not very many can catch up with the atmosphere at dusk. So if we consider a single point of latitude and longitude on the Earth, during the local morning hours, that point has moved towards the streams of meteors and the Earth which has the effect of sweeping off space debris, sweeps off any meteor activity. In the local evening hours however, this point will in effect be moving away from the stream of meteors and this will in effect lead to the observed decrease in the meteor detection during the local evening hours (*Singer et al.*, 2004).

5.1.1 Meteor Trail Diffusion Dynamics

Meteors with higher entry velocities during their passage through the Earth's atmosphere will be heated more strongly and thus ablate more quickly and produce denser ionization trials than those with low velocities. During their passage through the Earth's atmosphere, there is a quick compression of air in front of the meteor. There is instant heating of the air to temperatures that are high enough to ionize it. The combination of heat and friction completely ablates most of the meteors before they reach the ground. The plasma in the trail is what makes it possible for returned signal at the ground to be received by a radar.

The thermal velocity of ions is much lower than that of electrons at the same temperature, since the ions in the meteor trail are much heavier than the electrons. So one might expect that the diffusion of electrons would be faster than that of ions. However, ions and electrons actually diffuse at the same rate, because of the polarization fields that are set up when electrons are trying to run away. Ambipolar diffusion is then used to refer to such diffusion of charged particles. As a result, both ions and electrons diffuse at a rate that is somewhere between the rate that one diffuses without the other.

There is a fading away and an eventual disappearance of reflected power of a meteor trail. Diffusion is the movement of atoms or molecules from an area of higher concentration to a region of lower concentration. This diffusion process continues until there is balance between the difference in the concentrations, thereby removing the gradient that is needed to reflect the radar signal. The thermal motion of particles drives the diffusion. Since diffusion does not depend on the magnitude of concentration, it is easy to link the speed of the diffusion to the temperature (as discussed in more details in section 5.1.4 below). Thus, the meteor trail subsequently diffuses and drifts in the atmosphere. The fundamental basis of meteor radars make use of these physical processes in derivation of mesospheric winds and temperature. With the aid of meteor radars, meteor echoes are classified as either overdense or underdense (*Ceplecha et al.*, 1998; *Thomas et al.*, 1988).

5.1.2 Underdense Meteor Echoes

The underdense meteor echo occurs when the electron density in the trail is so low that the radio wave is not reflected at the surface but rather penetrates into the trail and scatters from the individual free electrons. These meteors are much more numerous than the overdense meteors and can last for less than 1 second. Thus for a typical underdense meteor echo (*McKinley*, 1961):

- A radio wave is not reflected by the trail.
- The trail is formed "instantaneously" over the radar's field of view.
- The line density (i.e. the number of charged ions per unit meter) of the trail is $\leq 10^{14}$ C/m.

- The diameter of the trail is less than or equal to half the radar's wavelength (i.e. $\leq \lambda_{radar}/2$, where λ_{radar} is the radar wavelength).

- The trail has a life time of less than one second. Some of the radiation of the electrons is backscattered to the radar, and when this happens, the signal received increases for a few hundredths of a second, and then decays exponentially.

Normally, the underdense meteors weigh less than 10^{-6} kg and have a radius $< 10^{-3}$ m (*Havnes and Signernes*, 2005). The line charge density is one of the main properties used in the classification of meteor trails. It is a measure of the number of charges per unit length contained within the trail volume along the axis of the trail. It is assumed that the line charge density is constant along the trail axis, near the point where the radar signal intersects and is scattered from the trail.

5.1.3 Overdense Meteor Echoes

Overdense meteor echoes are very strong echoes. Though rare, they can last for several seconds. The number of electrons produced per meter of path length in the overdense meteor trail is large enough that it totally reflects the radio wave signal. So the radio wave does not penetrate the column. The electron line densities for overdense echoes are greater than 10^{14} C/m, and their echo characteristics are similar to that of a hard target since the incident radio waves are unable to easily penetrate the trail (*McKinley*, 1961). The overdense meteors are likely to be large as the electron densities within the trails are high. As the trail diffuses, the overdense part expands, thus creating a larger surface available to reflect the radar beam. This expansion will eventually cause the electron density to decrease to a level that is insufficient for surface reflection.

5.1.4 Meteor Decay Time and Ambipolar Diffusion Coefficient Estimates

As previously mentioned, the majority of the meteor echoes observed by radars produce underdense echoes. After a meteor has produced a trail, the most important factor in reducing

the echo strength is ambipolar diffusion. Ambipolar diffusion reduces the density volume without affecting the line density (*McKinley*, 1961). The echo decay time and the diffusion coefficient can be derived. For simplicity, let's start with the continuity equation. The continuity equation accounts for transport induced by diffusion. The transport of electrons and ions across the axis of the meteor trail is due to the self generated ambipolar electric field. The continuity equations for both electrons and ions can be written as (*Choudhuri*, 1998):

$$\frac{\partial n_e}{\partial t} = -\nabla \cdot \Gamma_e = -\nabla \cdot (-D_e \nabla n_e - \mu_e E_a n_e) = D_e \nabla^2 n_e + \mu_e E_a n_e + \mu_e n_e \nabla \cdot E_a \quad (5.1)$$

$$\frac{\partial n_i}{\partial t} = -\nabla \cdot \Gamma_i = -\nabla \cdot (-D_i \nabla n_i + \mu_i E_a n_i) = D_i \nabla^2 n_i - \mu_i E_a n_i - \mu_i n_i \nabla \cdot E_a \quad (5.2)$$

where E_a is the ambipolar electric field, the electron and ion densities are n_e and n_i respectively, Γ_e and Γ_i are the electron and ion fluxes, μ_e and μ_i are the electron and ion mobilities and D_e and D_i are the electron and ion diffusion coefficients respectively. $\nabla \cdot E_a = q(n_i - n_e)/\varepsilon \approx 0$. Therefore Equations (5.1) and (5.2) become:

$$\frac{\partial n_e}{\partial t} = D_e \nabla^2 n_e + \mu_e E_a \nabla n_e \quad (5.3)$$

$$\frac{\partial n_i}{\partial t} = D_i \nabla^2 n_i - \mu_i E_a \nabla n_i \quad (5.4)$$

We can multiply Equation (5.3) by μ_i and Equation (5.4) by μ_e, and add them together while assuming that $n_e = n_i = n$ (charge neutrality), $\frac{\partial n_e}{\partial t} = \frac{\partial n_i}{\partial t} = \frac{\partial n}{\partial t}$, $\nabla n_e = \nabla n_i = \nabla n$ and $\nabla^2 n_e = \nabla^2 n_i = \nabla^2 n$, we then obtain:

$$\mu_i \frac{\partial n}{\partial t} = \mu_i D_e \nabla^2 n + \mu_i \cdot \mu_e E_a \nabla n \quad (5.5)$$

$$\mu_e \frac{\partial n}{\partial t} = \mu_e D_i \nabla^2 n - \mu_e \cdot \mu_i E_a \nabla n \quad (5.6)$$

We then obtain:

$$\frac{\partial n}{\partial t} = \left(\frac{D_e \mu_I + D_i \mu_e}{\mu_e + \mu_i} \right) \nabla^2 n = D_a \nabla^2 n \quad (5.7)$$

where the ambipolar diffusion coefficient is:

$$D_a = D_i \frac{\left(1 + \frac{D_e}{D_i} \frac{\mu_i}{\mu_e}\right)}{\left(1 + \frac{\mu_i}{\mu_e}\right)} \quad (5.8)$$

Using the Einstein relation $D = (k_B T)\mu/q$ (k_B is the Boltzmann constant, T is temperature), and assuming that $\mu_e >> \mu_i$, we then have:

$$D_a = D_i \frac{\left(1 + \frac{T_e}{T_i}\right)}{\left(1 + \frac{\mu_i}{\mu_e}\right)} \approx D_i \left(1 + \frac{T_e}{T_i}\right) \tag{5.9}$$

Both electrons and ions appear to diffuse with the same coefficient, D_a which includes the effects of both their own free diffusion. From Equation (5.7), we can solve for the decay time by using $\nabla = ik$, and $\nabla^2 = -k^2$, so that,

$$n = n_o e^{-k^2 D_a \tau} \tag{5.10}$$

$$k^2 D_a = \frac{1}{\tau} \tag{5.11}$$

with $k = 2\pi/\lambda$ and $\lambda = \lambda_{radar}/2$, ($\lambda_{radar}$ is the radar wavelength) we have that the decay time constant therefore is:

$$\tau = \frac{\lambda_{radar}^2}{16\pi^2 D_a} \tag{5.12}$$

where D_a is the ambipolar diffusion coefficient which is the rate at which the meteor echoes decay in the atmosphere and is independent of all parameters except wavelength. The diffusion is related to temperature (from Equation (5.9)) as (*Arnold et al.*, 2001):

$$D \propto \frac{T_i + T_e}{\nu_i} \tag{5.13}$$

where T_i and T_e are the ion and electron temperatures respectively, and ν_i is the ion-neutral collision frequency. T_i and T_e increase with height in the thermosphere, and the ν_i decreases with height. Owing to the latter, the diffusion coefficient increases roughly exponentially with height in the meteor region (*McKinley*, 1961). It should be pointed out that different definitions for the decay times have been used by some authors. For instance, previous authors (*Hocking et al.*, 1997) have defined the decay time as the time it takes for the amplitude to fall to half its original value.

The above analysis is assumed to be valid only when the expansion of the trail is influenced by ambipolar diffusion alone. Several processes have been known to influence the dissipation of the meteor trails. The results of *Dyrud et al.* (2001) and *Hall* (2002) have shown that the density gradients at the edges of the meteor trails, drive instabilities which

Table 5.1: Height estimates of occurrence for SuperDARN Near Range Echoes (Table 2 of *Hall et al.* (1997))

Measurements	Source of Estimate	Height, km
a	cross-correlation with Saskatoon MF	80-100
b	spectral comparison with Sask MF	94-106
c	phase of semi-diurnal tide	94 ± 3
d	vertical angle measurement	80-100
e	spectral width peak (Fig. 5 of (*Hall et al.*, 1997))	91 ± 2
f	spectral width mean (Fig. 5 of (*Hall et al.*, 1997))	97 ± 2

in turn create an anomalous diffusion (due to electromagnetic and turbulent effects) that can affect the radar results. This meteor diffusion plays an important role in radar studies since below 90 km, there is an increasing risk in underestimating the decay time as the effect of neutral turbulence may largely contribute to the meteor trail's dissipation (*Hall*, 2002). Recent studies have shown that the decay time for underdense meteor echoes varies depending on the echo strength (*Singer et al.*, 2008). *Singer et al.* (2008) and co-workers also found that the decrease in the decay time of meteor trails (temperatures based on this are larger than from other systems/models) is related to the icy particle occurrence resulting from noctilucent clouds (NLC) near the coldest summer mesopause.

5.1.5 SuperDARN Near-Range Meteor Echoes

Hall et al. (1997) first showed that SuperDARN meteor echoes are returned from ranges <500 km, and they termed these echoes as 'Grainy Near Range Echoes' (GNREs) due to the grainy appearance of the backscatter power variation on the range versus time and intensity plot of echo power (Figure 5.3). The speckled appearance of the near-range echoes occurs randomly in echo intensity. While Figures 5.3a-c show the characteristic speckled appearance, Figure 5.3d shows an expanded time and range scale of Figure 5.3b. *Hall et al.* (1997) concluded that irrespective of whether or not there is magnetic activity and the accompanying auroral irregularities, there is a very steady day-to-day occurrence of GNREs peaking near 0600 LT (or 1200 UT). When the near range echo occurrence for the first five range gates (i.e. range

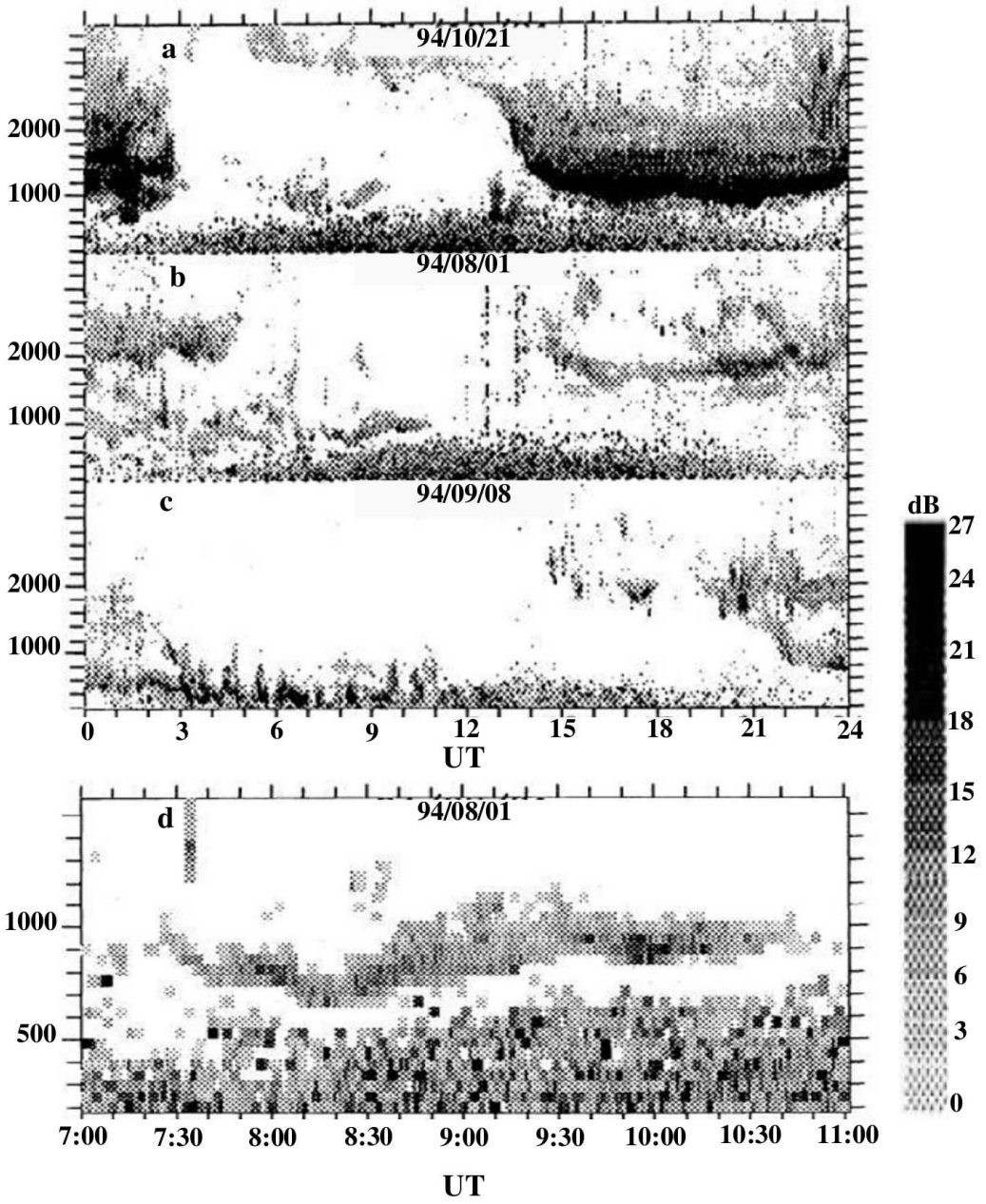

Figure 5.3: Range-Time intensity (power) plots for Saskatoon SuperDARN radar from Beam 5. (a) October 21, 1994 - A day of low magnetic activity K_p and echoes are seen to extend to higher ranges (600 or 700 km) for a few hours centered on 1200 UT (0600 LT); (b) August 1, 1994 - A day of moderate K_p, similar to (a) but with some E region echoes also occurring at range less than 400 km; (c) September 8, 1994 - A day of of high K_p, with echoes obscured by auroral echoes over much of 0000 - 1000 UT time interval, and reduced strength of the GNREs compared to (a) and (b). The decreased strength is attributed to enhanced D region ionization and subsequent absorption of radio waves; (d) Expanded section of Figure 5.3b with range scaling starting at 200 km, showing clearly the speckled appearance, (*Hall et al.*, 1997).

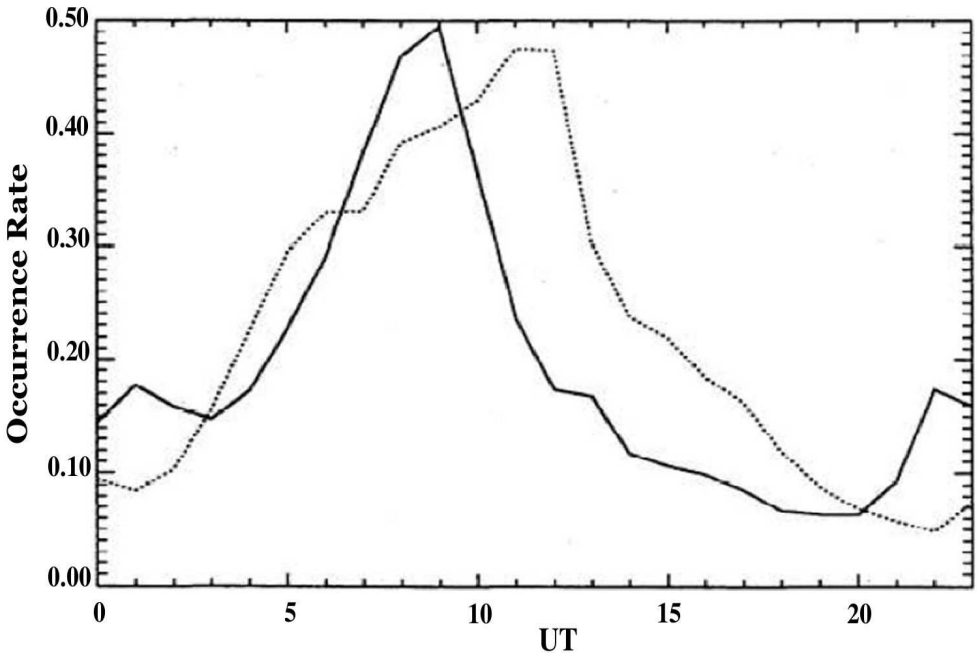

Figure 5.4: Mean diurnal echo occurrence for beam 5 of near range for Saskatoon SuperDARN radar. The solid curve is for the month of May 1994 and dotted curve for October 1994. The fraction of integration period is for signal-to-noise-ratio of at $\geq$10 dB in the nearest five range gates (that is, 180 to 405 km in range), (from (*Hall et al.*, 1997)).

180–400 km) was plotted, an occurrence peak in the morning hours was seen (Figure 5.4). The solid curve is for May 1994 and the dotted curve for October 1994. For both months shown, an occurrence peak around 1200 UT (≡ 0600 LT) is seen, but with 2-hour delay in month of October compared to May. The maximum frequency of occurrence is reaching about 50%. A drop in the echo rate reached 10% during the late afternoon. Thus a diurnal variation of the meteor echo occurrence is seen with a characteristic peak near sunrise, as reported from the discussion of Figure 5.2.

Originally, unlike other dedicated meteor radars, SuperDARN radars were not designed to directly measure meteor echoes decay rates. However, by adjusting the radar control program parameters (such as operating in special mode of high time resolution), the detection rate of the meteors can be enhanced (*Tsutsumi et al.*, 2009; *Yukimatu and Tsutsumi*, 2002). Due to high data volume and processing ambiguity, SuperDARN currently does not run the special high resolution mode. But when a backscattered signal is dominated by a single meteor echo, the ACF determined from the normal SuperDARN operations provides information about the meteor echo decay time. The detected meteor echoes can be used for the estimation of mesospheric winds (*Hussey et al.*, 2002).

The height determination agreed well to an altitude of 94 ± 3 km, which is within the range of height expected for meteor echoes (Table 5.1). Also, the rate of echo occurrence of GNREs agree closely with the predicted number of meteor echoes for a radar with SuperDARN characteristics, and the power of the backscatter of GNREs is found to increase during times of meteor showers (*Hall et al.*, 1997). So these authors concluded that GNREs are due to meteor trails.

5.2 Polar Mesosphere Summer Echoes Background Information

During summer, very strong radar echoes are detected from the mesopause altitudes in the polar regions with vertically sounding radars. These echoes are referred to as *Polar Mesosphere Summer Echoes*, (PMSE) and other visible phenomena such as noctilucent clouds

(NLC) have been closely associated with them.

The transition region between the mesosphere and the lower thermosphere is a transition region that is controlled by a combination of radiative and dynamic forces from above and below. The boundary between the mesosphere and thermosphere is called the mesopause, corresponding to the temperature minimum. Figure 5.5 (top panel) shows the mean seasonal variations of the mesopause temperature and altitude at 69°N. In summer, the temperature of the polar mesopause can be extremely cold with temperature of about 130 K and with mesopause height reaching about 88 km, (bottom panel of Figure 5.5). By contrast, in the winter mesopause, the minimum temperatures reach approximately 190 K and the mesopause location is higher near 98 km (*Lübken et al.*, 1991). As already discussed in section 2.5, atmospheric gravity waves are thought to be responsible for this mesopause circulation. We will next give a brief history of PMSEs observations. It will be followed by the different characteristics of PMSE and the several theories that have been used to explain the phenomena relating to PMSE.

5.2.1 Brief History of PMSE Observations

In 1979, Ecklund and Balsley were the first to make observations of polar mesosphere summer echoes using their Poker Flat 50 MHz VHF (very high frequency) radar in Alaska at altitudes between 80 and 90 km around the summer mesopause region and at the polar and mid-latitudes (*Ecklund and Balsley*, 1981). A few years after the first discovery, in the summer of 1984, *Czechowsky et al.* (1989), observed a similar type of echo with the 53.5 MHz SOUSY (SOUnding SYstem) radar at Andenes in northern Norway (*Czechowsky et al.*, 1989). The PMSE phenomenon became popular among scientists after it was found that the EISCAT radar at 224 MHz also observed strong PMSE echoes at Tromso, Norway (*Hoppe et al.*, 1988). These echoes were soon realized to be confined within high latitudes, hence the name Polar Mesosphere Summer Echoes (PMSE), (*Röttger et al.*, 1988).

More advanced radar experiments and instruments have shed more light on the basic physical theories involved in the generation of PMSE as well as the physical conditions associated with it. Studies have documented the relation between PMSE and other atmospheric phenomena. The existence of small ice particles in the mesosphere has now been connected

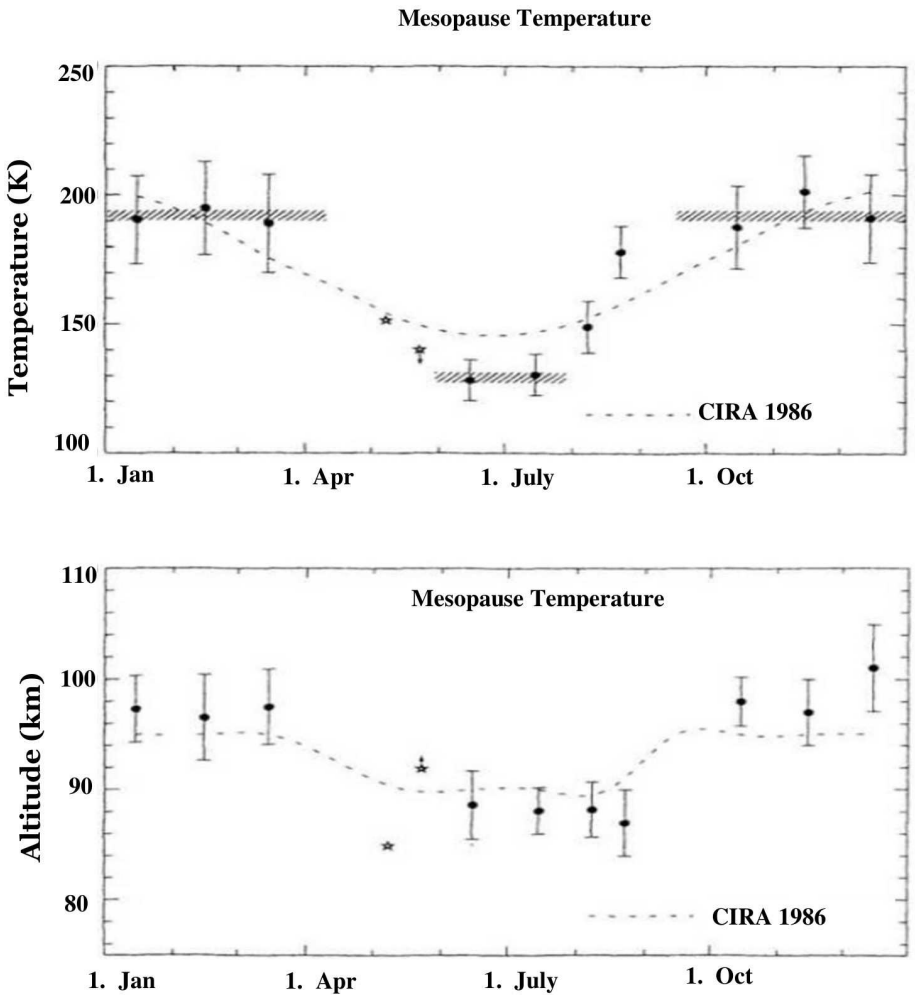

Figure 5.5: Temperature (top) and altitude (bottom) of the mesosphere at 69°N as a function of season. The vertical bars give the variability of the temperature and altitude in that particular month, (*Lübken et al.*, 1991).

with PMSE. These ice particles exist because of extremely cold temperatures during the summer in the mesosphere, when the coldest temperatures of the Earth are observed (*Rapp et al.*, 2004).

5.2.2 Theories and Experimental Information of PMSE

Since its first observation by *Ecklund and Balsley* (1981), many other observations of PMSEs have been made with very high frequency (VHF: 30-300 MHz) (*Röttger et al.*, 1988) and with ultra high frequency (UHF: 300-3000 MHz) (*Hall et al.*, 2001; *Röttger et al.*, 1990) and (*Cho et al.*, 1993). Observations have been made at frequencies in the HF band (3-30 MHz), (e.g. *Kelley*, 2002; *Lee*, 2001). Using radars at even lower frequencies in the medium frequency (MF) bands (300 kHz -3 MHz), (*Bremer et al.*, 1996) have also reported a strong hint of PMSE at 2.7 MHz, (*Vlaskov et al.*, 1995).

The following characteristics are a summary of their many peculiar features:

1. They are thought to be confined to high latitudes in the Northern Hemisphere at ∼65-69°N, 75°N and 78°N (*Lübken et al.*, 2004), they have been observed at several locations in Antarctica. The occurrence rate has been found to be almost 100% at 78°N (*Lübken et al.*, 2004), and ∼90% at 69°N (*Bremer et al.*, 2003).

2. In the Northern Hemisphere, PMSEs have been observed to show semidiurnal variation with maxima at noon (1200-1300 LT) and around midnight and minima near 0600-0700 LT and 1800-1900 LT (*Hoffmann et al.*, 1999). Similar diurnal variation in the Southern Hemisphere have also been observed for seasons of 2004-2005 (*Morris et al.*, 2007).

3. Since their first observation at Poker Flat, Alaska (*Ecklund and Balsley*, 1981), PMSEs have been known for their seasonal variation. In the Northern Hemisphere, PMSE starts appearing in the middle of May, peaks in June until the end of July and then gradually decreases until the end of August (*Bremer et al.*, 2009). Similarly, these summer months are corresponding to November through February in the Southern Hemisphere. This seasonal behavior is mainly explained by the seasonal variation of temperature (*Bremer et al.*, 2003).

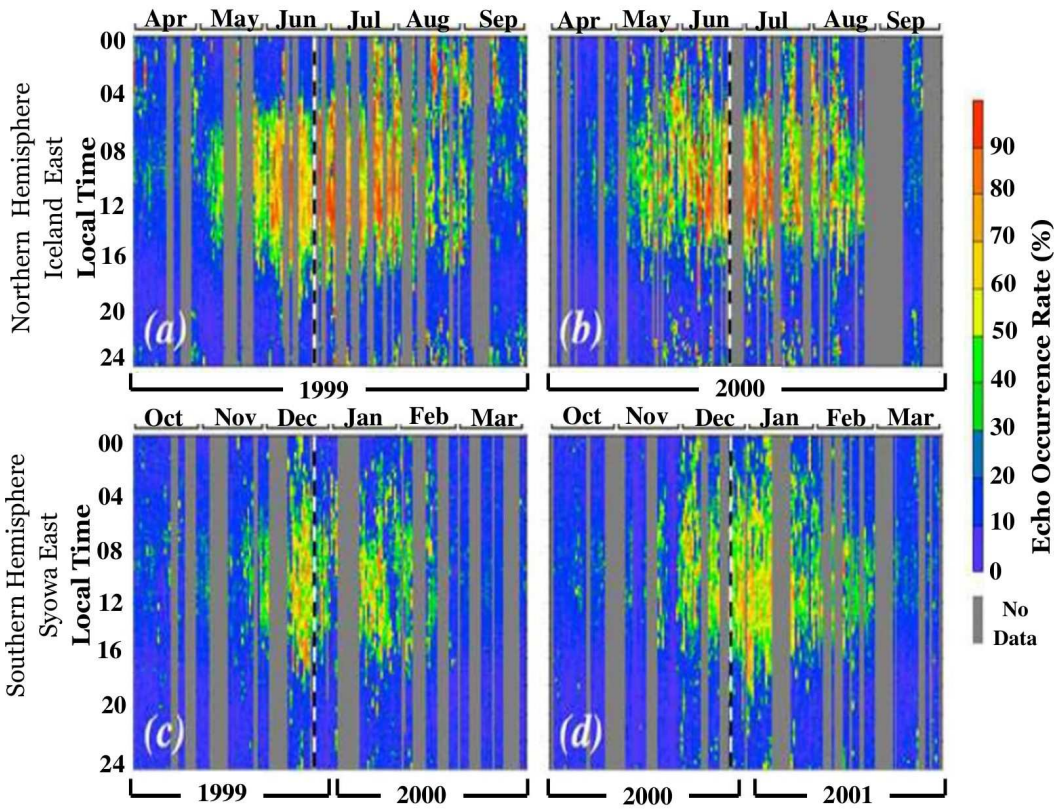

Figure 5.6: Rates of SuperDARN hypothesized PMSE occurrence in summer. Top panel: Iceland East Radar for (a) 1999 and (b) 2000; and lower panel: Syowa East radar for (c) 1999–2000 and (d) 2000–2001 (October to March). Periods with data shown in gray (*Hosokawa et al.*, 2005).

Besides the observations made by HF radars, there are studies done using oblique sounding radars (SuperDARN) (*Hosokawa et al.*, 2004, 2005; *Ogawa et al.*, 2002). The occurrence rates has been found to be ∼10-20% for two mid-latitude radars at 54°N (Figure 5.6). These studies have suggested that the first few range gates of the HF radar are capable of detecting PMSEs. However, these authors based their findings on morphology of the echo occurrence rate alone. More of this will be discussed later.

Various theories have been put forward to explain the PMSE phenomenon. They are divided between turbulent and non-turbulent. The turbulent theories argue that neutral air turbulence creates turbulence in electrons. However, this theory has not been successful. Radar scattering originates in fluctuations in electron density which are directly produced by neutral turbulence. For radar echoes to be detected, half of the radar's wavelength (Bragg's scale) must match the inertial subrange of the turbulent energy spectrum. However, at

mesospheric altitude, say 80 km or so, irregularities with scales of tens of meters should be dissipated by ambipolar diffusion. Hence, if electrons producing the scattering are driven by the turbulence with the same scales as neutrals, ambipolar diffusion should smooth out immediately any fluctuations or irregularities and the radar signals should be very weak.

A non-turbulent theory is based on the dusty plasma scattering concept that requires that dust particles with multiple elemental charges in the mesosphere attract electrons. In order to maintain charge neutrality, the electrons will move in the same direction for a given dust particle, with clouds of opposite charges formed around each dust particle. These clouds formed mainly by electrons are able to scatter radio waves (*Hagfors*, 1992; *La Hoz*, 1992).

All the theories use the fact that the summer mesopause has the coldest temperature in the Earth's atmosphere and that ice particle formation is well linked with PMSE (*Rapp and Thomas*, 2006). These low temperatures lead to the nucleation and growth of ice particles from water vapour at around 85 km (*Witt*, 1962). These ice particles can be seen with the naked eye from the ground as silver-grey pattern known as noctilucent clouds, NLC (Figure 5.7). The first observation of NLC is dated to 1883 (*Leslie et al.*, 1885). They are represented by bands (gravity waves) and they are visible at any area in the twilight sky. The comparison of the seasonal occurrence rate of NLC's and PMSE have shown that NLC appear until the period of lowest temperatures of the summer months and PMSE were also present throughout the day (*Kirkwood*, 1998). Rocket measurements of temperatures reveal the temperature in the NLC layer might be lower than 154 K (*Lübken et al.*, 1996). The existence of strong similarities in occurrence properties between PMSE and NLC layers have been used to support their common origin hypothesis. Moreover, the overlapping altitude of PMSE and NLC appearance and occurrence in the same months make it very likely that both phenomena may have a common origin and are influenced by common processes.

5.3 Ionospheric E Region Echoes

Ionospheric E region echoes are detected at radar frequencies extending from HF at 3-30 MHz, VHF at 30-300 MHz, and UHF at 300-3000 MHz. But HF radars are advantageous over VHF because of their ability to achieve a perpendicularity condition with the magnetic

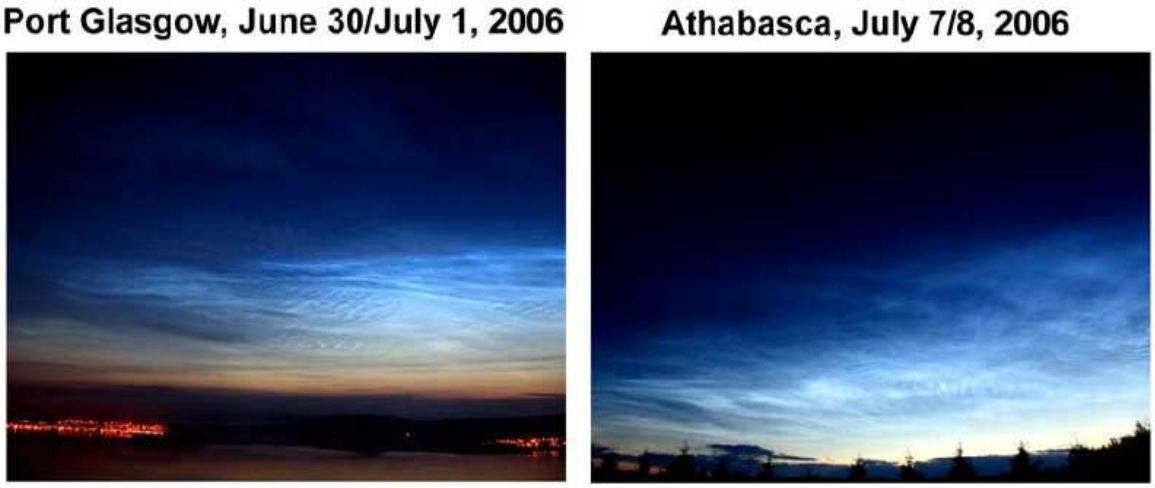

Figure 5.7: Noctilucent Clouds over Glasgow and Athabasca (Courtesy of (*Dalin et al.*, 2008).

field in both the high-latitude E and F regions as the radio wave refract more at lower frequencies than at 30-300 MHz (*Davies*, 1990). Basically, the irregularities producing these echoes are influenced mostly by the Farley-Buneman (*Buneman*, 1963; *Farley*, 1963), and the gradient drift instabilities discussed in Chapter 4 (*Ossakow et al.*, 1979; *Sudan et al.*, 1973). The former occurs when electrons and ions drift with large velocity differences in excess of the ion acoustic speed, and the latter occurs when there is an electron density gradient component that is perpendicular to the drift of the electrons.

5.3.1 Close-Range E Region Echoes

A statistical study of over 20 months for the Co-operative UK Twin located Auroral Sounding System (CUTLASS) radars in Iceland was carried out by *Milan et al.* (1997b). During the summer months, close-range E region echoes were observed predominantly in the midnight local sector. It was concluded that the characteristics of HF wave propagation and the contribution from ionospheric electron density strongly determine the number of echoes observed at any given range. A factor noted by these authors was that, within the polar regions a large seasonal variation in the propagation environments results from constant seasonal illumination in summer months and constant darkness during the winter months. This explained the summer dominance.

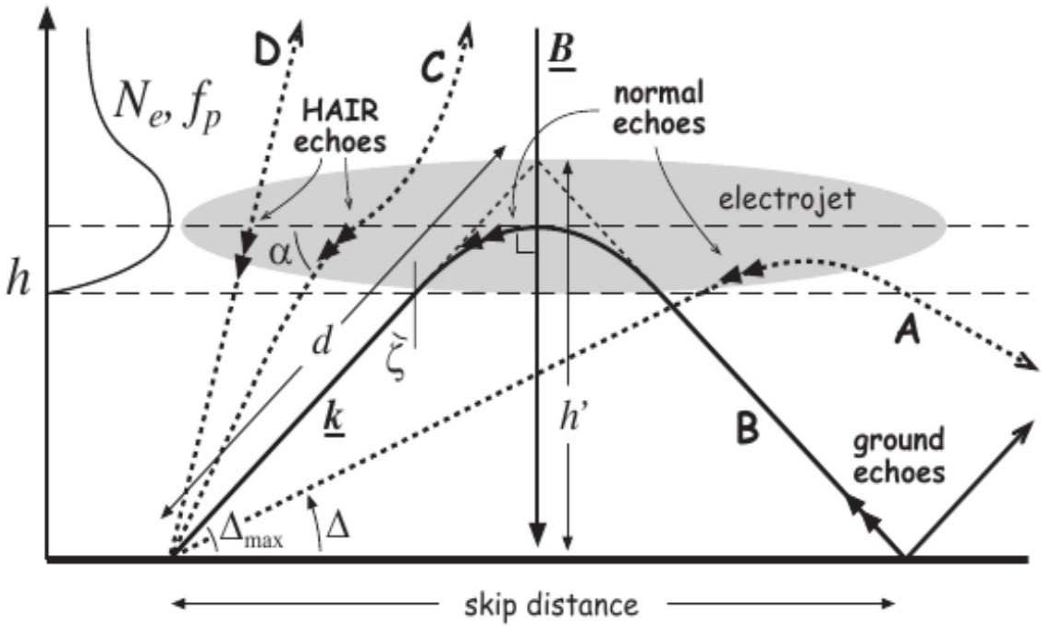

Figure 5.8: Illustration showing HF radio waves propagation in the electrojet region. The double arrows indicate observed backscatter location, whether normal E region, ground echoes, or HAIR echoes (Adapted from (*Milan et al.*, 2004).

Milan et al. (2004) suggested that the short-range echoes may result from non-field-aligned irregularities. They hypothesized that these echoes may arise from high aspect angle scatter, and "high-aspect angle irregularity region" (HAIR), was the term used to classify the region from which they arose.

What makes HAIR echoes different from normal E region echoes is the presence of structures that are apparently not perpendicular to the magnetic field. Figure 5.8 shows how rays that are launched at elevation angles just above Λ_{max} will almost be refracted perpendicular to the magnetic field. (*Milan et al.*, 2004) suggested that HAIR echoes results from high aspect irregularity scatter and their initial estimates inferred aspect angle, α_a with typical value of 10°. These high aspect angle were thought to exist throughout the electrojets. However, they were observed during prolonged periods of high geomagnetic activity, when the auroral oval moves to lower latitudes. And at this time, enhanced particle precipitation in the E region is located in the close-ranges of the field-of-view.

5.4 Summary

The E region ionosphere supports the propagation of radio waves and SuperDARN HF radars have proven to be a powerful tool in detecting backscatter from ionospheric irregularities in the E and F region. The oblique sounding system employed by SuperDARN radars allows the radars to detect echoes at close ranges. The first range gate of these radars covers the slant range between 180–225 km.

The first class, meteor echoes, has been observed before at ranges less that 500 km with maximum intensity near local dawn (*Hall et al.*, 1997). These authors showed that meteor trails can scatter radio waves between 80–106 km, but the returns selected were those with SNR greater than 10 dB. The study by *Chisham and Freeman* (2013) showed the altitude distribution of SuperDARN meteor echoes to be maximum at 102–103 km. However, *Chisham and Freeman* (2013) characterized "meteor echoes" as those having low measurement errors in Doppler velocity and spectral width. Although these studies have shown the capability of SuperDARN HF radar to detect backscatter or reflection from meteor trails, there are still some uncertainties as to the selection criteria and identification of other classes of echoes that have been observed at close-ranges that show seasonal and diurnal dependence.

As for PMSE, their maximum occurrence frequency is near 1200 LT in the summer months. These echoes are distinctly not the same as those observed with meteor echoes that are generally observed at dawn. *Ogawa et al.* (2002) attributed the peculiar near-range SuperDARN HF echoes to PMSE. These authors used four months of data to arrive at their conclusion. Furthermore, like *Ogawa et al.* (2002), *Hosokawa et al.* (2004, 2005) later reported that the close-range echoes observed using the SuperDARN radars are PMSEs, without using the elevation angle information (from the SuperDARN data) to make a firm altitude determination. The authors concluded that the near-range echoes observed in summer were PMSE, thereby basing their conclusion only on the morphology and local time dependence of the echoes. Moreover, instead of a systematic study in comparing results obtained from a chain of radars (in other latitudes) and also in determining the characteristics of these echoes with respect to signal-to-noise-ratio, Doppler velocities and spectral width,

these authors used an extraction procedure of removing backscatter data (termed "meteor echoes") having SNR lesser than 6 dB, a Doppler velocity greater than 50 m s^{-1} and a spectral width greater than 50 m s^{-1}. The SNR criterion is a direct opposite of that employed by *Hall et al.* (1997) who used close-range backscatter with SNR greater than 10 dB to identify meteor trail echoes. These pre-selected criteria were used without any physical justification, leaving many questions to be resolved about the true nature of the echoes.

The HAIR echoes on the other hand are those backscatter echoes whose ionospheric refraction are insufficient to bend HF signals to achieve perpendicularity with the magnetic field. *Milan et al.* (2004) reported this unusual class of ionospheric returns and attributed their origin to non-field-aligned E region irregularities inside the auroral zone. Although they argued that these echoes are relatively weak, have unusually high aspect angles and have Doppler velocities of 100 m s^{-1}, there has been an uncertainty as to whether they are a common occurrence.

Admittedly, there is an overlap for the altitude ranges where the PMSE, meteor echoes, and close-range E region HAIR echoes appear (mesosphere to lower E region). *Ponomarenko et al.* (2010) have shown that near-range echoes are indeed present, are very frequent and their narrow spectral width stands out. But based on the large degree of uncertainty in associating particular close-range echoes to a particular physical mechanism, this thesis performs a systematic study by carrying out statistical analyses of diurnal and seasonal variations of HF backscatter returns at close-range with respect to occurrence rate, velocity and Doppler shift. The study considers latitudinal variation as it compares results from one radar to the next in a North-to-South chain. The elevation angle information is used to determine the height distribution of SuperDARN close-range echoes. No selected criteria is made for any physical process. With these points in mind, the next chapter presents observations of close-range backscatter from 10 SuperDARN HF radars and the characteristics and properties of these echoes are discussed.

Chapter 6

CLOSE-RANGE HF ECHOES: DATA SELECTION AND ANALYSIS

The design of SuperDARN HF radars has been successful in covering the globe with fields-of-view covering the polar, high- and mid-latitudes (*Greenwald et al.*, 1995). At ranges less than <500 km, E region and lower thermosphere echoes are detected by the SuperDARN HF radars. Many characteristics of such echoes need be studied.

The focus of this thesis is to investigate the origin of the close-range HF echoes detected at the mesosphere and lower thermosphere region of the ionosphere and also identify their properties. This study will also identify and analyze the differences in the characteristics of these echoes at the polar, high-, mid-latitudes. The close-range echoes are different from the normal E region echoes. The meteor echoes and the unusual HAIR are of course present, but are the PMSEs present? To answer the question as well as understand the nature of the short-range HF echoes, it is vital to identify and characterize the echoes based on their diurnal and seasonal variabilities at different latitudes as well as to learn as much as possible about the properties of these echoes, namely the signal-to-noise ratio, Doppler velocity and spectral width. Moreover, it is important for the analysis to use information provided by the elevation angles to determine where in the ionosphere region the short-range HF echoes occur. This means that, in order to estimate the altitude distribution of the close range echoes, we have used interferometry.

The results of the study are presented in this chapter. Specifically, we analyze data obtained from close-range SuperDARN echoes and we concentrate on their variation with respect to time of day for different seasons. Different case studies of the echo occurrence for different radar stations at different latitudes are investigated. The analysis is done by

Radar Station	Geographic Coords		Geomagnetic Coords	
	latitude (^{o})	longitude (^{o})	latitude (^{o})	longitude (^{o})
Rankin Inlet	62.82N	93.11W	72.96N	28.17W
Inuvik	68.42N	133.5W	72.96N	28.17W
Clyde River	70.49N	68.5E	78.8N	18.1E

Table 6.1: Geographic and Geomagnetic coordinates for the PolarDARN which includes the RKN and INV radars.

separating the radars at polar, high and mid-latitudes in order to highlight any latitudinal dependence observed and to understand the dynamics of the echoes from SuperDARN HF radars in the North-to-South chain.

6.1 PolarDARN Radars Location and Geometry With Respect to Other SuperDARN Radars

The analysis begins with the PolarDARN radars at Rankin Inlet and Inuvik. The Rankin Inlet (RKN) radar has been in operation since 2006 and it has been paired with the Inuvik (INV) radar. This pair of radars with overlapping fields-of-view was primarily installed with the aim to cover high magnetic latitudes (showing the beginning of the "poleward expansion" of the SuperDARN network), and to study the dynamics of convection, radio scattering conditions, and field-aligned currents in the polar cap region as well as at the poleward edge of the auroral oval. Table 6.1 gives the coordinates of PolarDARN (including the RKN and INV radars) and Figure 6.1 shows their fields-of-view.

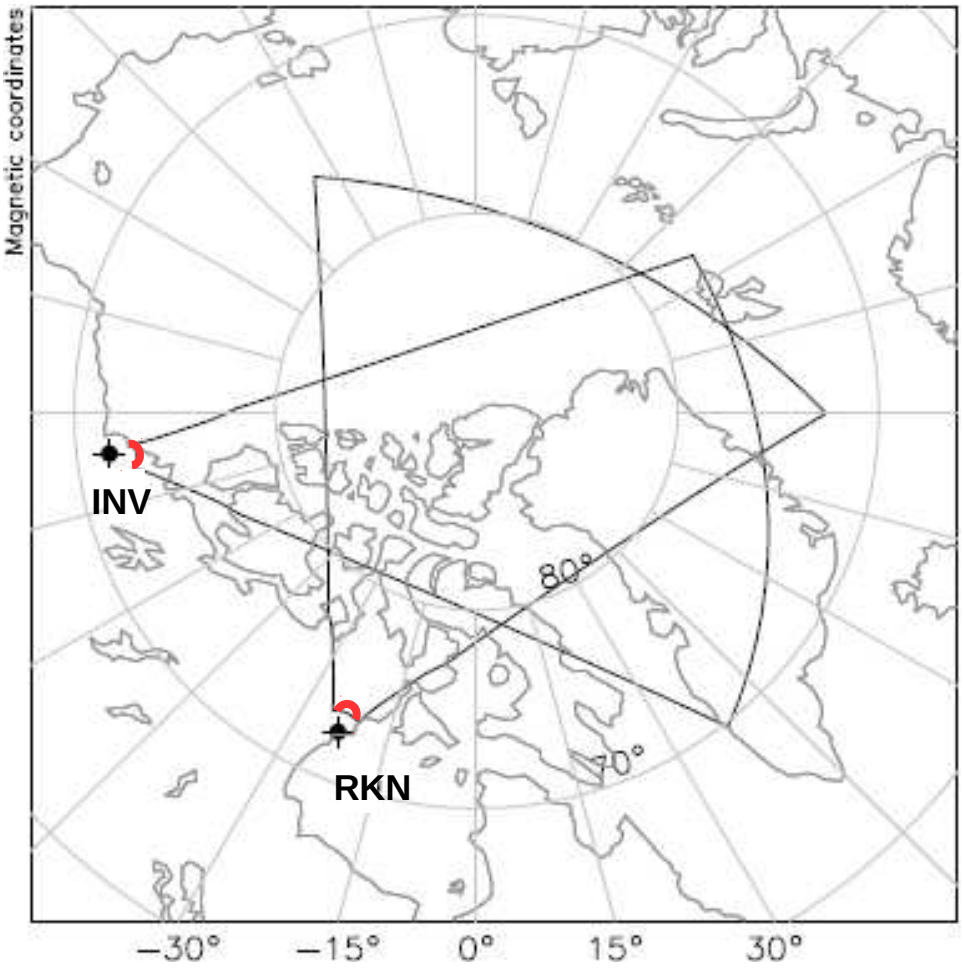

Figure 6.1: Fields-of-view of the Rankin Inlet (RKN) and Inuvik (INV) radars (adapted from *http://vt.superdarn.org/tiki-index.php?page=radarFoV*).

6.2 Observations and Statistical Characteristics of Echo Occurrence

As previously mentioned in Chapter 3, each FOV of the SuperDARN radars consists of 16 beams (usually numbered beam 0, 1, 2, ..., 15) covering a large part of the auroral and polar regions. Each beam samples a total of 75 range gates, with each having a length of 45 km. The first gate start at 180 km from the radar site and the last gate is at 3555 km, giving a total of 3375 km range span.

The region of interest is the first three range gates with emphasis on the first range gate which corresponds to slant range between 180 and 225 km. This is represented by red arcs on the field-of-view of each of the radars shown in Figure 6.1. The analysis begins with accessing the echo occurrence from this range gate for the RKN and INV radars during the period 2007 to 2010. For the analysis, the echo signal-to-noise-ratio (SNR) is $\geq$6 dB (to reduce noise effect).

The average ACFs are processed from the FITACF algorithm so as to estimate key parameters such as the Doppler velocity, the Doppler width, the SNR and the elevation angle for all ranges and on every beam. My analysis began by developing and creating IDL programs, and these were employed and modified to read in FITACF data from any SuperDARN radar for any given day and to create plots of various parameters including the backscatter SNR (dB), line-of-sight velocity (m s^{-1}), spectral width in Doppler units (m s^{-1}) and elevation angle ($^{\circ}$). Also included in these programs are the transformation from one radar beam and range gate to the next and the conversion from universal time (UT) to local time (LT).

6.2.1 Diurnal Variation in Echo Occurrence

Before performing the statistical analysis, individual days were carefully examined. A case study for July 4, 2010 is presented in Figure 6.2. In order to compute the echo occurrence rate for each radar beam and range gate (RG), a value of 1 is assigned when an echo occurs. This is only done when a radar is operational and able to detect echoes. The daily average of

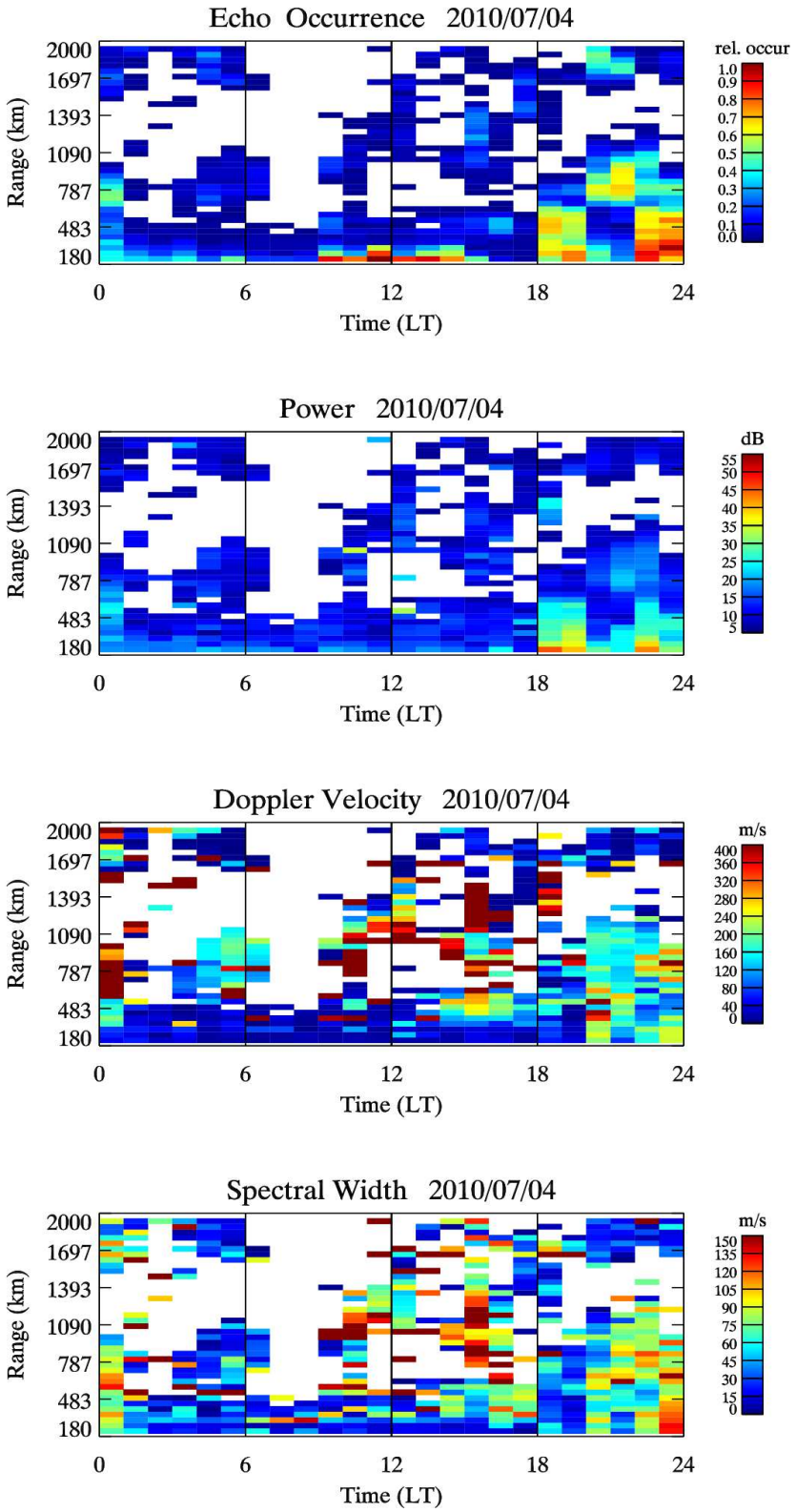

Figure 6.2: Range-Time plots showing echo occurrence, SNR, Doppler velocity and spectral width for the RKN radar on July 4, 2010 at the first range gate and with beam 7.

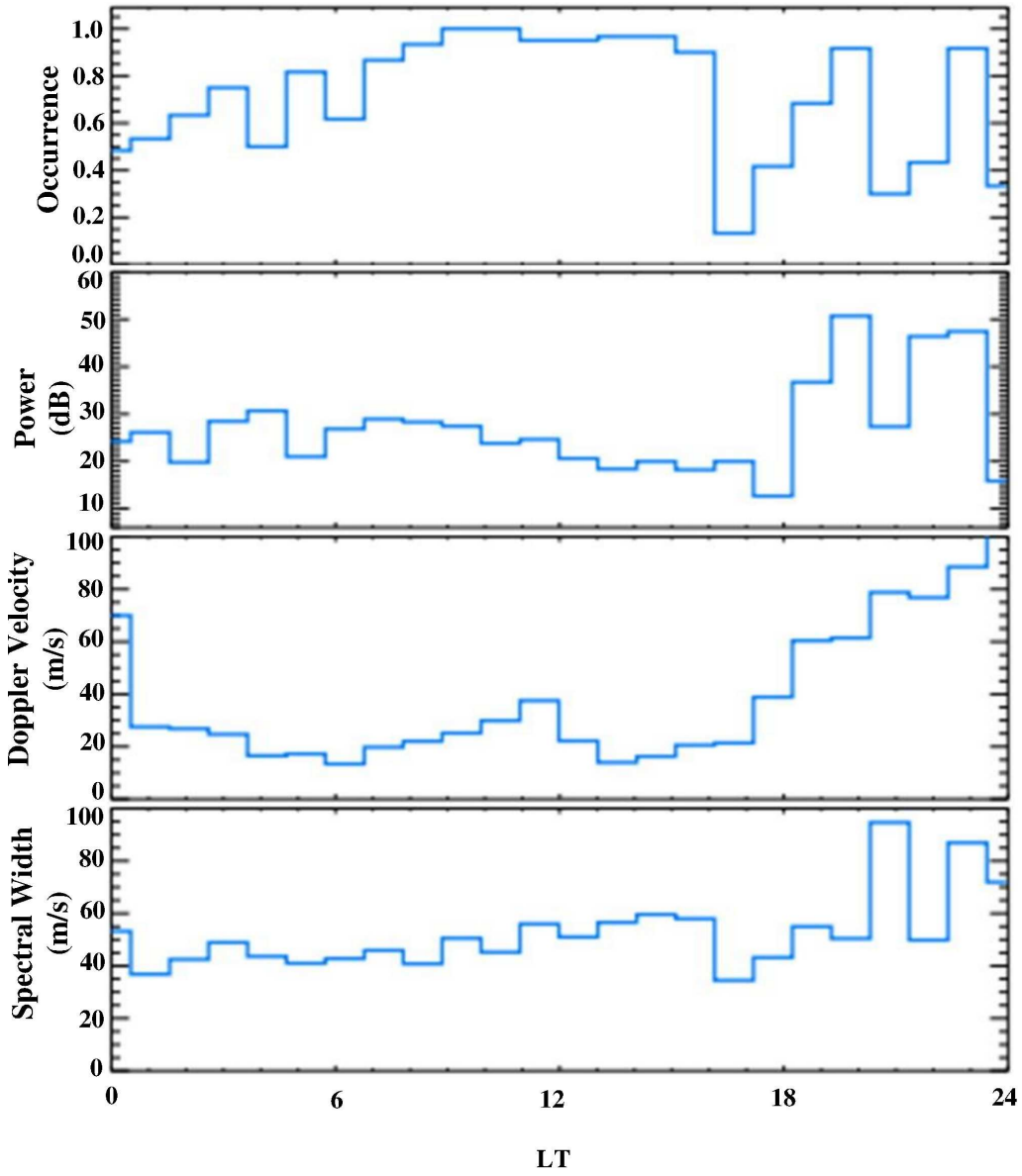

Figure 6.3: Variation of echo properties versus time. Line plots showing echo occurrence, SNR, Doppler velocity and spectral width for RKN radar in July 4, 2010 at the first range gate with beam 7.

echo occurrence was calculated by dividing the measured number of valid ionospheric echoes observed by any given beam and range cell by the maximum possible echo number for the interval of interest. That is, for each radar cell (range-beam cell) within the close range region FOV, the number of echoes detected for any given time was estimated and divided by the maximum number of echoes that could have been detected for that time. The relative number of echoes as a function of range and time is shown in the top plot represented in Figure 6.2 of the RKN radar for each 1-hour period of time. The vertical axis shows the range in kilometers and the horizontal axis shows the local time (LT). The local time for RKN is approximately a 6-hour difference from the Universal Time (UT) for the near field of view of the radar. The UT hours have been shifted in order to account for this difference. The white filling depicts range-time intervals for which no echoes were recorded. During the time interval shown, the radar was operating at 11.5 MHz.

The hourly distribution of the echo occurrence shows enhanced echo occurrence at the near ranges (≤ 500 km). Figure 6.3 (top panel) gives the hourly variations of echo occurrence with time for the first range gate, which corresponds to the closest slant range at 180 km. A maximum is seen between 0700 and 1600 LT and between 2100 LT and midnight. A steep decrease in the frequency of occurrence is seen after 1500 LT with a clear minimum as a result between 1600 and 1700 LT. A clear diurnal variation can thus be seen. During the hours when the long duration maximum is observed, the SNR (the second panel from the top of Figure 6.3) is less than 30 dB until the evening hours, at which point the SNR begins to increase after 1800 LT. The velocity of the enhanced echoes is between 10 and 40 m s^{-1} (third panel from the top) and the spectral width is less than 60 m s^{-1} (fourth panel from the top).

6.2.2 Seasonal Variation in Echo Occurrence

The near-range echo occurrence rate is seen in Figure 6.3 to depend on the time of day. The next step is to investigate if the trend persists through a study of the seasonal variation and time of day. In order to analyze the variation of the echoes with respect to time and season and to compare results from various radars, we averaged monthly echo occurrences for all available data in the year 2010. Figure 6.4 shows the variation of the echoes with

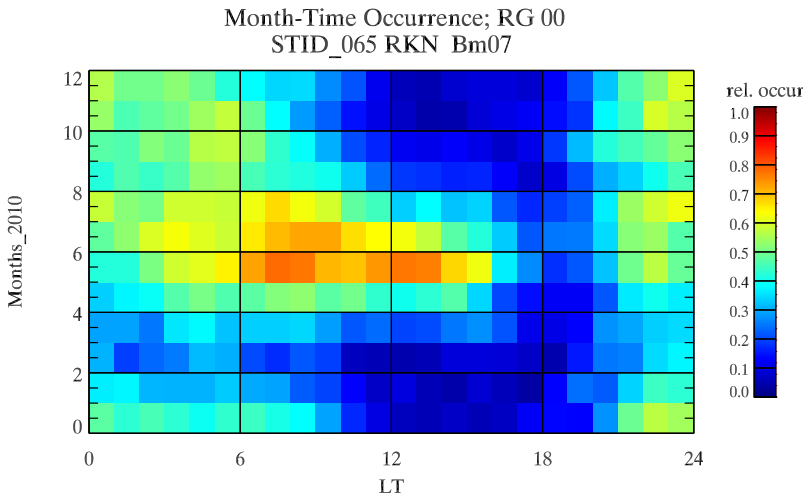

Figure 6.4: Month-Time occurrence rates for RKN in 2010 at the first range gate and with beam 7.

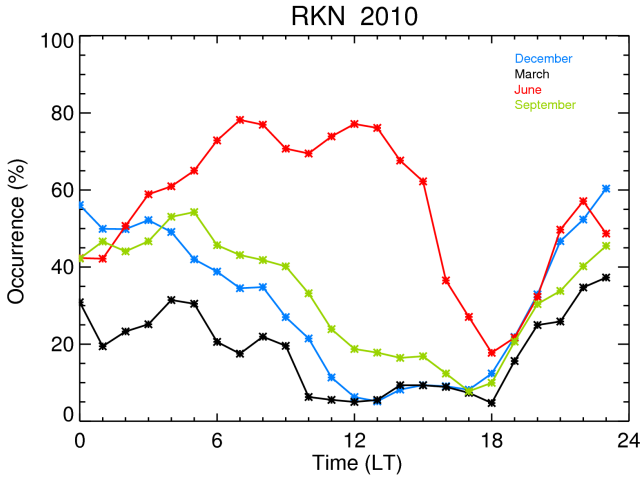

Figure 6.5: Line plots showing month-time occurrence rates in percentage for December, March, June and September of 2010 for RKN at the first range gate and with beam 7.

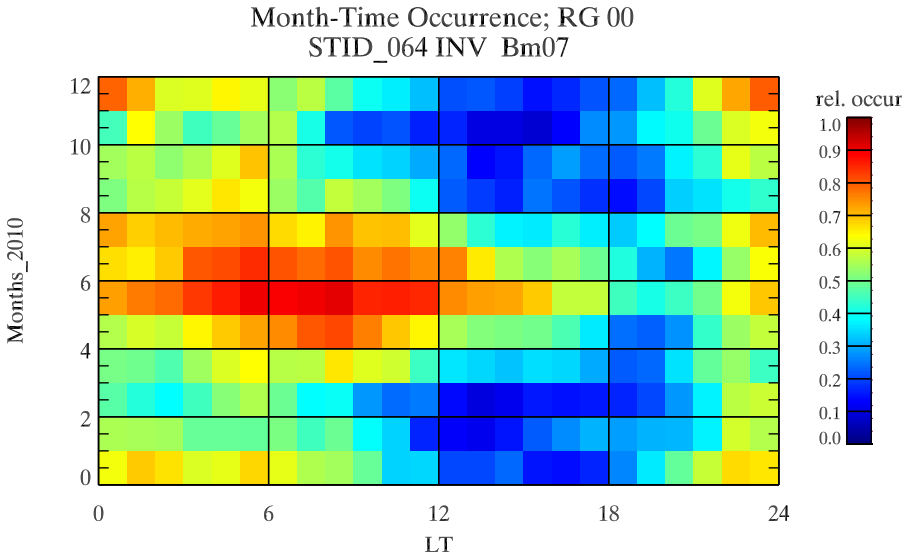

Figure 6.6: Month-Time occurrence rates for INV 2010 at the first range gate and with beam 7.

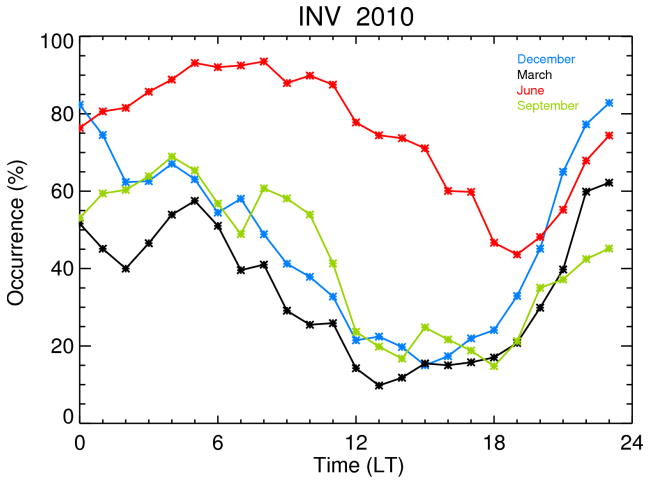

Figure 6.7: Line plots showing month-time occurrence rates in percentage for December, March, June and September of 2010 for INV at the first range gate and with beam 7.

months given on the y-axis and local time (LT) of the day on the x-axis, for the central beam (beam 7) of RKN at the first range gate. These monthly statistics at RKN reveal that the frequency of occurrence of the echoes is high during the daytime hours of the summer months around the period between 0600–1200 LT and that the frequency of echo occurrence begins to decrease until a clear minimum which is observed around 1800 LT for all months. An echo band can also be seen for all months at night beginning at around 2100 LT.

To give a clear sense of the variation of the echo occurrence, the average occurrence over different months for each season was computed. Figure 6.5 presents a line plot for a selected month from the four seasons: winter (December), spring equinox (March), summer (June), fall equinox (September). Significant variations can be seen more clearly for different selected months. An increased occurrence rate beginning near 0600 LT reaching about 78% between 0700-1200 LT can be seen in the month of June. For the month of March, the frequency of occurrence reaches about ∼58% near 0500 LT and 62% at midnight. A clear minimum of echo occurrence around 1800 LT for all months can also be observed with the frequency of occurrence reaching about 22% in June at 1800 LT and 18% in March at 1300 LT, and then increasing after 2000 LT until midnight. The month of September also follows similar diurnal and seasonal patterns. This is in agreement with the plots of Figure 6.4.

Presented in Figures 6.6 and 6.7 are the variations of the echo occurrence for the INV radar in the year 2010. The variations are similar to Figures 6.4 and 6.5 for RKN. In the INV case, diurnal and seasonal variations in occurrence rate can reach a maximum occurrence rate of up to 90% in the summer months. The maximum echo occurrence in June is 91% at about 0800 LT and there is a steady decrease in occurrence rate around 1800 LT where a minimum is observed. The line plot in Figure 6.7 presents another view for the results obtained with Figure 6.6.

To further quantify the occurrence rates for both the RKN and INV radars, the average over 24 hours was computed. Figure 6.8 presents obtained results for RKN (black line with asterisk) and INV (blue line with asterisk) for the 2010 year. Table 6.2 gives the values for the average echo occurrence rates over 24 hours. The first column gives the months, the second and last columns give the RKN and INV observations respectively. It can clearly be seen that the trends of average occurrence rates are similar with a steady increase as well

Month	**RKN**	**INV**
January	0.310	0.475
February	0.240	0.378
March	0.195	0.326
April	0.283	0.458
May	0.403	0.561
June	0.599	0.721
July	0.560	0.633
August	0.497	0.579
September	0.347	0.403
October	0.352	0.401
November	0.324	0.354
December	0.319	0.454

Table 6.2: Average of echo occurrence rate over 24 hours for RKN and INV radars in the 2010 year.

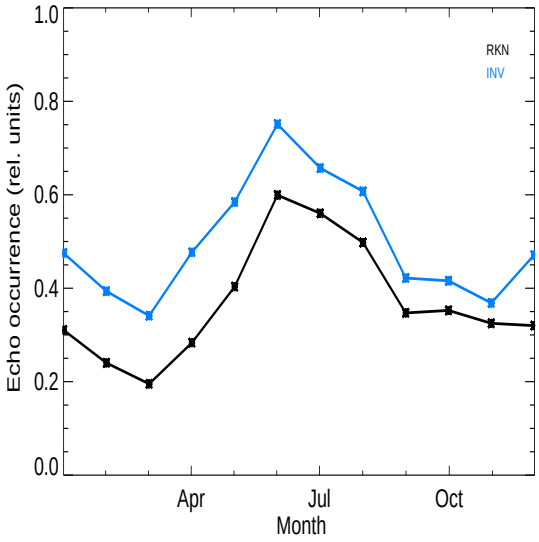

Figure 6.8: Month-Time occurrence rates for RKN and INV 2010 at the first range gate and with beam 7.

as steady decrease. The typical standard deviation was also computed and it gives 0.200 (0.212) for RKN (INV) radar station with a ratio of 0.9 between the two stations. The occurrence rates are highest in the summer months with maximum values of 0.599 in June for RKN and 0.751 in June for INV. The rates are smallest in the same month of March with values of 0.195 and 0.341 for RKN and INV respectively. In the winter months, e.g. in February, the occurrence rate is 0.240 (0.394) for the RKN (INV). Hence, roughly speaking, the difference in echo occurrence rates between summer and winter is a factor of 3.

Data presented in Figure 6.9 show the plots of RKN echo occurrence rates for beam 7 for the first range gate (with color scale shown below) for different years (2007-2010). Each panel contains the year and the months on the vertical axis, and the horizontal axis is the LT. Features earlier discussed are easily recognized. One sees an enhanced echo occurrence during the daytime hours of the summer months. For each year, the pattern of enhanced echo occurrence in Figure 6.9 appears to be like a "tongue" which extends from the early morning hours to the daytime and thereafter decreases after noon. Before progressing into the summer months, the echo occurrence (for example, in February and March) is weak between the dawn and noon hours. During the daytime of the summer months, however, the maxima appear and persist to after noon until about 1400 LT. There are almost no echoes detected around dusk throughout all months and all years.

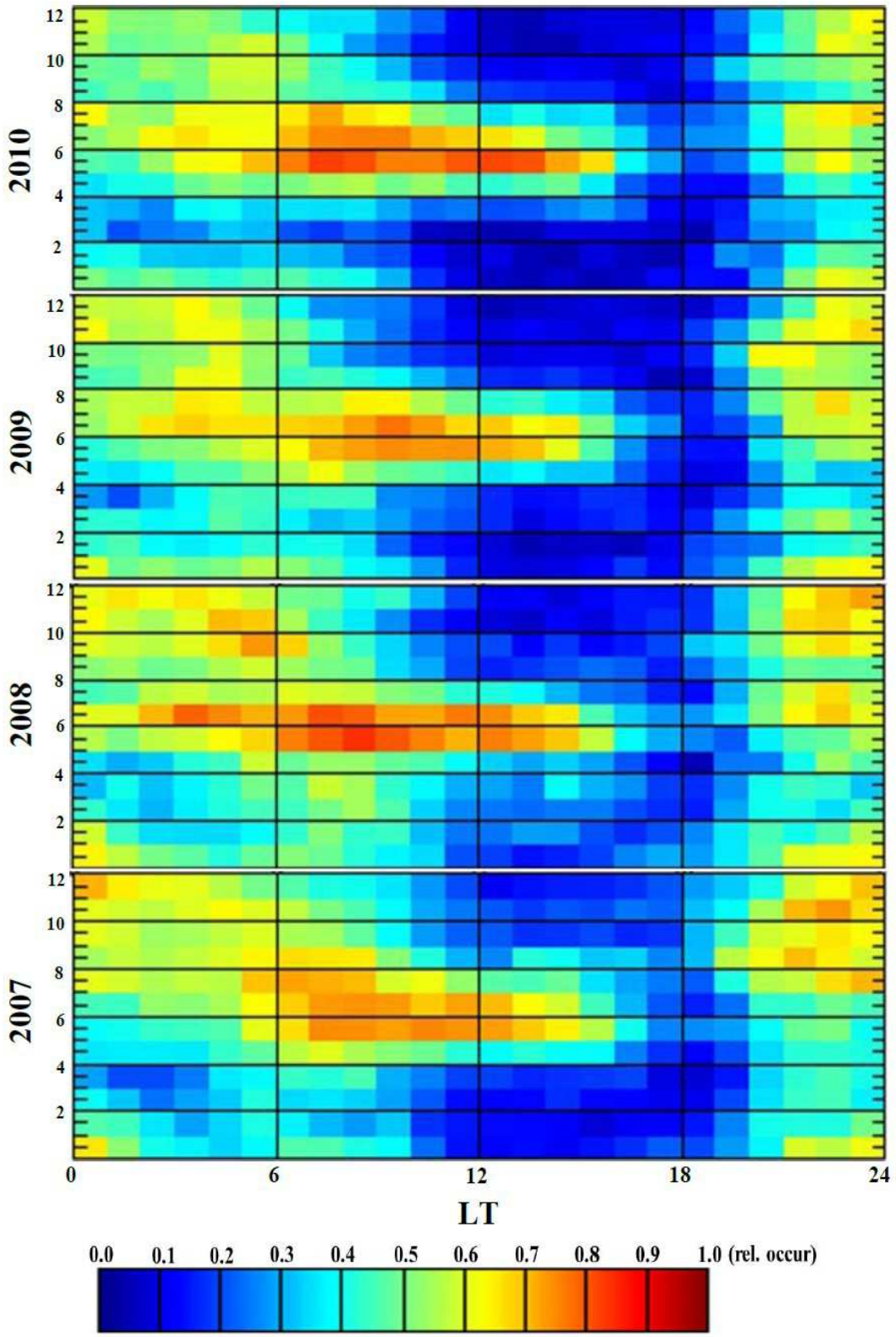

Figure 6.9: Month-Time occurrence rates for RKN at the first range gate and with beam 7. The panels correspond to different years as shown.

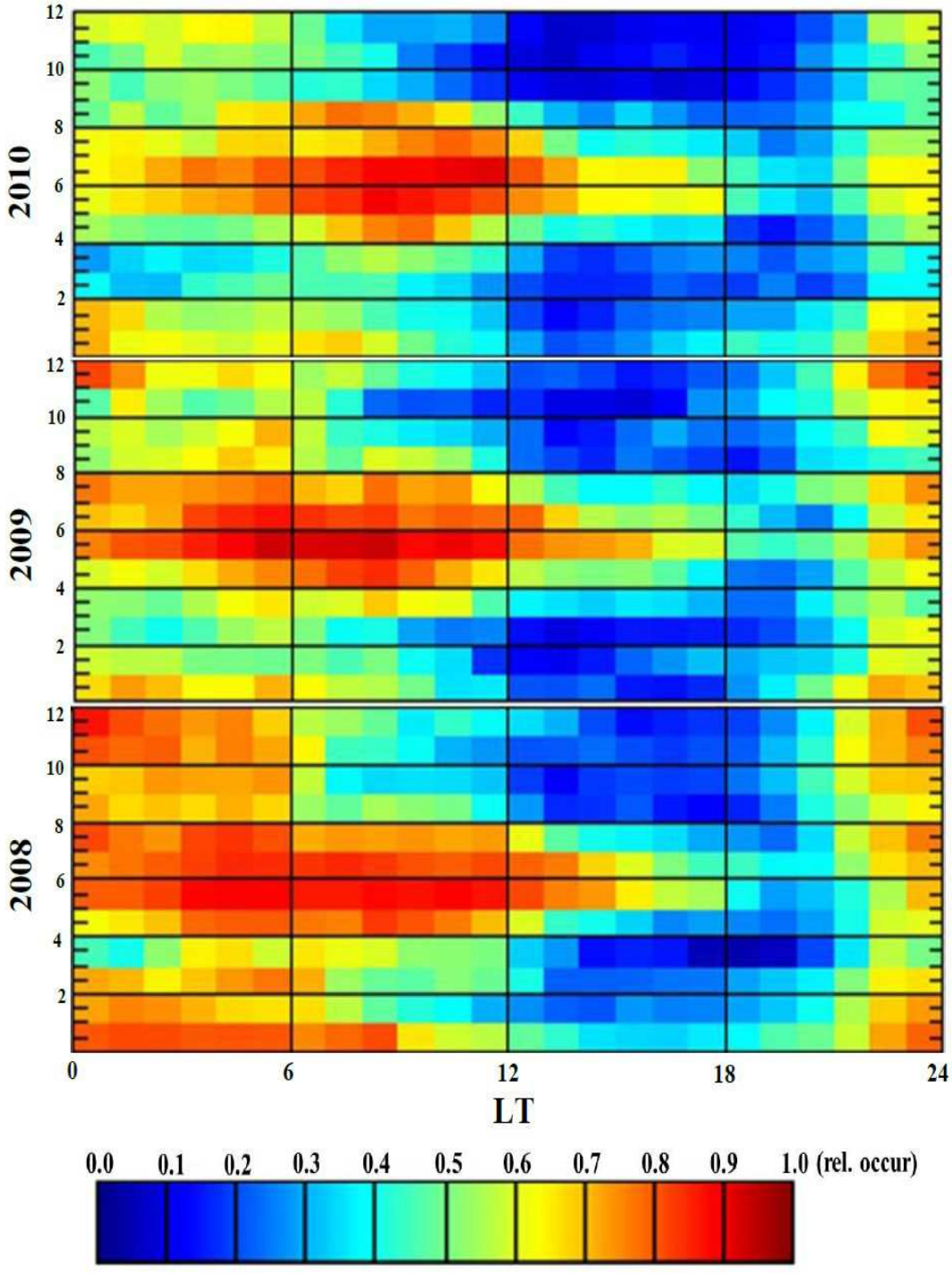

Figure 6.10: Same format as Figure 6.9 but for INV.

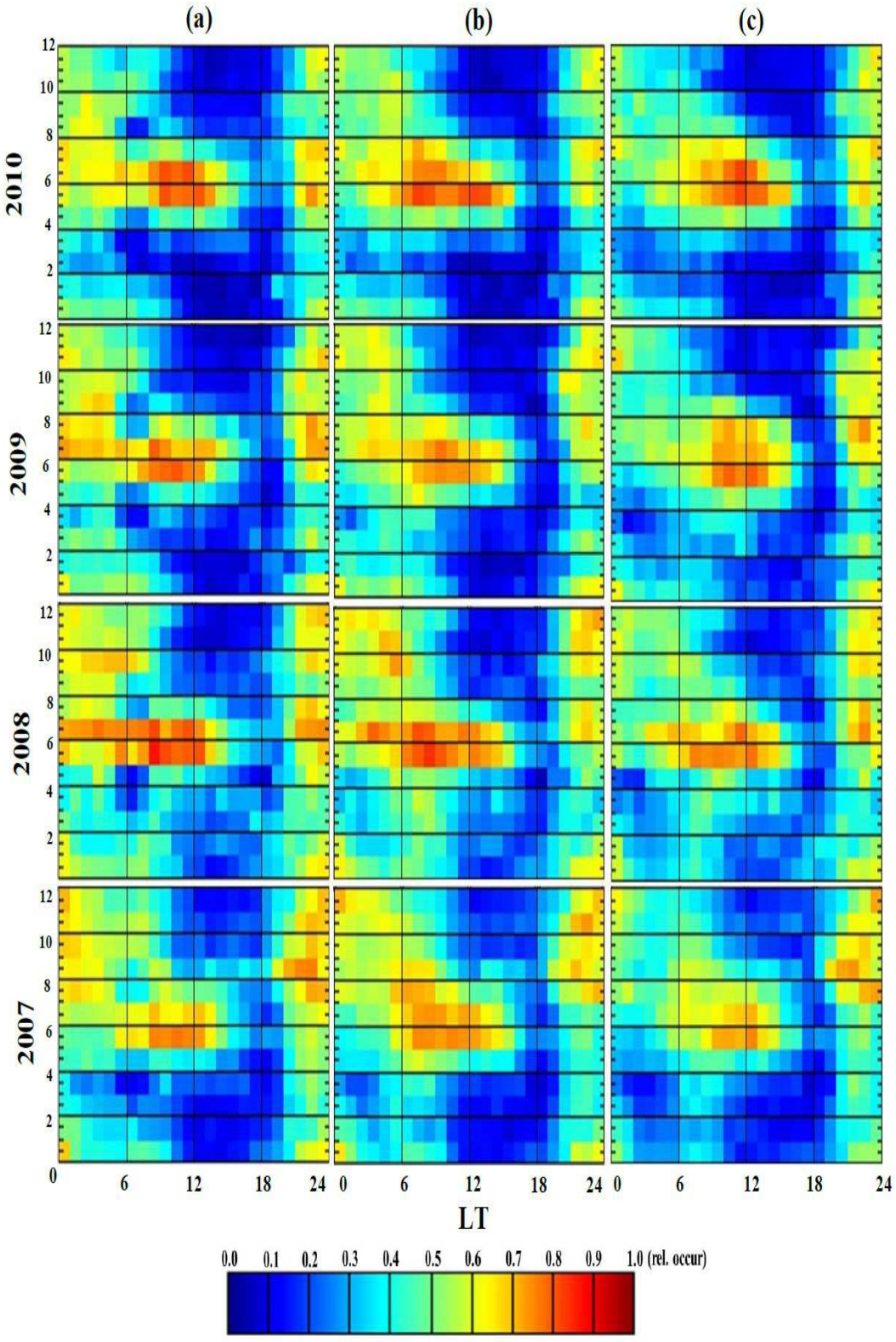

Figure 6.11: Month-Time occurrence rates showing the diurnal and seasonal variations of near-range echoes. (a) western beam 0, (b) central beam 7 and (c) eastern beam 15 for RKN from 2007-2010, (see text for more detail). The color bar is given below each plot.

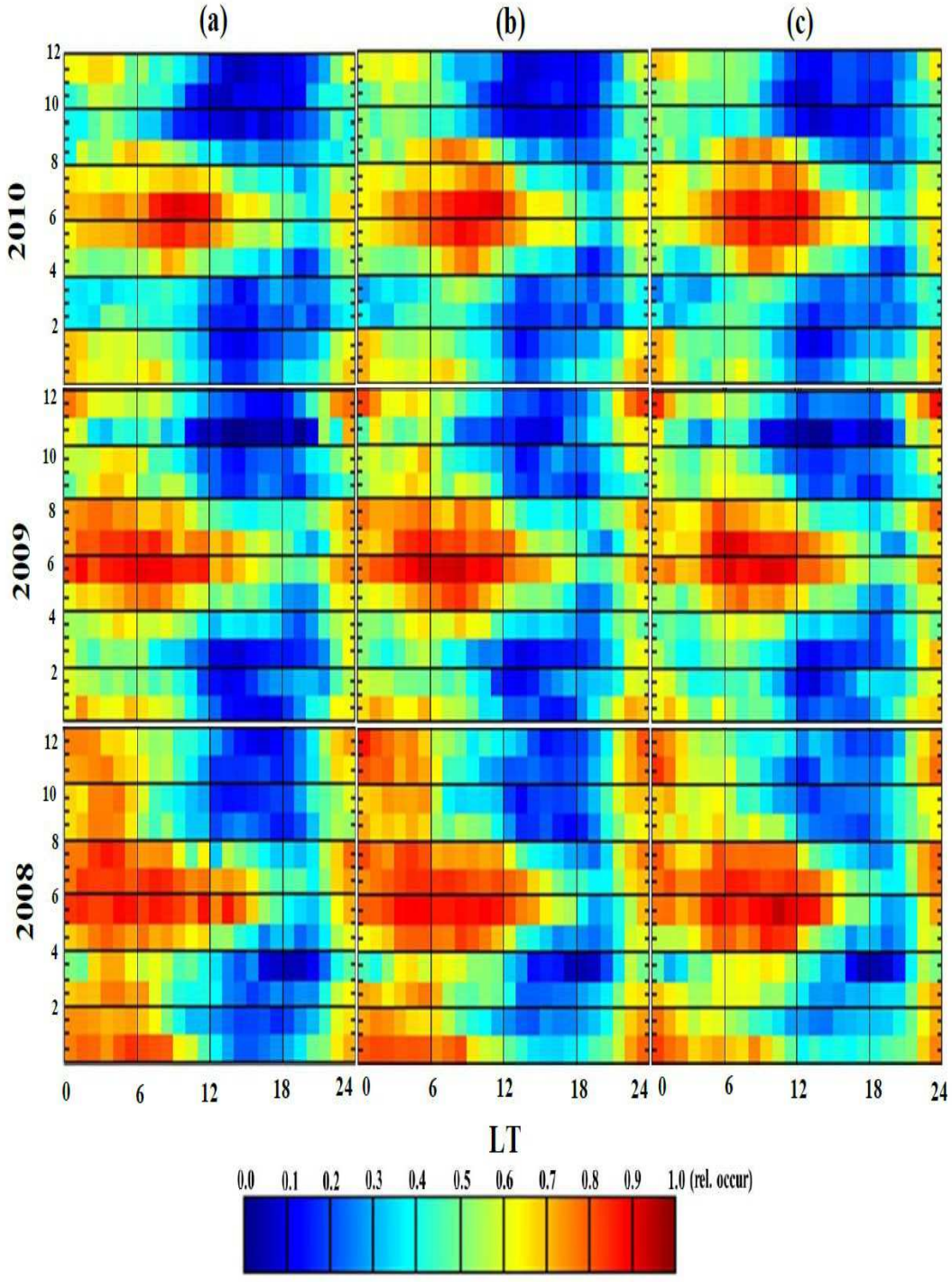

Figure 6.12: Same format as Figure 6.11 but for INV radar station from 2008-2010.

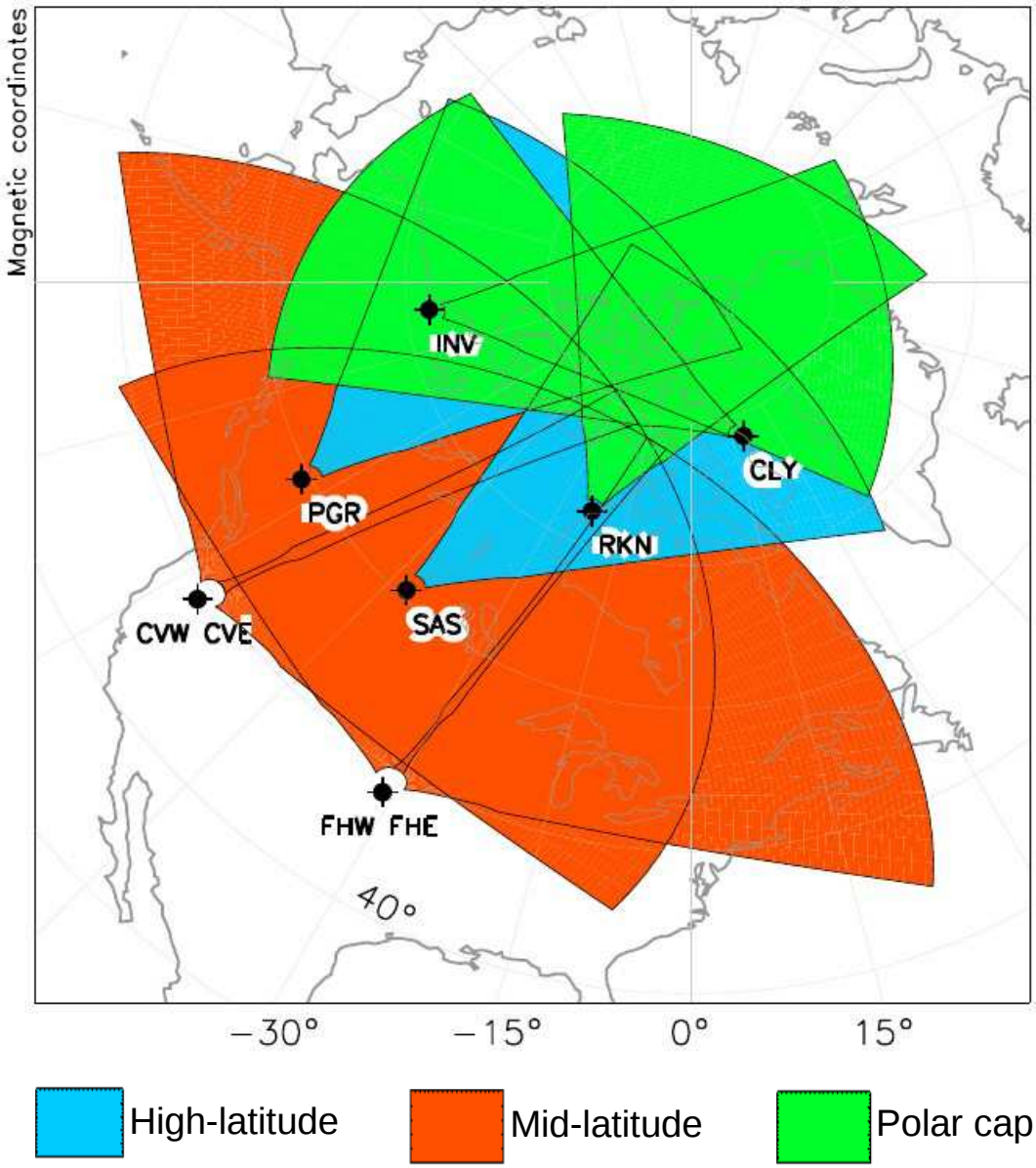

Figure 6.13: Fields-of-view of the eight SuperDARN radars operating in the Northern Hemisphere used during the time of this study. Radar ID corresponding to: Rankin Inlet (RKN), Inuvik (INV), Clyde River (CLY), Saskatoon (SAS), Prince George (PGR), Christmas Valley East (CVE), Christmas Valley West (CVW), Fort Hays East (FHE) and Fort Hays West (FHW) have been used. For each radar, the first range gate. (Produced from *http://vt.superdarn.org/tiki-index.php?page=radarFoV*).

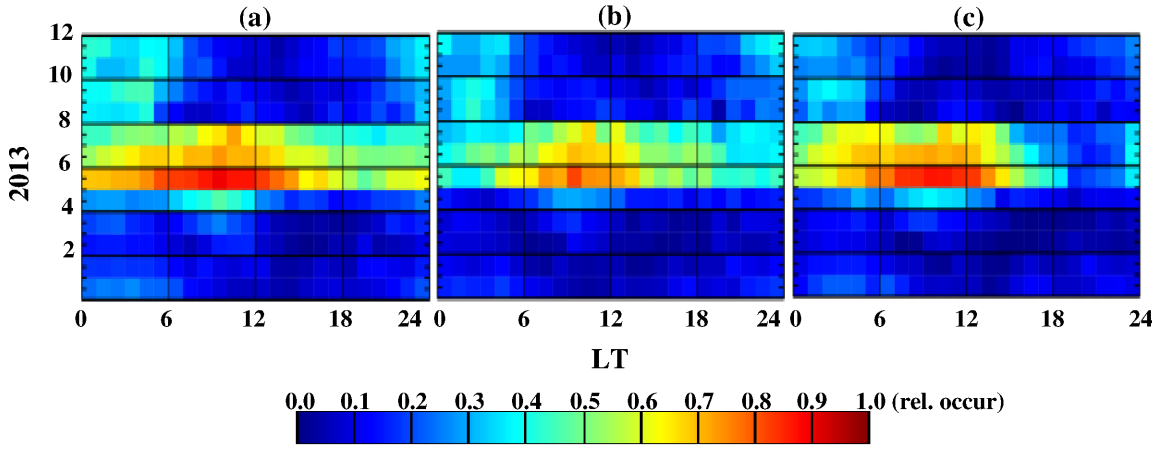

Figure 6.14: Month-Time occurrence rates showing the diurnal and seasonal variations of near-range echoes from (a) western beam 0, (b) central beam 7 and (c) eastern beam 15 for CLY of 2013.

Multiyear results obtained for the INV radar are presented in Figure 6.10. The format is same as Figure 6.9. One can quickly see from the plots that the number of echo occurrence is more for INV radar station than for RKN for all years. This result is consistent with Figure 6.8 where we have shown that the trend followed by both radars are remarkably similar but the observed number of echoes during the daytime hours of the summer months is higher by a factor of about 2 compared to the winter months.

Next, we analyze the variation of the echo occurrence with respect to the different beam directions. For RKN, the statistics of the echo occurrence are shown in Figure 6.11 where a comparison is made between beams 0 (Figure 6.11a), 7 (Figure 6.11b) and 15 (Figure 6.11c) which correspond to the western, central and eastern parts respectively. The year-to-year echo distribution is approximately uniform across all beams, showing similar trends and enhanced echo occurrence rates during the daytime hours of the summer months. Similar results for different beam directions are obtained for INV radar (Figure 6.12).

The Clyde River (CLY) radar holds the record for being the highest SuperDARN latitude radar in the Northern hemisphere (see Table 6.1 for coordinates). The FOV of the CLY radar with respect to other radars are shown in Figure 6.13.

The first range echo occurrence rate for the CLY radar is shown in Figure 6.14 with similar features displayed. Consistent results are seen in the different look directions, that is for beams 0, 7 and 15 (Figures 6.14a-c), showing no directional dependence. These results

Radar Station	Geographic Coords.		Geomagnetic Coords.	
	latitude (^{o})	longitude (^{o})	latitude (^{o})	longitude (^{o})
Saskatoon	52.16N	106.53W	61.34N	45.26W
Prince George	53.98N	122.59W	59.88N	65.67W
Christmas Valley East	43.27N	120.36W	49.50N	58.30W
Christmas Valley West	43.27N	120.36W	49.50N	58.30W
Fort Hays East	38.86N	99.39W	48.90N	32.20W
Fort Hays West	38.86N	99.39W	48.90N	32.20W

Table 6.3: Geographic and Geomagnetic coordinates for the high- and mid-latitude radars.

including those from INV and RKN show that the close-range echoes do not, in general, depend on beam numbers (or look direction).

The RKN and INV radars show similar patterns for the echo occurrence for the different beams used, but there appears to be small changes in the statistical amount of the echo occurrence rates for these radars which are in different longitudes and latitudes. The CLY radar, on the other hand, shows strong seasonal behaviour with high frequency of occurrence observed mostly in the summer months. The next thing to do is therefore to extend the analysis of near-range echoes of radars to the mid-latitudes in order to have a chain of radars which will enable us see if important changes are taken place in these echoes, given that PMSE, meteor echoes, and close-range E region echoes have a latitudinal dependence.

Figures 6.15 and 6.16 show the echo occurrence rate for the SAS and PGR radars respectively. The geographic coordinates and fields-of-view of these radars are given in Table 6.3 and Figure 6.13 respectively. Features similar to those observed for RKN (with maximum frequency of occurrence of 78%) are also seen in these radars although the echoes are more enhanced in the dataset for SAS with rates reaching up to 90% (Figure 6.15), 85% for INV (Figure 6.12), but 70% for PGR (Figure 6.16). During the summer months in the daytime hours, a steep increase at the beginning of May, maxima in June and July and a gradual decrease after mid-August are observed. The statistical pattern of the echo occurrence is

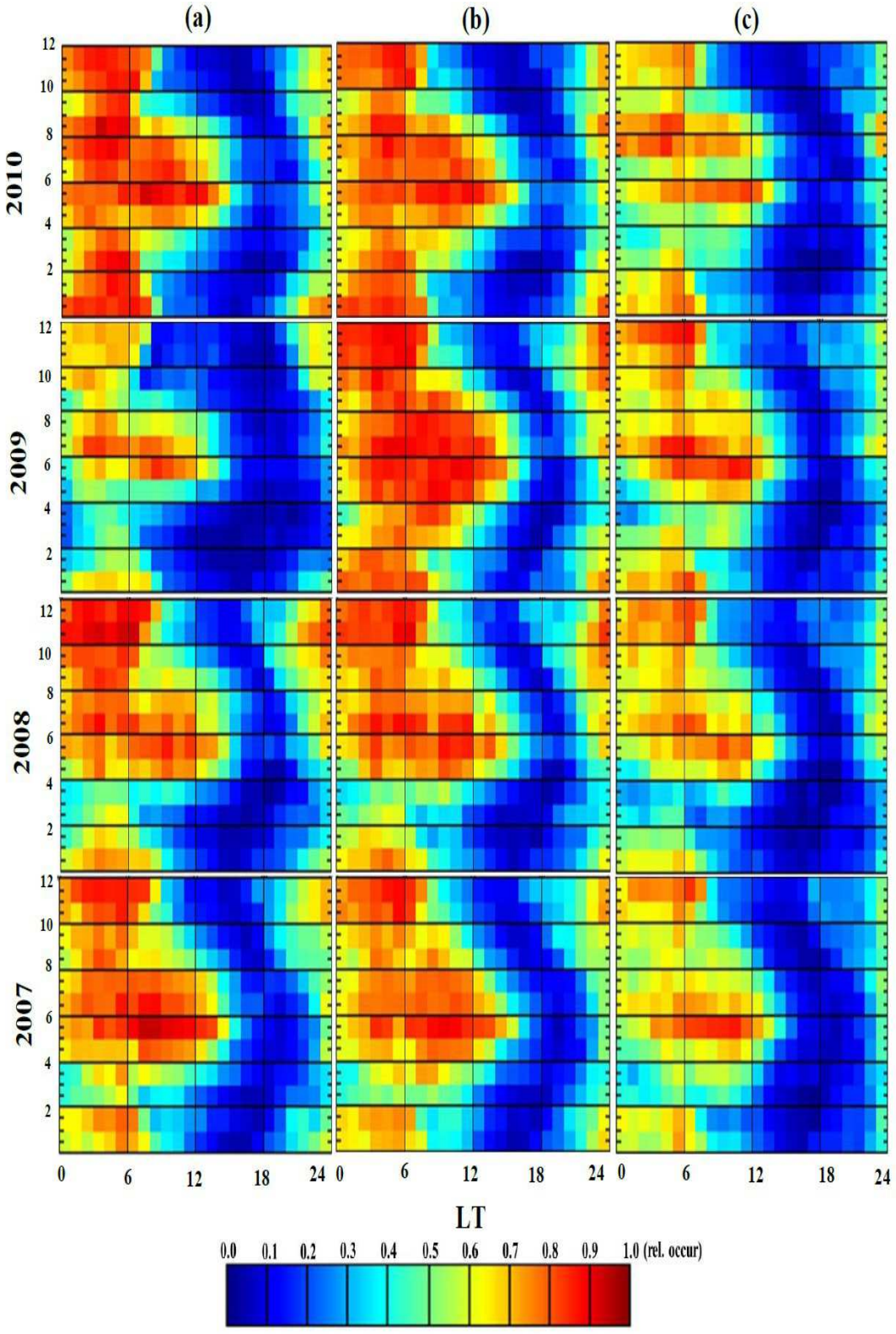

Figure 6.15: Same format as Figure 6.11 but for SAS radar station from 2007-2010.

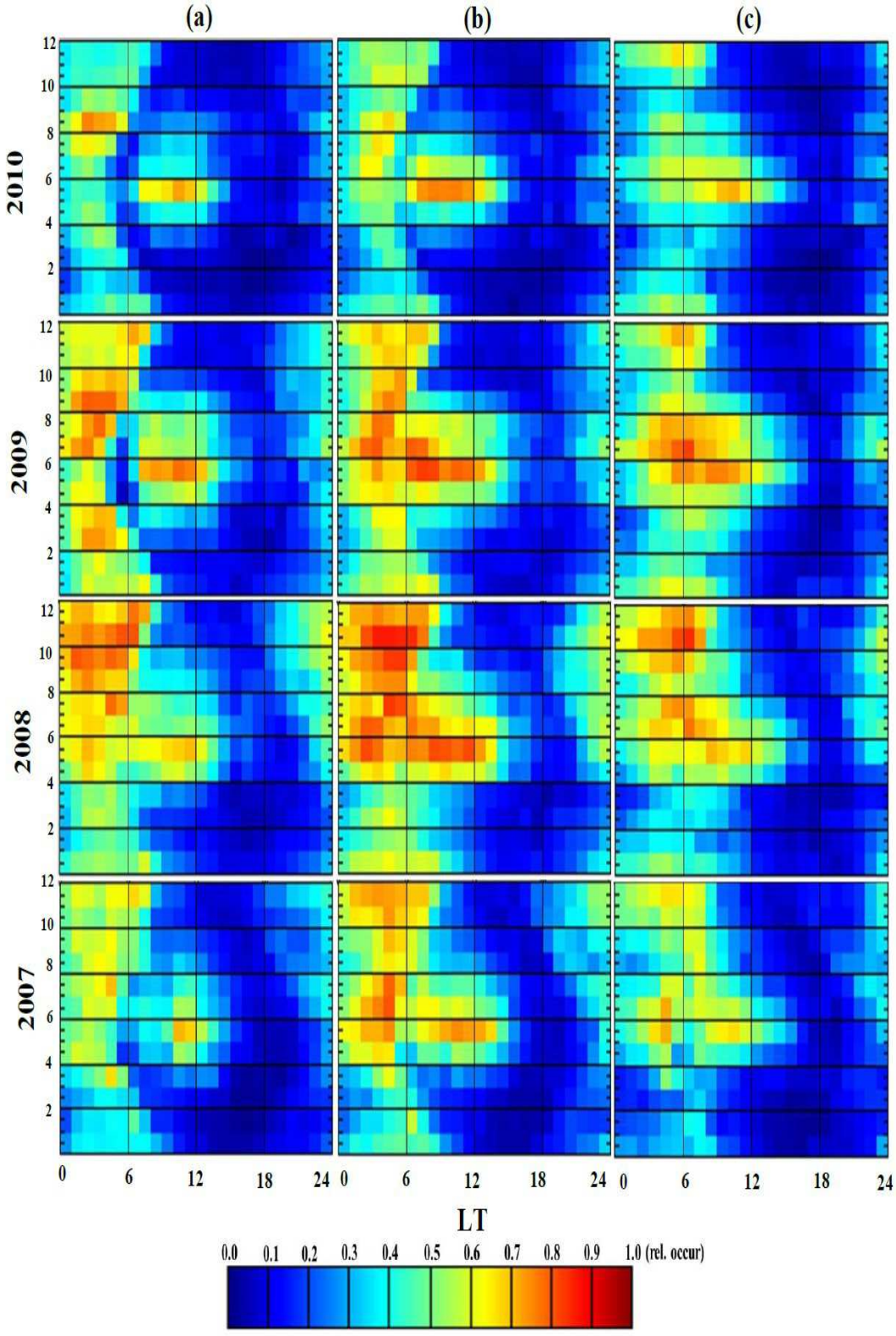

Figure 6.16: Same format as Figure 6.11 but for PGR radar station from 2007-2010.

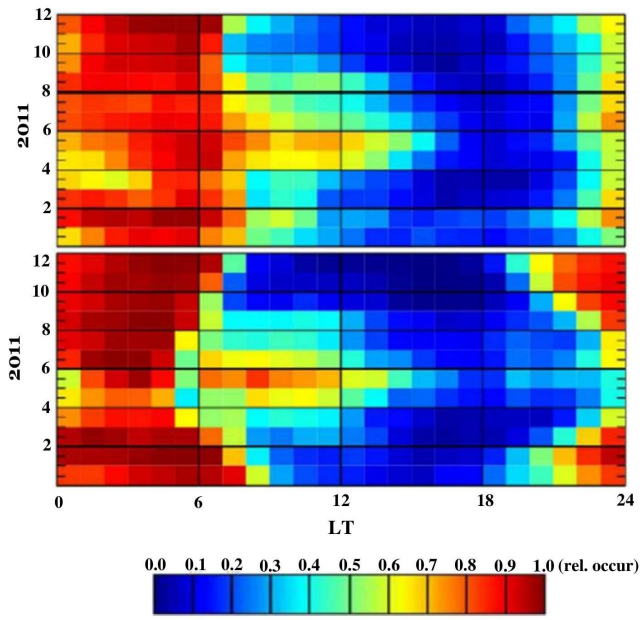

Figure 6.17: Month-Time occurrence rates in beam 7 of CVE (top panel) and CVW (bottom panel) radars from 2011.

similar between the RKN, INV, SAS and PGR radars. The echoes occur for the first range gate (between 180–225 km) on all beams of the radars, indicating that the echoes at this range do not depend on the beam direction.

In order to extend the analysis of the near-range echo occurrence rates to mid-latitudes, four additional SuperDARN radars in the United States, Christmas Valley East (CVE), Christmas Valley West (CVW), Fort Hays East (FHE) and Fort Hays West (FHW) have also been analyzed. The geographic locations of these radars are given in Table 6.3. The FHE and FHW radar sites are closely related as are the CVE and CVW in the mid-latitudes. Figure 6.17 shows diurnal and seasonal variation of close-range echoes for the CVE (top panel) and CVW (bottom panel) radars during the year 2011. The format is same as before with the calender months on the y-axis and the local time on the x-axis. The same features are observed. The trends of echo occurrence in the daytime summer hours of the mid-latitude radars are similar to those observed for the PolarDARN and auroral radars, even though the occurrence rates are different. The maximum occurrence is observed at pre-noon to about 95%, but around noon, the frequency of occurrence decreases to about 70%. We note that a similar diurnal and seasonal variation is observed for other beams.

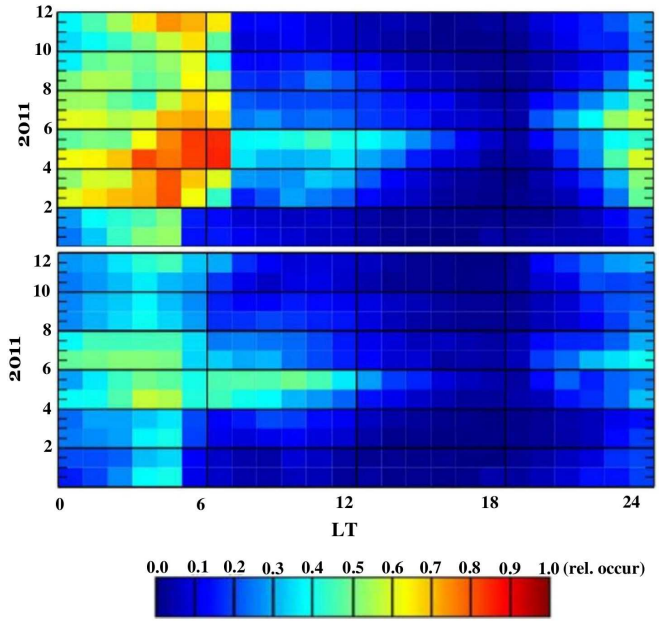

Figure 6.18: Month-Time occurrence rates in beam 7 of FHE (top panel) and FHW (bottom panel) radar station from 2011.

Similar characteristics are displayed by the datasets for FHE and FHW shown in Figure 6.18. The frequency of occurrence of the echoes observed by FHE (top panel) is high to about 80% around the dawn hours (0400–0700 LT) beginning from March, peaks in June and decreases starting in July. For FHW, the echo occurrence near dawn reaches about 50% between May and August and starts decreasing after 0700 LT. These US radars utilize a change in night and day frequencies. This leads to the sharp shift observed for these radars at around 0700 LT, which apparently is due to propagation at different frequencies. A secondary population of echoes can also be observed in the midnight sector, extending into the early morning hours. However, the rate of occurrence is significantly reduced when compared to the other radars. It should be noted that even though the frequency of occurrence observed during the day in the summer months for other radars is higher, the tongue-like feature is still present for FHE and FHW radars.

6.2.3 Characteristics of Short-Range Echoes

The echo SNR, Doppler velocity and spectral width are key parameters to represent the characteristics of the echoes observed by radars. For the case of SuperDARN, such param-

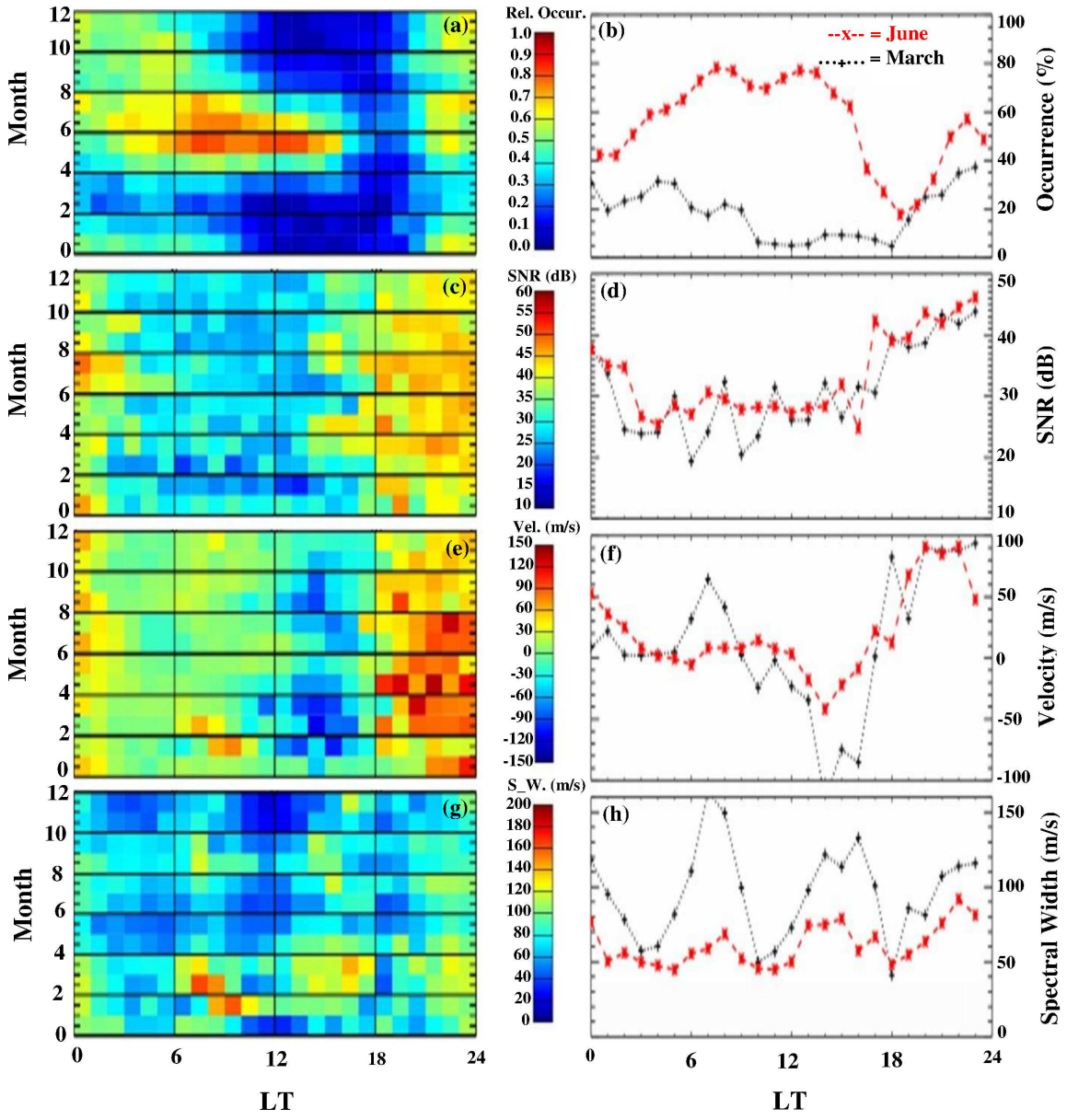

Figure 6.19: Plots for echo occurrence (a), and their corresponding (c) SNR, (e) velocity and (g) spectral width distribution along the RKN beam 7, 2010. (b), (d), (f) and (h) are the line distribution of echo occurrence, SNR, velocity and spectral width respectively for RKN beam 7, for the month of June (red -*-) and March (black ..+..) for 2010.

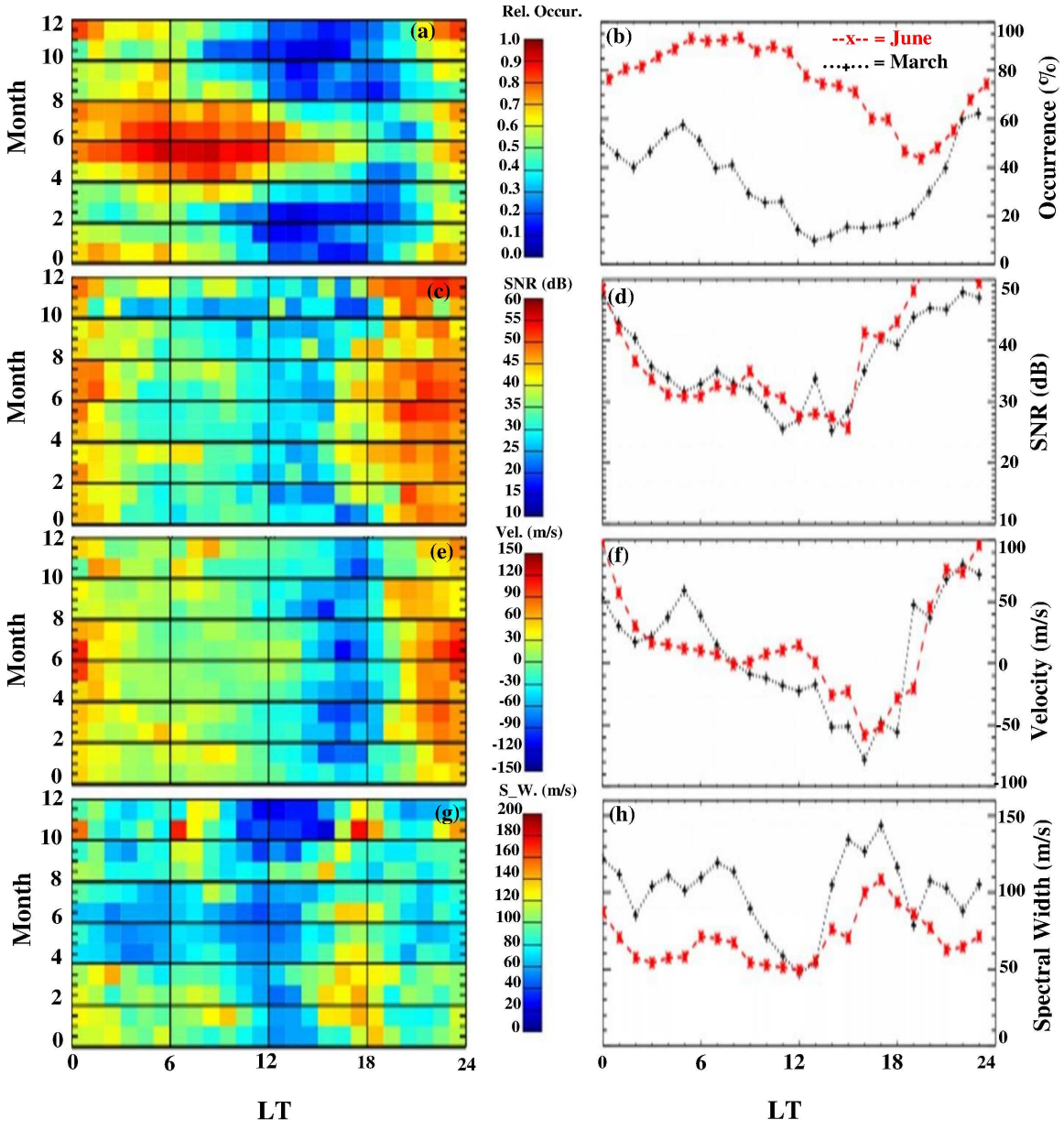

Figure 6.20: Same format as Figure 6.19 but for INV.

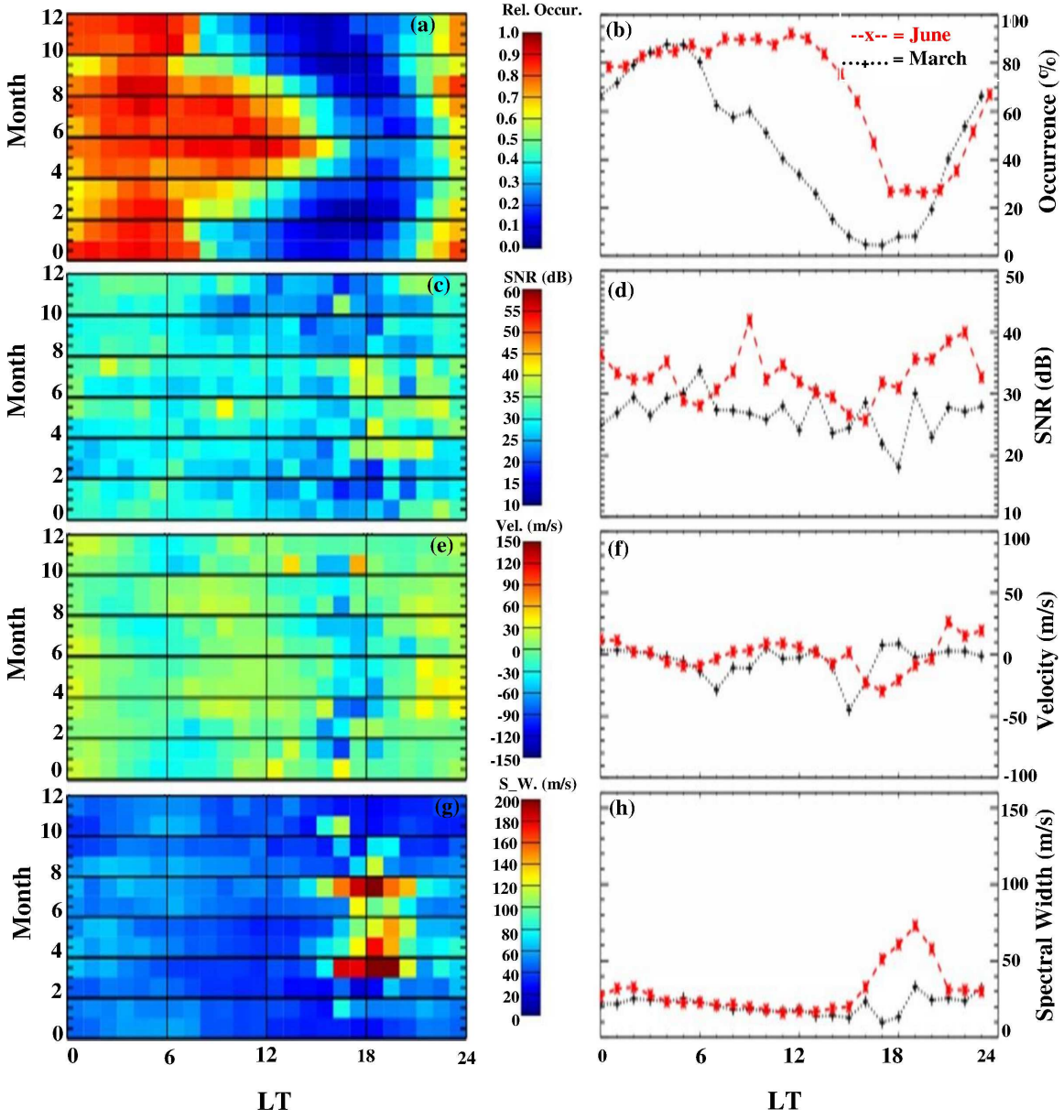

Figure 6.21: Same format as Figure 6.19 but for SAS.

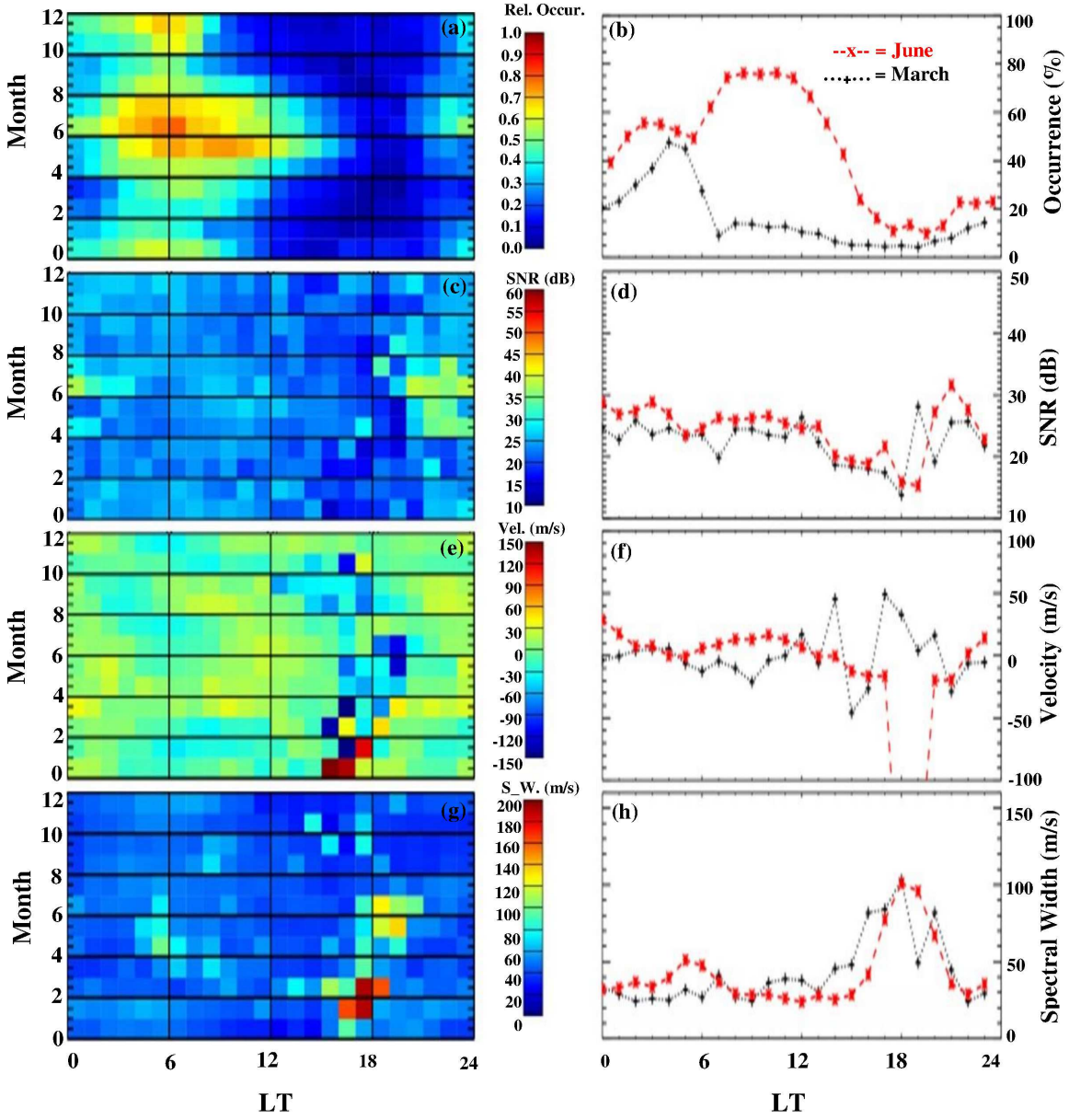

Figure 6.22: Same format as Figure 6.19 but for PGR.

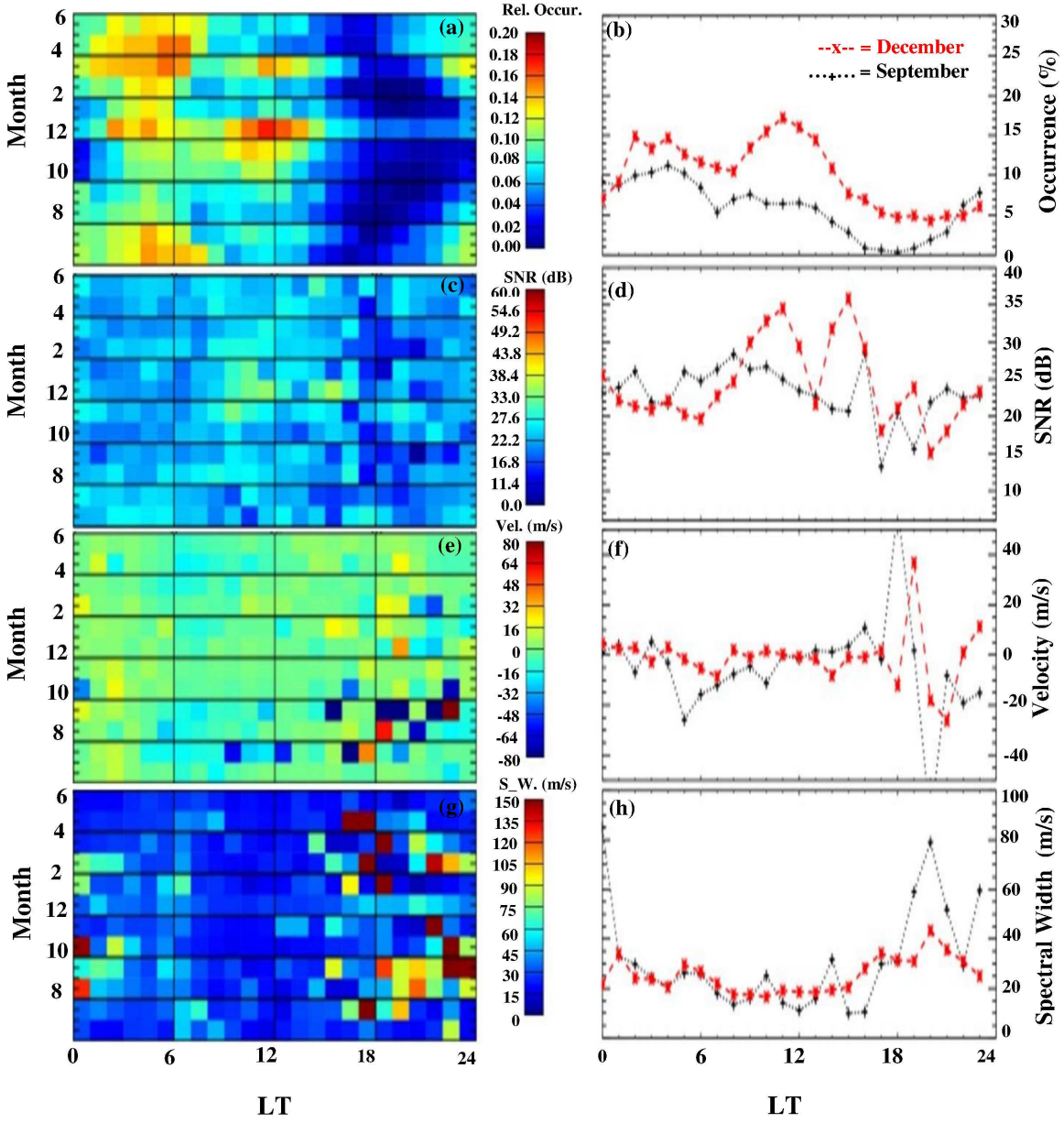

Figure 6.23: Same format as Figure 6.19 but for a Southern radar (TIG). Note that the summer and spring months shonw for the line plots on the right panel is December and September respectively.

eters are estimated from the autocorrelation function of the radar echoes, as described in detail in Chapter 3. This subsection considers the characteristics of the close-range echoes as they relate to the diurnal and seasonal variations. Figures 6.19(a, c, e and g) show 2-D plots for the occurrence rates, SNR ($\geq$ 6 dB), the Doppler velocities and the spectral widths, respectively, for the RKN 2010 beam 7. For each panel of the 2-D plots on the left of Figure 6.19, the months are on the y-axis and the local time on the x-axis. In the summer months when the frequency of echo occurrence is high, the SNR is enhanced from dawn to after noon hours to about 30 dB. There is effectively strong SNR for most months after dusk where the SNR reaches up to 50 dB. These plots are complemented by the line plots on the right of Figure 6.19 to quantitatively assess the echo occurrence characteristics for one of the summer months (June) and one from the spring months (March). The difference in SNR between the summer and the spring months can be clearly seen in Figure 6.19d. The Doppler velocity corresponds to the plasma drift with a line-of-sight component that is either towards (positive velocity) the radar or away (negative velocity) from the radar. The Doppler velocity, when sorted according to season, is about $\pm$40 m s^{-1} during the daytime summer month where the echoes' occurrences are enhanced. After dusk the Doppler speed (Figure 6.19f) begins to increase to about 100 m s^{-1} until midnight. From Figure 6.19h, the distribution of the spectral widths is 50 m s^{-1} around noon where the occurrence rate is at maximum in summer, and in March, it is about 100 m s^{-1}.

It can be seen from Figure 6.20 that the echo properties observed at INV are similar to those of RKN. For the SAS radar shown in Figure 6.21 and PGR in Figure 6.22, the overall SNR in all months and all hours is less than 45 dB. The Doppler velocity in SAS and PGR is less than $\pm$40 m s^{-1}. The difference in Doppler velocity observed between the summer and spring months is not much except for the summer month that has a spike which starts becoming negative to greater than -100 m s^{-1} after 1700 LT in June of the PGR radar (Figure 6.22f) and later increased after 1900 LT. The spectral width of the echo during the daytime hours of the summer month is less than 50 m s^{-1} between 0900 and 1500 LT. A spike in the spectral width that peaks to 75 m s^{-1} for the SAS radar (Figure 6.21h) at 1900 LT and about 102 m s^{-1} for the PGR radar (Figure 6.22h) close to 1800 LT can also be seen. With these few exceptions, the overall Doppler shifts and spectral widths are the same.

The austral seasons for the Tasman International Geospace Environment (TIGER- (TIG)) radars are shown in Figure 6.23. Similar procedures involved in processing data were applied to this radar from the South. The summer season in the Southern Hemisphere begins in December and ends in February. Similar results obtained from the Northern radars can be seen in the South with three populations of echo occurrence (Figure 6.23a). However, the overall rate of occurrence for this Southern radar is significantly less than those from the Northern hemisphere radars. For the summer season, the daytime population increases in December, peaks in January at 1100 LT to about 18% and decreases until February. The spring season has a maximum near 0600 LT (dawn population). All months see a minimum near 1700 LT which is a common feature of the Northern radars. Figure 6.23b gives line plots showing the diurnal variations of TIG close-range echoes for December and September. This stated, we do expect different thresholds for different radars, so that the similarity of the patterns is more than the differences in numbers themselves.

Figures 6.23(c-h) give the characteristics of the echo occurrence for TIG radar with respect to SNR, Doppler shift and spectral widths. The signal-to-noise-ratio (Figure 6.23c) from month to month does not show any significant pattern (and is clearly shown in Figure 6.23d). The overall values does not exceed 35 dB. The same can be said for the velocity during peak echo occurrence. The Doppler shift in general does not exceed ± 50 m s^{-1}, except in July to October with values of more than ± 50 m s^{-1}. The spectral width also displays similar behavior with that of other properties with values less than 50 m s^{-1} except after 1600 LT where values above 50 m s^{-1} is observed. Overall, there is no dependence of the echo properties with respect to time of day and season.

6.2.4 Spatial Pattern of Echo Occurrence Rates

The spatial occurrence pattern (i.e. slant range information) of the echo occurrence is investigated in the present subsection. Plots of range-versus-beam echo occurrence are made and examined in order to determine where, within the field-of-view, the close-range echoes are detected across beams and if any variability is observed from beam to beam for the SuperDARN close-range HF echoes.

Figure 6.24 presents the slant range versus beam echo occurrence rates for the PolarDARN

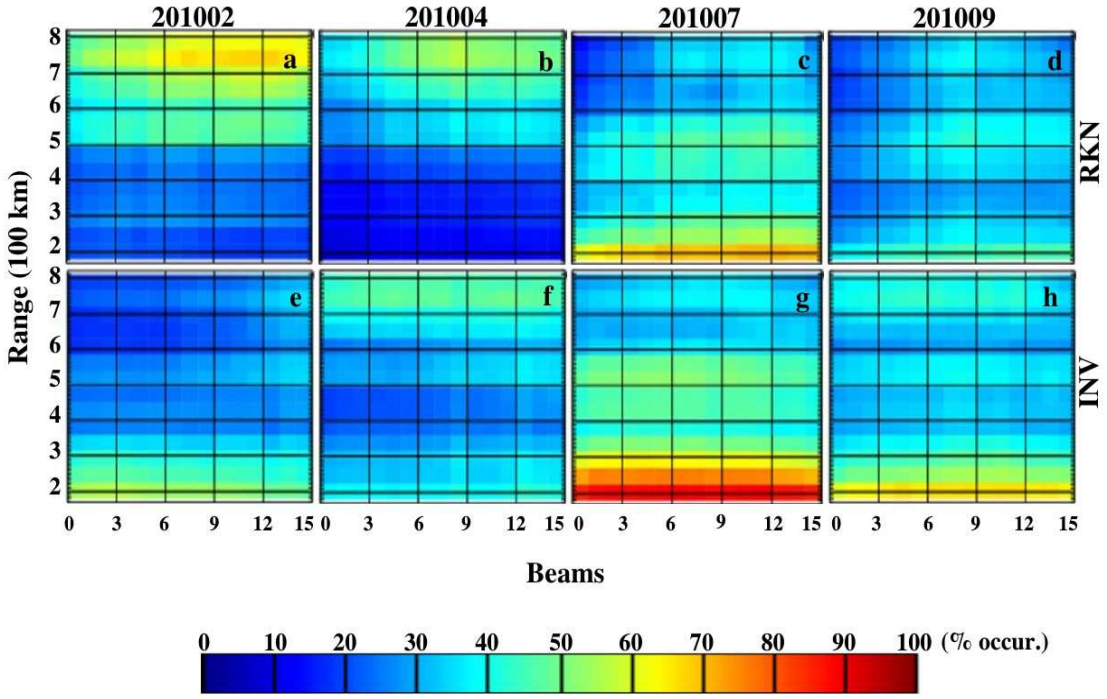

Figure 6.24: Spatial echo occurrence patterns across 16 beams for the RKN (top row) and INV (bottom) radars around noon (1000-1400 LT) with selected months from each season February(a, e); April (b, f); July (c , g) and September (d, h) in 2010. The echo occurrence patterns presented are for the datasets with ranges ≤800 km. The color scale gives the percentage frequency of echo occurrence.

radars (RKN and INV) around the noon sector (1000-1500 LT) for periods of 201002, 201004, 201007 and 201009 (i.e. February, April, July and September respectively of the year 2010). Each cell's color represents HF backscatter as the percentage relative to the maximum value within the entire view. The top and bottom panels of Figure 6.24 represent the RKN and INV radars respectively. The vertical axis for each panel gives the range in kilometers, and the horizontal axis gives the beam number. The spatial occurrence plots are for data with ranges ≤800 km. Figure 6.24c shows a pronounced echo band that stretches across almost all the beams for RKN in the ranges approximately <250 km and a reduced population between 450 and 600 km ranges. However, for Figures 6.24a and 6.24b of the RKN radar, the enhanced echo band is absent for close ranges but a second population is observed at farther ranges (beyond 500 km). For the month of September (Figure 6.24d), close range echoes are observed but at a much smaller rate of occurrence than during summer. This occurrence distribution pattern is similar to that of INV (Figure 6.24g) but is more enhanced compared

to RKN. Figures 6.24e and Figure 6.24f show similar results obtained for the RKN radar for 201002 and 201004. The month of September also shows a similar result (Figure 6.24h). Roughly speaking therefore, one can see that the distribution of echo occurrence across all beams is very similar for both radars. The distinct features corresponds to enhanced echo band in the nearest ranges (less than 300 km) for July. There is a second band near 500 km in summer. Overall, the figure shows that close-range echoes are not a function of beam number. But they also show a motion with respect to range of echoes with season.

6.2.5 Summary of Echo Occurrence and Properties of Backscatter

The analysis of close-range SuperDARN HF echoes have shown that the echoes vary diurnally and seasonally. Based on their characteristics, three distinct populations have been observed. The evening population observed after 1800 LT is visible and very obvious only in the high latitude radars, with exception of CVW. This population of echoes tends to have higher Doppler shifts in the higher latitudes.

The dawn population shows up very clearly but not always as it varies from month to month. This morning population is very pronounced for all years in the SAS and CVE and CVW, but mostly in 2008, 2009 for PGR, 2008 for INV and is reduced in 2008 for RKN. For 2010 of TIG, the variability is observed but becomes weak in March.

The late morning/midday population is only seen during the summer months. They are either long or short lived. When observed at earlier times, this population overlaps with the dawn population. It has Doppler velocities of ± 50 m s^{-1} with nothing remarkable in the Doppler shifts and even the SNR. These echoes are ordinary looking echoes and there is no significant difference observed from beam to beam. While the pre-midnight population of echoes do not depend on beam number, they are auroral bound and their spectral properties are different from the other radars.

The data used in this thesis are based on the selection criteria of signal-noise-ratio greater than 6 dB. By definition, signal-to-noise-ratio involves the ionospheric signal power and the background noise power. The noise level changes significantly during the day and also from one radar to the next. Therefore, depending on the level of the noise, echoes with the same absolute power level are sometimes selected and sometimes rejected. The study by

Ponomarenko et al. (2015) has shown that while it is good to compare the frequencies of occurrence, we have to be careful because the noise contribution to the occurrence/signal-to-noise-ratio varies. The occurrence patterns change somewhat modestly but not significantly. For this thesis therefore, we should only focus on the relative trend or pattern of occurrence across all latitudes as the echo occurrence is subject to not only the signal, but also to the noise. That being stated, it is important to note that although the analyses of the CVE, CVW, FHE and FHW radars show similar trend/pattern with respect to their diurnal and seasonal variations, each radar has its own morphology. Even though these mid-latitudes radars are built in the same way and around the same years, they are shown to have different threshold power levels. This means that while trends can be compared from one radar to the next, caution should be exercised when considering the actual occurrence rates and power levels.

6.3 Elevation Angle and its Connection to the Scattering Altitude

The properties of close-range echoes have been identified but what altitude are they originating from? This information can be obtained from the elevation angles. SuperDARN receives scatter from ionospheric irregularities in the E and F region. SuperDARN employs an oblique sounding technique involving straight line propagation of radio waves from the radar to the scattering region. The oblique incidence allows echoes to be detected, possibly even at mesospheric altitudes, that is, in the first range gate of SuperDARN radars (*Ogawa et al.*, 1999).

In order to accurately estimate the location (altitude) information at which backscatter emanates, the measurement of elevation angles and the slant range to the backscatter volume must be used. These data can be obtained from most of SuperDARN radars. As previously mentioned in Chapter 3, the elevation angle is obtained through interferometry (*Milan et al.*, 1997a).

6.3.1 Virtual Height Determination of Close-Range Echoes

The combined knowledge of range and elevation angle for a flat Earth and a planar ionosphere offers a simple way for the estimation of a scattering point altitude less than a few hundreds of km away from the radar. Assume a triangle having 3 sides: (1) distance from the center of the Earth to the radar location is side R_E; (2) distance from the center of the Earth to the virtual scatter point is side $R_E + h$; and (3) side r is the slant range of virtual propagation. Therefore, the virtual height, h, can be written as (*Milan et al.*, 2001):

$$h = \sqrt{r^2 + R_E^2 + 2rR_E \sin\varepsilon} - R_E \tag{6.1}$$

Equation (6.1) shows how a knowledge of the range and elevation angle (while assuming straight-line propagation of an HF signal) can be used to determine the location of backscatter returns. The term "virtual height" used for the height obtained from the interferometer measurements of elevation angles means that the results are not direct height measurements since straight line propagation is assumed in the above analysis, with no way of accurately knowing the level of refraction occurring in the ionosphere.

To further understand the nature of the close-range echoes, we analyze the diurnal and seasonal variations of the virtual height. Unfortunately, the interferometry technique that enables the measurement of elevation angle is not employed in all the SuperDARN radars. This thesis therefore only considers radars used in this study that are using interferometer arrays. The results are presented for INV in the 2-D distribution plot (Figure 6.25) for a 24-hour period in the first range gate of beam 7. The top panel shows the frequency of echo occurrence each month. The middle and bottom panels give the elevation angle and virtual height respectively. The local time is on the x-axis and the y-axis gives the months. The virtual height distribution is estimated using Equation (6.1). The enhanced midday summer population is easily seen. The echo occurrence begin to increase in May, peaks to about 95% in June and decreases again. During this period where the frequency of occurrence of the echoes is high, the elevation angle (or the virtual height) decreases to a smaller value. Similar results are obtained for different look directions (beams 0 to 15). These features are seen in more precise terms for the month of June as represented in the line plot shown in

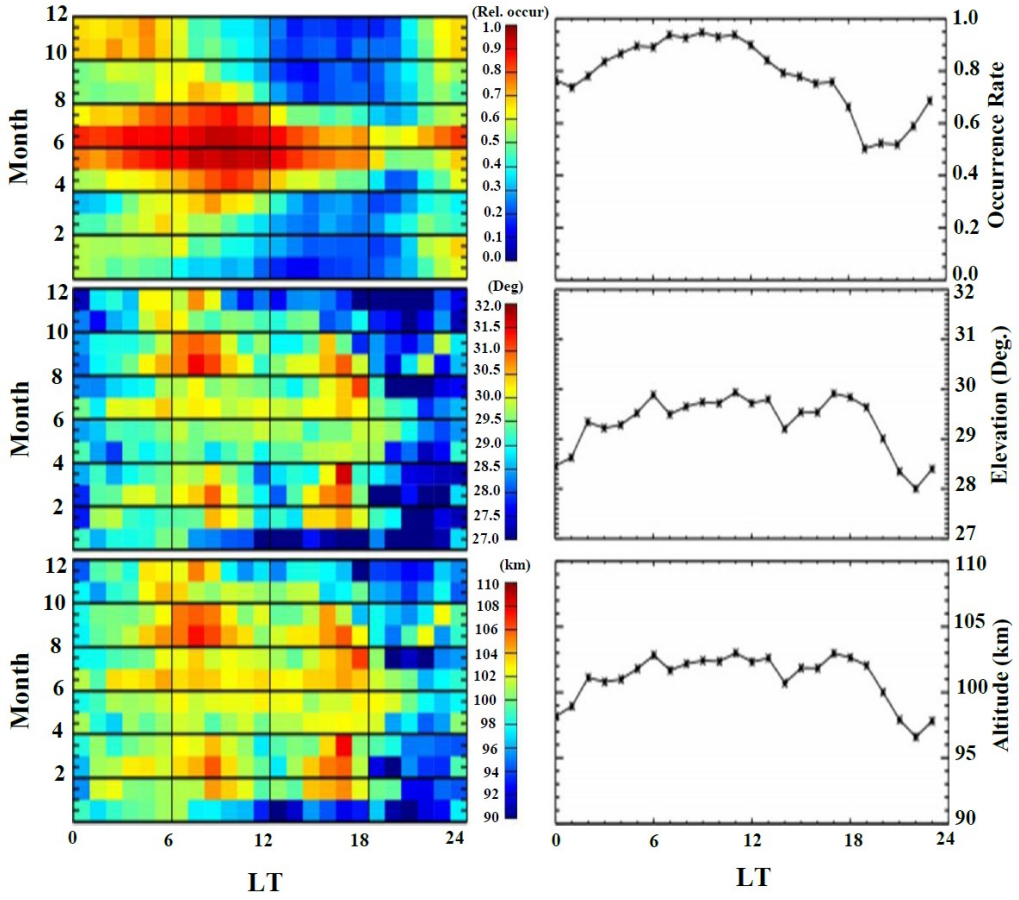

Figure 6.25: Two-dimensional month-time distribution (left panel) of echo occurrence (top), elevation angle (middle), and virtual height (bottom) at INV during 2012. The right panel is similar to the left panel from top to bottom but for the month of June only. The vertical axis gives the months and the horizontal axis the local time.

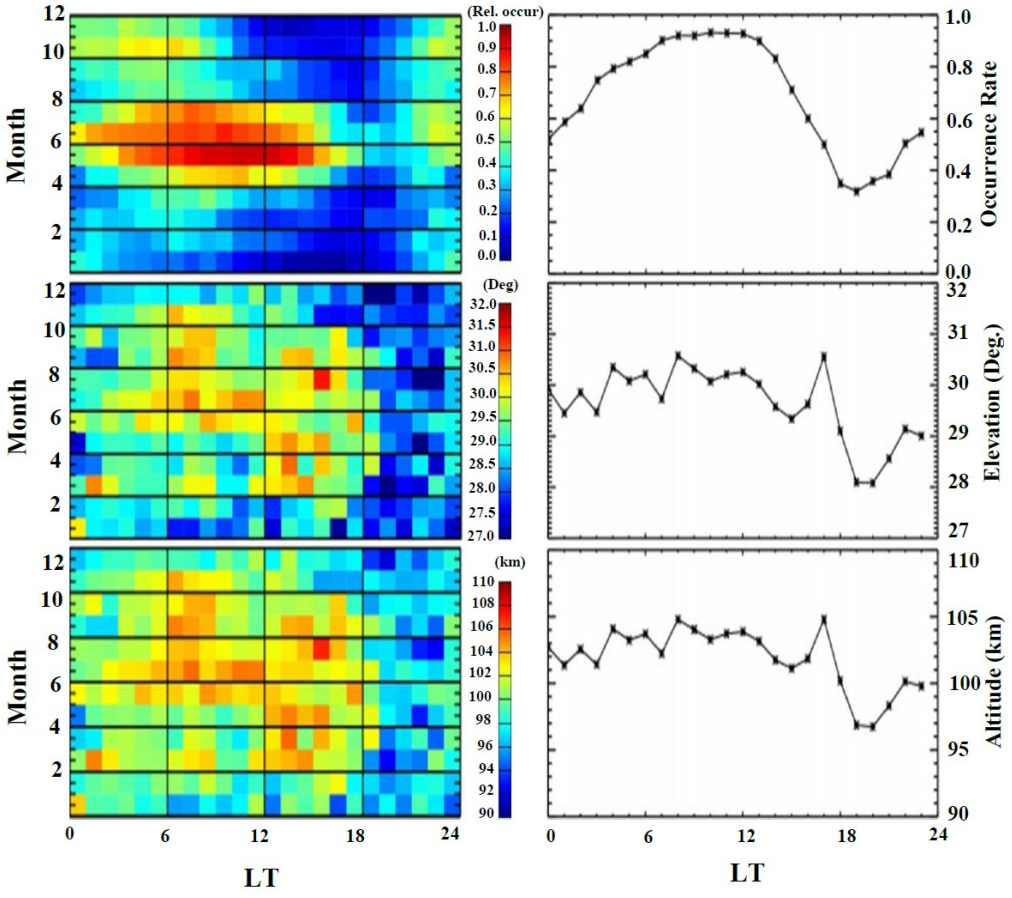

Figure 6.26: Same format as Figure 6.25 but for RKN radar station.

Figure 6.25. The virtual height between 0800 and 1300 LT is ∼102 km. The RKN station gives similar results (Figure 6.26), with the virtual height seen to be ∼103 km in the daytime hours of June. The elevation and virtual height show similar results with those of INV. The result is important in that it indicates that the altitude of the midday summer population is clearly above the PMSE altitude range.

One problem about the determination from elevation angle is that the standard SuperDARN mode of operation assumes 45 km range gate sampling. With this range resolution, (i.e. $\Delta r = 45$ km), $\Delta h \simeq \pm$10-12 km. This uncertainty in the range and height determination is rather large. In order to reduce the uncertainty of individual SuperDARN measurement, a special mode was run with a higher resolution of 15 km. The special experiment was run on August 10, 2013 using the 15 km resolution. The results were carefully processed so as to study the height determination for the region of interest. On August 10, 2013, the first range gate was set to begin at 90 km instead of the 180 km used in the common scan mode with 45 km resolution. With a 15-km range gate size, the uncertainty in height resolution is reduced to ±3–4 km, centering the initial range gate at 97.5 km. The experimental result are presented in Figure 6.27 for a 24-hour RKN data scan which started at 0600 UT (0000 LT). The range-time distribution of the SNR at ranges less than 500 km is given in the top panel for beam 7, and the bottom panel gives the elevation angle.

Consistent close-range echoes were observed between 0000 and 1800 LT, as shown in the top panel of Figure 6.27. However, after 1800 LT, the close-range echoes became rather infrequent. Similarly, during the period of frequent close-range echoes, the angle of arrival (bottom panel) was high.

It is important to note at this point that the SuperDARN interferometer array can only unambiguously measure elevation angles less than ∼40°. The reason for this is due to the considerable distance for SuperDARN radars between the main and interferometer arrays. As shown in the illustration of Figure 3.9 for this study, the separation d between the main and interferometer arrays is 100 m. The operating frequencies for the radar is near 10 MHz, which consequently gives a wavelength of ≈30 m; the interferometer spacing is therefore larger than the wavelength of HF signal (i.e. $\lambda < d$). This results in a 2π ambiguity problem or vertical angle-of-arrival *aliasing* effect, as the phase difference *measured* in the range of

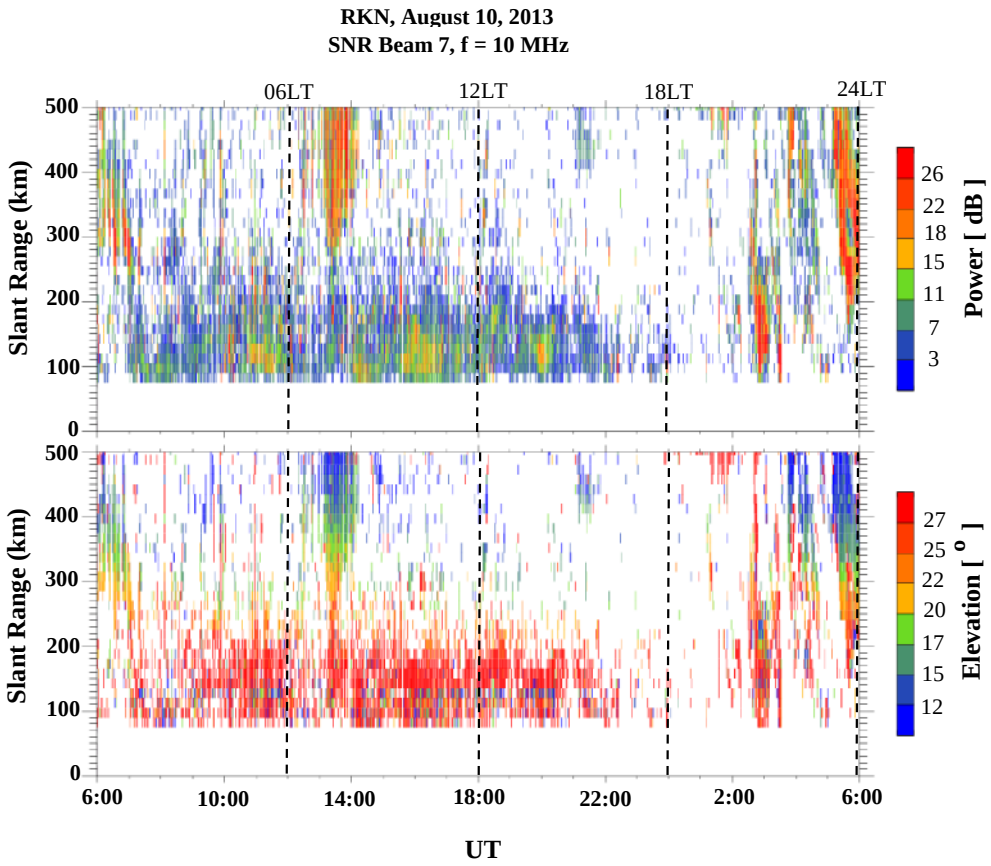

Figure 6.27: Range-time plots for RKN, beam 7 at 10 MHz during 24-hour period beginning from 0600 UT. The SNR (top panel) and elevation angle (bottom panel) are shown and close-range echoes are observed between 0000 and 1800 LT.

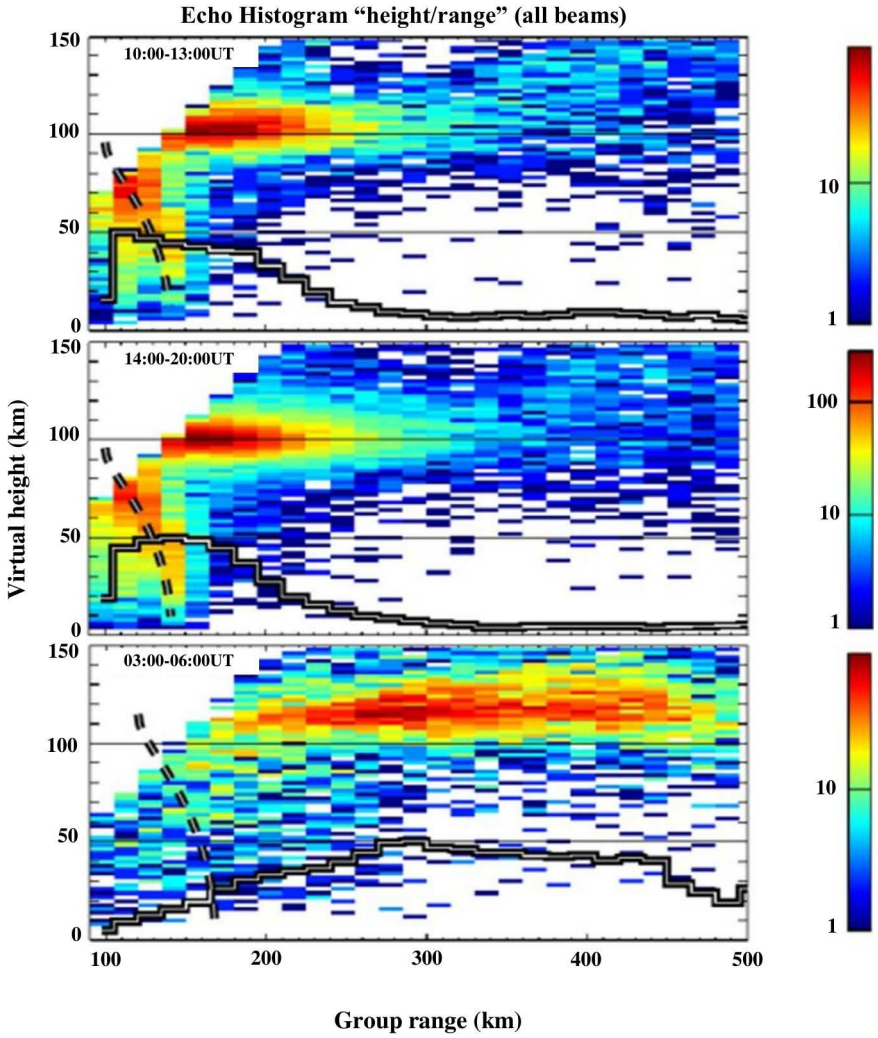

Figure 6.28: Close-range HF backscatter on August 10, 2013, using 15-km high resolution data. Height-range histogram density plots for local morning (top panel - 0400–0700 LT [=1000–1300 UT]), daytime (middle panel - 1000–1300 LT [=1400–2000 UT]) and pre-midnight (bottom panel - 2100–2300 LT [0300–0600 UT]) populations respectively. Height distortions at ranges $\leq$150 km due to 2π ambiguity in the interferometer measurements are shown in the dashed line. The height-integrated number of echoes observed at each range gate are shown as solid step-like line, (*Ponomarenko et al.*, 2015).

$-\pi$ to π between arriving signals at both the main and interferometer arrays, differs by an unknown multiple of 2π from the *total* phase difference (*André et al.*, 1998; *Milan et al.*, 1997a; *Ponomarenko et al.*, 2011). Thus, any backscatters that occurs at an elevation angles greater than 40° will be recorded as lower elevation angles.

Figure 6.28 (top panel) presents a histogram density plot of the morning (0400–0700 LT) population of echoes. The maximum occurrence is centered near 100 km altitude. A similar result is obtained for the daytime (1000–1300 LT) population of echoes (Figure 6.28 (middle panel)). At ranges ≥150 km, the maximum occurrence is centered near 100 km altitude. A normalized histogram estimated from total number of echoes observed at each range gate is shown as the solid step-like line shown in each plot for different time intervals. The decrease in echoes observed at the first few ranges is due to the fact that the echoes are below the maximum occurrence altitude of 100 km.

Since the virtual height has a direct relationship with elevation angle (as can be seen from Equation (6.1)), the virtual height estimates should vary in the same way with range as does the elevation angle. For a flat Earth approximation (where $\varepsilon = \sin^{-1}(h/r)$), we would expect the elevation angle to decrease as range increases. However, for ranges $\leq$ 150 km, a flip over or height distortion is seen (Figure 6.28 top and middle panels). This distortion is due to the 2π ambiguity problem of interferometry arrays previously mentioned.

On the other hand, the pre-midnight population (2100–2300 LT [=0300–0600 UT]) presented in Figure 6.28 (bottom panel), shows that the virtual height is centered between 110 and 125 km, with the near boundary of the close-range echoes shifted to farther ranges, and showing no 2π ambiguity. This altitude range is a little higher than expected for normal E region echoes, but this is expected since straight line propagation is assumed and the small amount of bending by refraction was not considered in the present study (*Milan and Lester*, 1999; *Milan et al.*, 2001).

6.3.2 Summary

This chapter started with a detailed analysis of echo occurrence at different radars in the polar, high- and mid-latitudes. The echoes under consideration were from the closest ranges of the SuperDARN HF radars.

Daily and monthly analysis were done. It was shown that the echo occurrence within the common field-of-view of all radars considered varied with time of day. In general, the frequency of echo occurrence is high during the daytime hours beginning around 0600 LT and peaks by noon until it begins to decrease with a minimum at dusk. The characteristics of the echoes also show seasonal variations. The summer months show a high frequency of occurrence which starts to increase in May, reaches a maximum in June and July and begins to decrease after August. We explored the nature of the variation of the echoes for the first range gate by considering different look directions of the radar beams and found that the echoes do not strongly depend on the beam number or look direction. These late morning/early afternoon results were similar from year to year.

In an attempt to understand the latitudinal dependence of the close-range echoes, data from the polar to high- and mid-latitudes were investigated. Even though the magnitude varies from one radar to the next, the midday summer echoes were present for all radars and more frequent. The evening population is more visible for the auroral latitudes and disappears from the lower latitudes.

Furthermore, the characteristics of the echoes with respect to SNR, Doppler velocity and spectral width were investigated. The daytime hours have an average SNR of about 30 dB, and no significant difference in the average SNR between the summer and the winter months was observed. The Doppler velocity is about ± 40 m s $^{-1}$ and spectral width is about 50 m s $^{-1}$ during the daytime hours, with no major difference seen in spectral properties between the summer and winter months.

The next chapter discusses the results and describes possible sources for the diurnal and seasonal variations observed for the close-range SuperDARN HF echoes.

Chapter 7

DISCUSSION OF EXPERIMENTAL RESULTS AND OBSERVATIONS

This thesis has studied oblique close-range HF backscatter. Although weak, the echoes are frequently observed by the SuperDARN radars at short ranges. The dataset of the first range gate of the SuperDARN radar corresponds to ranges between 180-255 km. To understand the nature and sources of these echoes, and to be able to explain them, we began our analysis by computing and analyzing the echo occurrence rates for the first-range gate with SNR greater than 6 dB (to reduce noise effect). The statistical analysis made use of data from all 16 beam directions. Due to the large dataset considered, the rate of echo occurrence and other properties were calculated in 1-hr temporal bins covering from 2007 to 2013 (for polar, high- and mid-latitudes).

7.1 Possible Origin of the Three Classes (populations) of SuperDARN Close-Range HF Ionospheric Backscatter

The overall statistical analysis showed that three distinct populations are returned from the oblique short-range (<500 km) HF backscatter. This result is consistent from year to year. The first, second and third populations are detected near dawn (0400–0700 LT), noon (1000–1300 LT) and pre-midnight (2100-2300 LT) respectively. Based on the features of the echoes, we discuss separately the three different classes of echoes that were observed, even though they can overlap. We start briefly with the discussion of the night or pre-midnight population

of echoes followed by the morning (or dawn population). We next turn to the discussion of the midday (or noon) population of echoes which is the primary focus of this thesis, and consider the relation of the observed midday summer echoes to neutral turbulence.

7.1.1 Pre-midnight Population

The pre-midnight population is only observed by radars in the auroral region. The spectral properties of the pre-midnight population (e.g (e, f) of RKN and INV, Figures 6.19 and 6.20) are different from those of other radars. For instance, the Doppler shifts are larger than the other short range echoes and are drifting with the same sign as that of the ordinary E region echoes found at larger ranges (*Ponomarenko et al.*, 2015). The August 10, 2013 short pulse experiments show that the virtual height for the pre-midnight population of echoes is between 110 and 125 km (if straight line propagation is assumed). This altitude is somewhat higher than for Farley Buneman waves as discussed in Chapter 4 (*Buneman*, 1963; *Farley*, 1963), but we must recall that our estimates do not include bending near the scattering altitude. Even though their properties are somewhat similar to normal E region echoes, they are still weaker and with smaller Doppler shifts but at higher aspect angles.

The fact that the Doppler velocities of this class of echoes have smaller Doppler velocities than the normal E region echoes suggests that the measurements could refer to observations at large aspect angles, where the irregularities generating the echoes are propagating outside the orthogonality condition. According to Equation (4.18), it follows that as Ψ increases with aspect angle (α_a), the phase velocity decreases monotonically according to $\omega_r = kv_d/(1+\Psi)$. Hence, the production of pre-midnight echoes can indeed be related to large aspect angles. Linear theory predicts that at large aspect angles, inferred from our elevation angles and range calculations, the structures should decay and not grow. We should note that this is not the first time that Farley Buneman waves have been observed at large aspect angles and reported at a variety of radar frequencies, namely, HF and UHF (e.g. *Foster et al.*, 1992; *Milan et al.*, 2004; *Moorcroft*, 1985, 1996).

Milan et al. (2004) have also concluded that the irregularities responsible for this scattering are not field-aligned. These authors documented the properties of these echoes which they called HAIR, and indicated that they were associated with the FB and GD instabilities.

However, while we would agree that the structures cannot grow at the large aspect angles, *Drexler and St Maurice* (2005) have pointed out that because the eigenfrequency is actually a function of altitude, the aspect angles of the structures have to increase monotonically with time, (whether or not the structures are growing or decaying). But when the aspect angle has grown too much, the structures start to decay. Therefore, the evolution of the structures continues after they have reached their maximum amplitude, and are not eliminated but rather decay without having to suddenly crash once they have reached their maximum amplitude. *Drexler and St Maurice* (2005) also argued that since the HAIR structures generated with large aspect angles are strongly damped and are not directly generated, it is possible that the HAIR echoes could have been nonlinearly produced from the caustics in the large amplitude evolution of large wavelength structures. When HAIR echoes are observed, they are weaker than those from the normal irregularities, which means that they might only be visible at close ranges. Lastly, the pre-midnight echoes are restricted to auroral latitudes. For these class of echoes have higher Doppler shifts compared to other classes but are lower than the normal E region echoes observed at small aspect angles.

7.1.2 Morning Population

The population observed in the dawn sector is detected by all radars. This backscatter class of returns is most likely due to meteor trails. The diurnal variability of echo rates for the early morning to dawn (0600 LT) population is very conspicuous as they are detected during almost all months (e.g. near 0600 LT in Figure 6.9, Figure 6.10). These results are consistent with previous observations of the meteor occurrence (*Hall et al.*, 1997; *Hussey et al.*, 2000; *McKinley*, 1961). The diurnal variability of meteor echoes is explained by Earth's orbital motion. Higher counts are expected to be more in the morning because the morning sector (dawn hours) is that part in the Earth's orbit that takes the lead, thus intercepting all the meteoroids moving in the direction opposite to its motion (Figure 5.2). Slower meteors that are traveling in the same direction may even be detectable in the dawn sector.

Aside from various showers, meteor echoes are present throughout the year, though an annual (seasonal) variation is expected due to the inclination of the Earth's axis with respect to the ecliptic plane (*Ceplecha et al.*, 1998; *Jenkins and Jarvis*, 1999). Results from this study

of close-range backscatter (for the different years and beams (look directions), (e.g. Figures 6.9, 6.10, 6.15)) show broad maximum for all seasons except in spring (especially in March) where a minimum is seen for the dawn population (around 0600 LT) (e.g. Figures 6.9 and 6.10). This behavior agrees well with previous studies for meteors (e.g. *Singer et al.*, 2005; *Szasz et al.*, 2005).

Singer et al. (2004), show strong annual variation with highest values observed during summer, and winter showing the lowest rates. Their results were based on measurements from the Northern Hemisphere at an Arctic site (at Andenes, 69.3° N) of a SKYiMET 33 MHz interferometry meteor radar and at a mid-latitude radar (at Juliusruh, 54.6° N). The daily meteor occurrence showed a strong annual variation for the two radars that were used, revealing a marked peak in June/July and broad minimum during January/February. *Singer et al.* (2004) showed results that are in agreement with the much earlier study by *Hawkins* (1956) who reported a strong sporadic meteor occurrence maximum in June/July and minimum in February, using a 53 MHz radar at Jodrell Bank, UK (53.3° N). A detailed study carried out by *Younger et al.* (2009) (using Esrange radar at Sweden (68° N); Ascension Island (8° S) and Rothera radar at Antarctica (68° S)) revealed similar seasonal variations (but with minimum in March) in the distribution of sporadic meteor in the atmosphere. It must be pointed out that the time of day for which the maximum meteor occurrence is observed for these studies is ∼0700 LT (near the dawn hour) which is to be expected for meteors as has been discussed earlier. These studies have attributed the seasonal variations of the sporadic meteor radiants (maximum sporadic meteor occurrence detected in summer and winter months and a minimum in equinoctial months) to the Earth's rotation about its own axis and the annual rotation of the Earth around the Sun in relation to the discrete number of sporadic meteor sources located close to the ecliptic plane.

The flux of meteoroid at the Earth is dominated by sporadic meteors (*Baggaley*, 2002; *Ceplecha et al.*, 1998). The deposition and distribution of sporadic meteors is anisotropic in direction and random in time. Some studies, (e.g. *Campbell-Brown and Jones*, 2006; *Ceplecha et al.*, 1998) have shown for instance, that sporadic meteors appear in six distinct sources relative to the Sun. There are the helion (sunward) and the anti-helion (anti-sunward) sources, which lies in the plane of the ecliptic and are located 60°-70° from the apex direction.

Two of the other sources are the prograde and the retrograde apex sources. Lastly, there are the north and south toroidal sources. The sources' positions come from the Earth's motion about the Sun and the meteoroid distribution about the Sun (*Hawkins*, 1956; *Jones and Brown*, 1993; *Weiss et al.*, 1960). Factors such as the sensitivity of different radars, the location of observing sites and its relation to the position of the sources, can affect the relative strength of individual sources (*Campbell-Brown and Jones*, 2006; *Ceplecha et al.*, 1998; *Singer et al.*, 2004). This implies that the observed/detected meteors will vary according to which sources are in the FOV of the radar and the sensitivity of the radar, (*Younger et al.*, 2009).

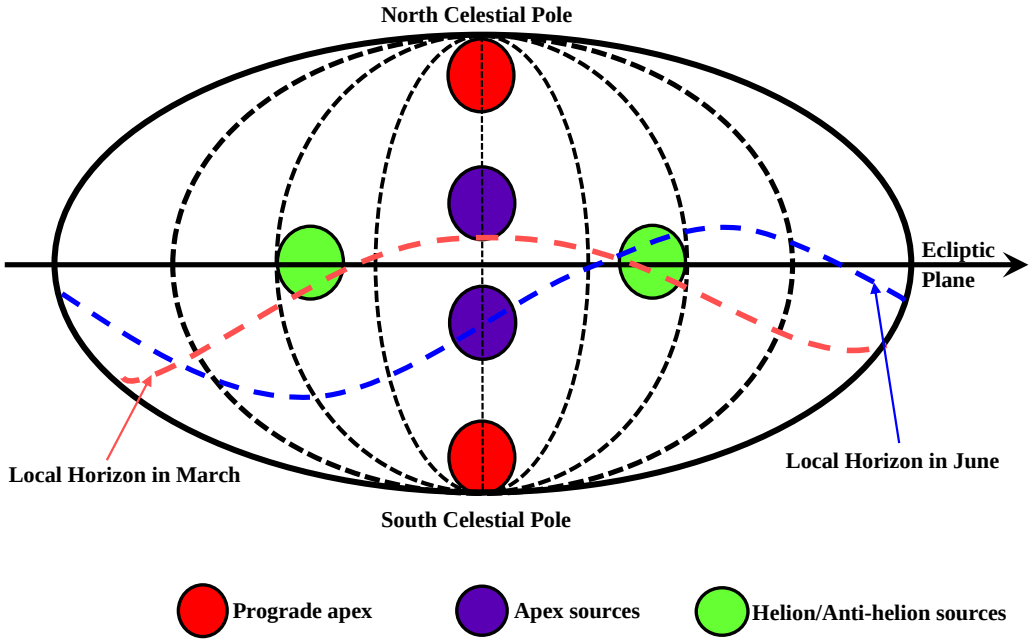

Figure 7.1: Illustration of the Ecliptic coordinate frame showing the sporadic sources. The colored green disks are the helion and anti-helion sources. The purple disks are the northern and southern apex sources and the red disks are prograde apex sources. The red and blue dashed lines are the local horizon at Estrange in March and June/July respectively (adapted from *Younger et al.*, 2009).

Our close-range morning (near dawn) population displays a morphology that resembles meteors. The echoes have a minimum rate of occurrence mostly in March for the Northern radars and September in the Southern radar. We can understand the behavior of the occurrence of the dawn population further by using Figure 7.1 (adapted from *Younger et al.*, 2009). The maximum rate of meteor impact is June/July (blue dashed line) and the

minimum is for March (red dashed line). For the month of March, the local horizon is above the southern apex and southern prograde apex source region. Therefore, the radar cannot observe meteors from these source regions. At the same time, the sensitivity of radars to sources like the northern apex and helion and anti-helion sources (are $\sim 20^{\circ}$ close to the local horizon) are lessened. The low meteor count rate observation in March could therefore be attributed to poor viewing geometry. For the months of June and July however, the local horizon is below the helion, anti-helion, southern apex and northern sources, and therefore contributes to the observed count rates (*Younger et al.*, 2009).

Hall et al. (1997) were the first to suggest that the SuperDARN radar can detect meteor echoes at close range (i.e. ranges less than 500 km). Various follow up studies (e.g. *Arnold et al.*, 2001; *Hibbins and Jarvis*, 2008; *Hussey et al.*, 2000) using the SuperDARN radars have investigated the characteristics of these SuperDARN meteor echoes. It has been shown from these studies that meteor echoes at short ranges (<500 km) have characteristics that are different from backscatter returns from plasma irregularities in both the E and F ionospheric regions. They are characterized by low line-of-sight Doppler velocity (± 40 m s^{-1}), and low spectral width (between 1 and 50 m s^{-1} which is consistent with diffusion theory and in agreement with results of *Arnold et al.* (2003)); and an SNR between 3 and 24 dB (*Arnold et al.*, 2001, 2003; *Hall et al.*, 1997; *Hussey et al.*, 2000; *Jenkins and Jarvis*, 1999; *Ogawa et al.*, 2002). In this thesis, the population observed near dawn has spectral properties that agree with previous studies (Figures 6.19, 6.20, 6.21 and 6.22).

In summary, previous studies and this thesis have been able to show that the SuperDARN HF radars are capable of detecting echoes from meteor trails. This thesis however is the most comprehensive done up to date that comprises long term morphological variation of near-range meteor backscatter in multiple latitudes. The magnitude of the velocity of meteor echoes at mesospheric height lies between ± 50 m s^{-1}, which is expected for mesospheric winds. The observation of neutral wind using radars allows mesospheric winds to be studied (*Yukimatu and Tsutsumi*, 2002, 2003), which is important since the wind velocity varies with altitude. SuperDARN radars are therefore able to provide valuable information about the meridional and zonal winds in an important region of the atmosphere.

7.1.3 Midday Summer Population

The main focus of the present study is the midday summer population, whose existence has been reported before but never probed in depth. The results presented in Chapter 6 show that the echoes from close-range are very frequent during the midday summer months, even though they are not that powerful, which makes this population interesting. An important feature is that this population is present in all the radars (north-to-south chain) and in both hemispheres at local summer.

The Case Against PMSEs for the Midday Summer Population

The morphology of the midday summer population resembles that of PMSE. While PMSEs are mostly confined to polar or high latitudes (*Lübken et al.*, 2004), some authors have argued that they can be observed at mid-latitudes (e.g. *Hosokawa et al.*, 2004, 2005; *Ogawa et al.*, 2002). Their results show semidiurnal variation, having maxima at noon (1200-1300 LT), and minima near 0600-0700 LT and 1800-1900 LT. In the present data set, all radars show similar diurnal and seasonal variations. The diurnal and seasonal dependence observed in the present study parallels those known for PMSEs to the points that many previous studies (e.g *Hosokawa et al.*, 2004, 2005; *Ogawa et al.*, 2002) have attributed the SuperDARN echoes at close range to PMSEs, particularly because of the summer occurrence. However, even though the morphology of the current study is similar to previous work, this alone cannot be sufficient to conclude that the midday summer echoes are PMSE.

As for the case that favors PMSE, the morphology and the spectral properties resembles those of PMSEs. Our results reveal Doppler velocities are mostly less than ± 40 m s^{-1}, with spectral widths less than 50 m s^{-1} and echo SNR of less 30 dB. These characteristics including the seasonal behavior, are similar to those summarized by *Röttger* (1994).

On the negative side, most of the PMSE detection has been through the use of vertical (or nearly vertical) incidence (pointing beam) VHF radars with good height resolution, indicating the PMSE altitude to be 80-90 km (*Cho and Röttger*, 1997; *Ecklund and Balsley*, 1981; *Gadsden and Schröder*, 1989; *Hoffmann et al.*, 1999; *Nussbaumer et al.*, 1996; *Zecha et al.,*, 2001; *Zecha and Röttger*, 2009). However, the altitude derived from the SuperDARN

elevation angles of the midday summer echoes is considerably higher than expected for PMSE. Previous studies done with SuperDARN radars only considered the diurnal and seasonal variation of the SuperDARN hypothesized PMSE-HF echoes without looking into the scattering volume location of the backscatter from the midday summer. Our analysis using the elevation angle measurements from the normal scan has revealed that the daytime summer population is from a virtual height of 100 km. The original ±10 km uncertainty was reduced by using a short pulse resolution of 15 km and the altitude was the same with a ±3 km uncertainty. This altitude of 100 km is too high for PMSE, and does not agree with the established altitude of noctilucent clouds known to be linked with PMSE restricted to 80-90 km height range. In addition, the latitudinal spread of the midday summer population of echoes is another case against PMSE. The echoes are seen by all radars at all latitudes and PMSEs are mostly a high latitude phenomenon. These cons thereby indicate that the echoes are not PMSEs. Thus, an alternate mechanism has to be responsible for the generation of the more frequent but weak daytime close-range echoes that are observed across a broad range of latitudes. We now discuss possible generation mechanisms starting with plasma irregularities and meteor echoes.

The Case Against Plasma Instabilities for the Midday Summer Population

The midday summer echoes cannot be related to plasma instabilities because the echoes occur at the time of day when plasma irregularities are usually not observed. For one thing, SuperDARN radars detect the structures at a broad range of latitudes. Also, there is no sign of auroral activity in the middle of the day for the PolarDARN radars. Hence, the midday summer class of backscatter cannot be associated with plasma irregularities of the auroral type. Moreover, the altitude at which these echoes originate is around 100 km which is lower than expected from plasma instabilities: as discussed in subsection 7.1.1 even if plasma irregularities with small Doppler shift could form there, very strong electric fields (highly unlikely for the reasons given above) would be required in order to generate radar returns at low altitudes (*Dimant and Sudan*, 1995a,b, 1997).

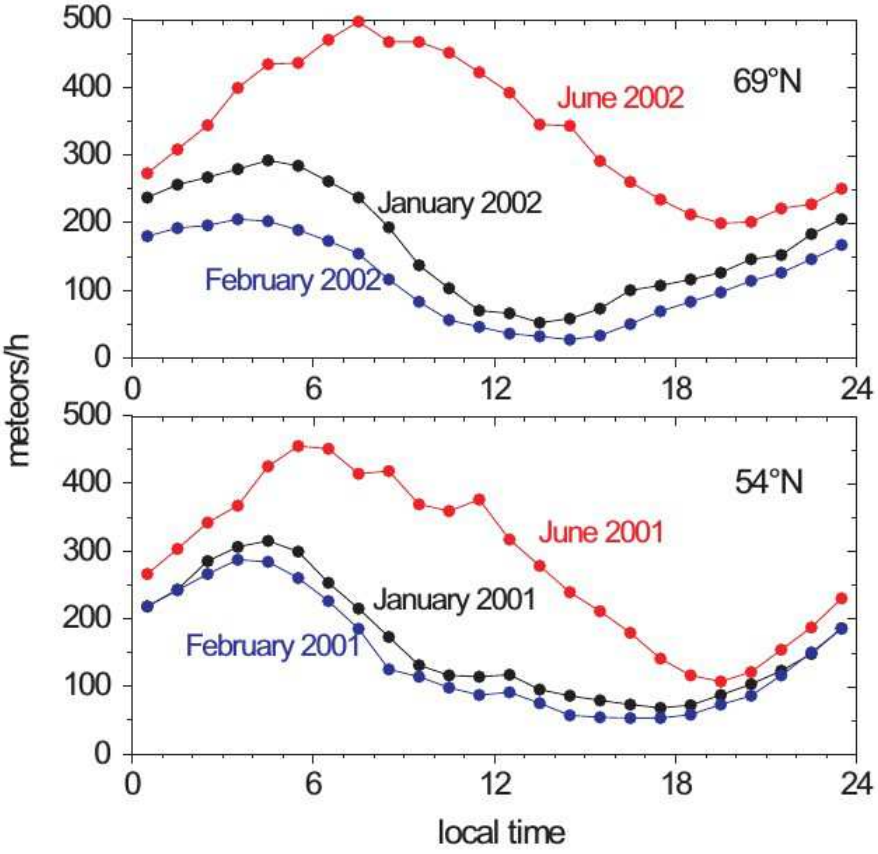

Figure 7.2: Diurnal and monthly variations in meteor rates January, February, and June at mid-latitudes and Arctic latitudes (*Singer et al.*, 2004).

The Case For and Against Meteors as Cause of Midday Summer Near-range Echoes

Meteors occur throughout the year and at all times of the day. The results of the morning/dawn population as discussed is subsection 7.1.2 have shown that meteors are indeed present at various latitudes and their occurrence rates show the expected diurnal and seasonal dependence.

The midday summer population has many similarities with meteor echoes. It has the same altitude (100 km) as that of the dawn (meteor) class. Also, the power of the daytime summer population is comparable to that observed in the morning population. Finally, the frequency of occurrence is higher in summer, just as in the meteor situation (Figure 7.2). One thing that introduces doubt about a meteor interpretation for the midday summer population is the time of occurrence. Meteors peak near 0600 LT, as seen in the specialized

meteor radars like SKiMET (*Younger et al.*, 2009). Figure 7.2 presents the diurnal and monthly variations of meteor rates at two latitudes (*Singer et al.*, 2004). The meteor peak occurrence rate is still near dawn, not noon. The occurrence is higher at noon in summer than at 0600 LT in winter. Hence, if increased rates are seen in winter at dawn, more echoes should also be seen at noon in summer. A central question is: why do the SuperDARN close-range backscatter peak at midday if they come from meteor trails? It could be that the meteor contribution is related to the look direction (boresight) which may change the occurrence in the presence of meteor showers (as opposed to sporadic meteorites). Further analysis to check this possibility is beyond the scope of the present study and will not be considered here.

Could Neutral Turbulence be the Cause of the Midday Summer Population?

Another possible mechanism for the generation of the midday summer echoes is related to the altitude. The properties of the midday summer echoes are consistent with the neutral wind and the altitude from which they originate is 100 km. Supposing that the occurrence of these echoes is attributed to neutral turbulence, the important question to answer is whether it is reasonable to attribute irregularities produced in the region of 100 km and below to neutral turbulence. The other question to answer is why only in summer?

The altitude in which the midday population is observed is interesting because there are often very intense shears at 100 km (*Larsen*, 2000, 2002). The shears are apparently unstable to the Kelvin-Helmholtz (KH) instability and the turbulence that goes with it. Large wind shears in association with Kelvin-Helmholtz turbulent billow structures (with 5 km horizontal spacing and vertical extent of about 3 km) have been observed in the height range from 90–110 km altitude range (*Bishop*, 2004; *Hecht et al.*, 2004; *Larsen*, 2000, 2002). The turbulence generated by the large scale KH instability goes down to the viscous subrange (*Fritts et al.*, 1996). That subrange at 100 km is close to the 10 m scales accessed by SuperDARN near 100 km (Figure 7.3, taken from *Kelley* (2009)). The viscous subrange is attainable at 100 km but not so much higher up because it decreases quickly with altitude and we are already a bit too much inside the viscous subrange. Therefore, the lower the better. (Figure 7.3, taken from *Kelley* (2009)).

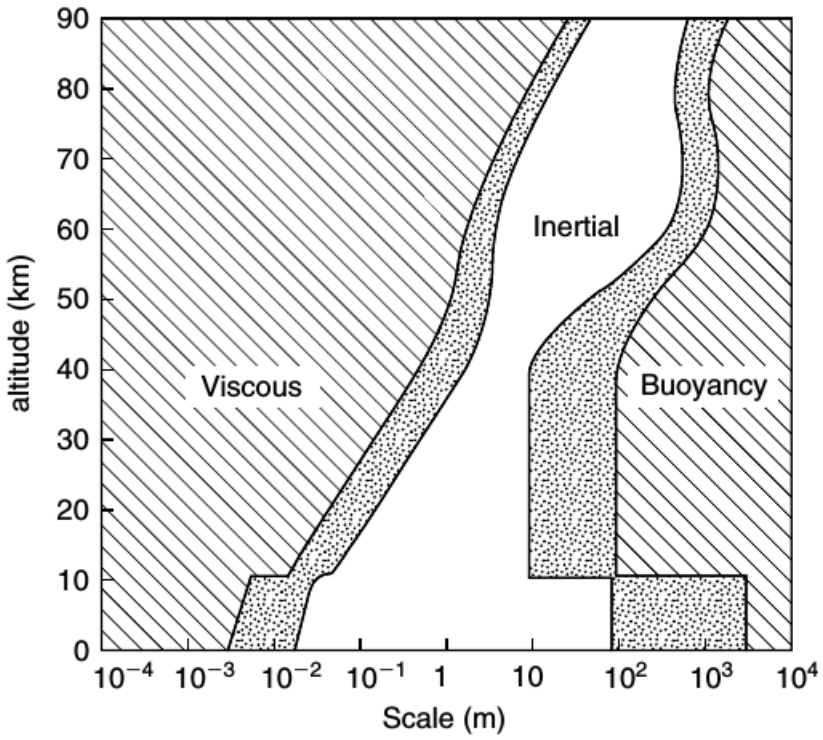

Figure 7.3: The Earth's atmosphere viscous subranges (*courtesy of W. Hocking*), (*Kelley*, 2009).

Direct rocket observations have shown that plasma density can effectively be modulated by the frequent ion-neutral collisions (e.g. *Blix et al.*, 1994, 1996; *Schlegel*, 1992). We can therefore reasonably argue that neutral turbulence generated by intense shears observed at 100 km generate structures down to about 10 m. These echoes are detected with radars because at 100 km (where the ion collision frequency is large ($\nu_i > \Omega_i$)), the ions follow the neutrals but the electrons do not. In that case, the ions will be imaging the neutral structures. The electrons on the other hand (with rather high mobility along the magnetic field) will want to erase any structure that is not sufficiently field-aligned. However, as discussed in relation to plasma instabilities, the fact that the electrons do this and are responsible for the decay of the structures does not mean that the structures will be wiped out. They exist and then decay, but they could decay slowly enough to have a better chance to be detected by radars.

Finally, these neutral turbulence-induced echoes would be seen only in summer because in summer, ionization is at maximum (as compared to winter where it is at a minimum) and reaches down to 100 km (with plasma density of 10^{11} during the day, as shown in Figure 7.4).

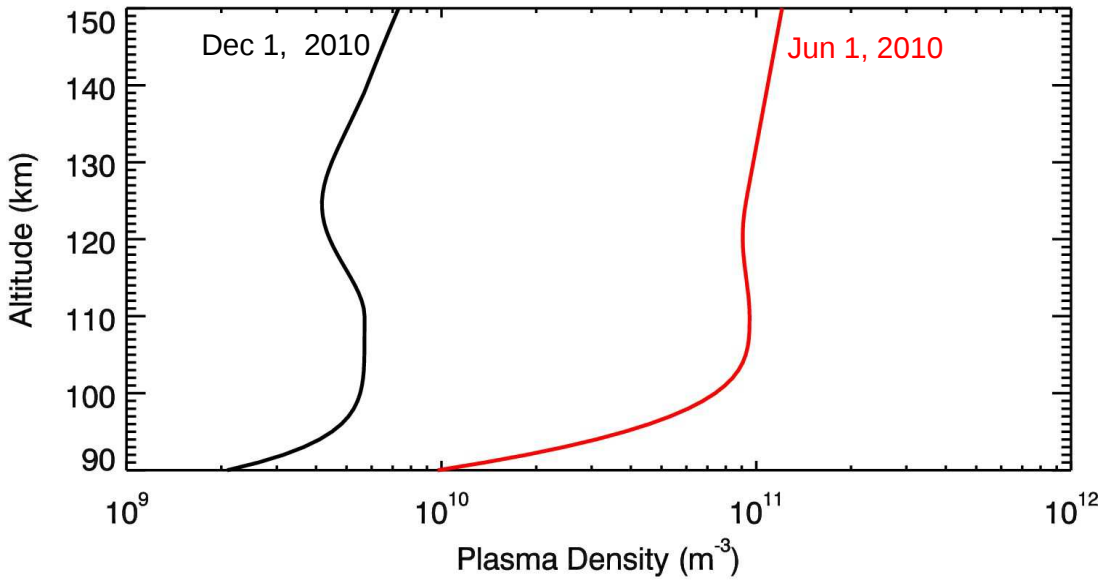

Figure 7.4: Variation of plasma density with altitude at 75° and at noon for winter (December 1 (black line)) and summer (June 1 (red line)) of 2010, in the E region of the ionosphere. Data are obtained from VITMO (Virtual Ionosphere, Thermosphere, Mesosphere Observatory), with courtesy of International Reference Ionosphere - IRI model.

In the middle of the day, photoionization reaches its peak. But, if occasionally the turbulent layers move up, there is a chance for the non field-aligned structures to be seen. However, the problem higher up is that the electrons' very high mobility will short out the structures more efficiently and more rapidly while the 10 m wavelength will put the structures more into the viscous subrange, making them that much weaker and difficult to detect.

Chapter 8

CONCLUSION

The primary goal of this thesis was to document the properties of close-range echoes detected by the SuperDARN HF radars and investigate their possible origin. To this end, a large data set from ten SuperDARN radars from both the Northern and Southern hemispheres was produced and analyzed. The selected radars cover the polar, high- and mid-latitude latitudes. Backscatter was detected from the mesosphere and lower thermosphere region at oblique incidence for the first range gate at 180 km. In order to distinguish the different mechanisms responsible for the generation of the close-range radar returns, statistical analyses were performed on various years of data and for the different radars so as to check for diurnal, seasonal and latitudinal dependences. This helped in the classification of the near-range echoes. Only ionospheric echoes with SNR greater than 6 dB were selected in order to reduce noise effects in the occurrence plots. Different look directions of the radar beams were also studied.

The summary of the findings of this thesis are as follows:

1. A pre-midnight population (2100–2300 LT) of close-range HF backscatter from the E region was observed. This class of echoes is less frequent than the others as it is restricted to the auroral regions. No significant difference was observed from beam to beam thus showing that the echoes do not depend on look direction. The altitude range (110-125 km) from which they originate fits the altitude range for Farley-Buneman and the gradient drift instabilities even though the aspect angles appear to be larger than expected from linear instability theory. They are echoes likely originating from scatter at high aspect angles. It is however feasible to argue that these are the HAIR echoes produced from nonlinear evolution of ordinary echoes. If small aspect angles could be

seen at some time, they would likely be much more powerful and large aspect angles would not be seen. It is possible that the observed structures are just decaying after having gone through maximum amplitude while evolving growing aspect angles. As expected, the Doppler velocities of this population are smaller than the normal E region echoes because they are observed at large aspect angles, where the irregularities generating the echoes are propagated outside the orthogonality condition.

2. The morning/dawn (0400–0700 LT) population is produced by meteors. The population was observed for all radars and also detected almost all year round. Moreover, a similar pattern was observed from one radar to the other (with the exception of CLY), though the echo occurrence frequency differs from auroral to high- and to mid-latitudes radars and also shows seasonal variation with a minimum rate observed in March. The line-of-sight velocities are comparable to wind velocities expected for mesospheric heights and echoes from this morning population are therefore useful for neutral wind studies.

3. The midday (1000–1300 LT) population is observed in summer only. This population has an echo occurrence pattern that is consistent from year to year. The Doppler shifts of this population are small ($\pm$40 m s^{-1}) and the spectral width is relatively narrow (50 m s^{-1} or less). Although the morphology of this population resembles that of PMSEs from noctilucent clouds at 80-90 km altitude, they do not originate from the same altitude region as PMSE. The analysis of this study using the elevation angle has shown that the daytime population comes from a virtual height centered at 100$\pm$3-4 km. Therefore, the PMSE mechanism could not be responsible for the midday summer backscatter. There is likelihood of meteors being present since they have the same height as meteors and have summer peak. This could be due to the particular look direction of individual radars. The possibility of meteor contribution to the midday summer population is worth investigating in the future.

   The alternative mechanism for generation of midday summer echoes is linked to large shears associated with neutral turbulence near 100 km altitude in the lower E region. In this lower part of the E region (100 km), the electrons are magnetized but

the ions are unmagnetized as a results of high collision frequency with the neutrals. The close coupling of the ions with the neutrals forces the ions to be moved around by the neutrals before having the electrons damp the structure through diffusion along the magnetic field. Direct rocket observations have confirmed strong shears at 100 km. These shears are KH unstable and the turbulence generated by the large scale KH instability goes down to the viscous subrange which increases rapidly with altitude but at 100 km is close to 10 m scales accessed by the SuperDARN. The observations cannot be due to the gradient drift or Farley-Buneman structures which according to linear theory require large electric fields at those heights. This summer occurrence of this population would simply be related to the fact that with more background ionization in summer at 100 km and the more accessible subrange at 100 km, the structures would be powerful enough to be seen by SuperDARN in summer only.

For the case of neutral turbulence, it is recommended for future work that the ions and electrons are considered. Computer numerical models should be developed that would take account of having neutral turbulence and producing irregularities in the plasma and then look at how the plasma irregularities evolve.

Bibliography

André, D., G. J. Sofko, K. Baker, and J. MacDougall, SuperDARN interferometry: Meteor echoes and electron densities from groundscatter, *Journal of Geophysical Research, 103*, 7003; 7015, 1998.

Arnold, N. F., T. R. Robinson, M. Lester, P. B. Byrne, and P. J. Chapman, Super Dual Auroral Radar Network observations of fluctuations in the spectral distribution of near range meteor echoes in the upper mesosphere and lower thermosphere, *Annales Geophysicae, 19* 425-434, 2001.

Arnold, N. F., P.A. Cook, T. R. Robinson, M. Lester, P. J. Chapman and N. Mitchell, Comparison of D-region Doppler drift winds measured by the SuperDARN Finland HF radar over an annual cycle using the Kiruna VHF meteor radar, *Annales Geophysicae, 21*(10) 2073-2082, 2003.

Baggaley, W. J., Radar observations: Meteors in the Earths atmosphere, *Cambridge University Press*, 123-148, 2002.

Baker, K.B., R. A. Greenwald, J. P. Villian, and S. Wing, Spectral characteristics of high frequency (HF) backscatter for high latitude ionospheric irregularities: Preliminary analysis of statistical properties, *JOHNS HOPKINS UNIV LAUREL MD APPLIED PHYSICS LAB.*, 1988.

Bauer, S. J., Physics of planetary ionospheres, *Berlin, New York, Springer*, 1973.

Bishop, R. L., M. F. Larsen, J. H. Hecht, A. Z. Liu, and C. S. Gardner, TOMEX: Mesospheric and lower thermospheric diffusivities and instability layers, *Journal of Geophysical Research: Atmospheres (1984-2012), 109*(D02S03), doi:10.1029/2002JD003079, 2004.

Blix, T. A., E. V. Thrane, S. Kirkwood, K. Schlegel, Plasma instabilities in the lower E-region observed during the DYANA campaign, *Journal of Atmospheric and Terrestial Physics, 56*(13) 1853-1870, 1994.

Blix, T. A, E. V. Thrane, S. Kirkwood, Y. S. Dimant, R. N. Sudan, Experimental evidence for unstable waves in the lower E/Upper D-region excited near the bisector between the electric field and the drift velocity, *Geophysical research letters, 23*(16), 2137-2140, 1996.

Booker, H. G., A theory of scattering by nonisotropic irregularities with application to radar reflection from the aurora, *Journal of Atmospheric and TerrestialPhysics*(8), 204-221, 1956.

Brasseur, G., and S. Solomon, Aeronomy of the middle atmosphere: Chemistry and physics of the stratosphere and mesosphere, *Atmospheric Science Library* 73-76, 1986.

Brasseur, G., and S. Solomon, Aeronomy of the middle atmosphere: Chemistry and physics of the stratosphere and mesosphere, *Springer Science and Business Media, 3rd Edition, 32*, 75-77, 2006.

Bremer, J., P. Hoffman, A. H. Manson, C. E. Meek, R. R*ü*ster, and W. Singer, PMSE observations at three different frequencies in northern Europe during summer 1994, *Annales Geophysicae 14*, 1317-1327, 1996.

Bremer, J., P. Hoffmann, R. Latteck, and W. Singer, Seasonal and long-term variations of PMSE from VHF radar observations at Andenes, Norway, *Journal of Geophysical Research, 108*(D8) 8438, doi:10.10292002JD002369, 2003.

Bremer, J., Hoffmann, P., Latteck, R., Singer,W., M. Zecha, Long-term changes of (polar) mesosphere summer echoes, *Journal of Atmospheric and Solar-Terrestrial Physics, 71* 1571-1576, 2009.

Buneman, O., Excitation of field aligned sound waves by electron streams, *Physical Review Letters, 10*, 285, 1963.

Campbell-Brown, M. D. and J. Jones, Annual variation of sporadic radar meteor rates, *Monthly Notices of the Royal Astronomical Society, 367*(2), 709-716, 2006.

Ceplecha, Z, J. Borovi̇ĉka, W. G. Elford, D. O. ReVelle, R. L. Hawkes, V. Porubĉan and M. Ŝimek, Meteor phenomena and bodies, *Space Science Reviews, 84*(3-4), 327-471, 1998.

Chapman, S., The absorption and dissociative or ionizing effect of monochromatic radiation in an atmosphere on a rotating Earth, *Proceedings of Physical Society, 43*, 26- 45, 1931a.

Chapman, S., The absorption and dissociative or ionizing effect of monochromatic radiation in an atmosphere on a rotating Earth, part ii. grazing incidence, *Proceedings of Physical Society, 43*, 483-501, 1931b.

Chisham, G., I. J. Coleman, M. P. Freeman, M. Pinnock, and M. Lester, Ionospheric signatures of split reconnection X-lines during conditions of IMF Bz < 0 *and* |By| $\sim$ |Bz|: Evidence for the antiparallel merging hypothesis, *Journal of Geophysical Research, 107*(1323), doi:10.1029/2001JA009124, 2001.

Chisham, G., M. Lester, S. E. Milan, M. P. Freeman, W. A. Bristow, A. Grocott, K. A. McWilliams, J. M. Ruohoniemi, T. K. Yeoman, P. L. Dyson, R. A. Greenwald, T. Kikuchi, M. Pinnock, J. P. S. Rash, N. Sato, G. J. Sofko, J.-P. Villain, A. D. M. Walker, A decade of the Super Dual Auroral Radar Network (SuperDARN): Scientific achievements, new techniques and future directions *Surveys in Geophysics, 28*(1), 33-109, 2007.

Chisham, G., and M. P. Freeman, A reassessment of SuperDARN meteor echoes from the upper mesosphere and lower thermosphere, *Journal of Atmospheric and Solar-Terrestrial Physics, 102*, 207-221, 2013.

Cho. J. Y. N. and M. C. Kelley, Polar mesosphere summer radar echoes: Observations and current theories, *Review of Geophysics, 31*, 243-265, 1993.

Cho. J. Y. N. and J. Röttger, An updated review of polar mesosphere summer echoes: Observation, theory, and their relationship to noctilucent clouds and subvisible aerosols, *Journal of Geophysical Research: Atmospheres (1984-2012), 102*(D2), 2001-2020, 1997.

Choudhuri, A. R., The physics of fluids and plasmas: an introduction for astrophysicists, *Cambridge University Press*, 259–260, 1998.

Czechowsky, P., Reid, I.M., Rüster, R., and Schmidt, G. VHF radar echoes observed in the summer and winter polar mesosphere over Andoya, Norway, *Journal of Geophysical Research, 94*, 6199-5217, 1989.

Dalin, P., N. Pertsev, A. Zadorozhny, M. Connors, I. Schofield, I. Shelton, M. Zalcik, T. McEwan, I. McEachran, S. Frandsen, O. Hansen, H. Andersen, V. Sukhodoev, V. Perminov, and V. Romejko, Ground-based observations of noctilucent clouds with a northern hemisphere network of automatic digital cameras, *Journal of Atmospheric and Solar-Terrestrial Physics, 70*, 1460-1472, 2008.

Davies, K., Ionospheric radio, *IEE Electromagnetic Waves Series 31*, Peter Peregrinus Ltd., London, 1990.

Dimant, Y. S. and R. N. Sudan, Kinetic theory of low-frequency cross-field instability in a weakly ionized plasma. I. Physics of plasmas, *Journal of Geophysical Research: Space Physics (1994-present), 2*(4), 1157-1168, 1995a.

Dimant, Y. S. and R. N. Sudan, Kinetic theory of the Farley-Buneman instability in the E region of the ionosphere, *Journal of Geophysical Research: Space Physics (1978-2012), 100*(A8), 14605-14623, 1995b.

Dimant, Y. S. and R. N. Sudan, Physical nature of a new cross-field current-driven instability in the lower ionosphere, *Journal of Geophysical Research: Space Physics (1978-2012), 102*(A2), 2551-2563, 1997.

Drexler, J., J. -P. St.-Maurice, D. Chen, and D. R. Moorcroft, New insights from a non-local generalization of the Farley-Buneman instability problem at high latitudes *Annales Geophysicae, 20*(12), 2003-2025, 2002.

Drexler, J. and J. -P. St.-Maurice, A possible origin for large aspect angle "HAIR" echoes seen by SuperDARN radars in the E region, *Annales Geophysicae, 23*(3), 767-772, 2005.

Dyrud, L. P., M. M. Oppenheim, and A. F. vom Endt, The anomalous diffusion of meteor trails, *Geophysical Research Letters, 28*, 2775-2778, 2001.

Ecklund, W. L., and B. B. Balsley, Long-term observations of the Arctic mesosphere with the MST radar at Poker Flat, Alaska, *Journal Geophysical Research, 86*, 7775, 1981.

Farley, D. T., A plasma instability resulting in field-aligned irregularities in the ionosphere, *Journal of Geophysical Research, 68* (22), 6083-6097, 1963.

Fejer, B. G., and M. C. Kelley, Ionospheric irregularities, *Review of Geophysics, 18*(2), 401-454, 1980.

Fejer, Bela G., J. Providakes, D. T. Farley, Theory of plasma waves in the auroral E region, *Journal of Geophysical Research, 89*,A9: 7487-7494, 1984.

Fleming, E. L., S. Chandra, M. R. . Schoeberl and J. J. Barnett, Monthly Mean global climatology of temperature, wind, geopotential height, and pressure for 0-120 km, *NASA Tech Memo 100697*, 85 pp, 1988.

Foster, J. C., D. C. Tetenbaum, C. F. Pozo, J.-P. St. Maurice, and D. R.Moorcroft, Aspect angle variations in intensity, phase velocity, and altitude for high-latitude 34-cm E region irregularities, *Journal of Geophysical Research: Space Physics (1978-2012), 97*(A6), 8601-8617, 1992.

Fritts, D. C., J. F. Garten and Ø. Andreassen, Wave breaking and transition to turbulence in stratified shear flows, *Journal of Atmospheric Sciences, 53*(8), 1057-1085, 1996.

Fritts and Alexander, Gravity Waves Dynamics and Effects in the Middle Atmosphere, *Reviews of Geophysics, 41*, 1/1003, doi:1029/2001RG00006, 2003.

Gadsden, M., and Schröder, W. Noctilucent clouds, *Springer-Verlag, New York*, 1989.

Gillies, D., Global-scale observations of changes in ionospheric echo occurrence and convection during periods of increased solar wind activity and increased geomagnetic activity, (*PhD Thesis, Physics and Engineering Physics, University of Saskatchewan*), 2012.

Greenwald, R. A., K. B. Baker, R. A. Hutchins, and C. Hanuise, An HF phased array radar for studying small-scale structure in the high-latitude ionosphere, *Radio Science, 20*, N1, 63-79, 1985.

Greenwald, R. A., K. B. Baker, J. R. Dudeney, M. Pinnock, T. B. Jones, E. C. Thomas, J. P. Villain, J. C. Cerisier, C. Senior, C. Hanuise, R. D. Hunsucker, G. Sofko, J. Koehler, E. Nielsen, R. Pellinen, A. D. M. Walker, N. Sato, and H. Yamagishi, DARN/SuperDARN: A global view of the dynamics of high-latitude convection, *Space Science Review, 71*, 761-793, 1995.

Gurevich, A. V., N. D. Borisov, and K. P. Zybin Ionospheric turbulence induced in the lower part of the E region by the turbulence of the neutral atmosphere *Journal of Geophysical Research: Space Physics (1978-2012), 102*(A1), 379-388, 1997.

Hagfors, T., Note on the scattering of electromagnetic waves from charged dust particles in a plasma, *Journal of Atmospheric and Terrestrial Physics, 54*, 333-338, 1992.

Haldoupis, C., A review on radio studies of auroral E-region ionospheric irregularities, *Annales Geophysicae, 73*, 239-258, 1989.

Hall, G. E., J. M. MacDougall, D. R. Moorcroft, J. -P. St. Maurice, A. H. Manson, and C. E Meek, Super Dual Auroral Radar Network observations of meteor echoes, *Journal of Geophysical Research, 102*(14), 603-614, 1997.

Hall, C.M., J. Röttger, Initial observation of Polar Mesospheric Summer Echoes using the EISCAT Svalbard radar, *Geophysical Research Letters*, vol. 28, 1, pp. 131-134, 2001.

Hall, C. M., On the influence of neutral turbulence ambipolar diffusivities deduced from meteor trail expansion, *Annales Geophysicae, 20*, 1857-1862, doi:10.5194/angeo-20-1857-2002, 2002.

Hargreaves, J. K., The solar-terrestrial environment, *Cambridge Atmospheric and Space Science Series, 5*, Cambridge University Press, 1992.

Hargreaves, J. K., The upper atmosphere and solar-terrestrial relations-An introduction to the aerospace environment, *New York, Van Nostrand Reinhold Co.*, 312 p., 1, 1979.

Havnes, O. and F. Sigernes, On the influence of background dust on radar scattering from meteor trails *Journal of Atmospheric and Solar-Terrestrial Physics, 67*, 659-664, 2005.

Hawkins, G. S, A radio echo survey of sporadic meteor radiants, *Monthly Notices of the Royal Astronomical Society, 116*(1), 92-101, 1956.

Hecht, J. H., A. Z. Liu, R. L. Walterscheid, R. G. Roble, M. F. Larsen, and J. H. Clemmons, Airglow emissions and oxygen mixing ratios from the photometer experiment on the Turbulent Oxygen Mixing Experiment (TOMEX), *Journal of Geophysical Research: Atmospheres (1984-2012, 109*(D02S05), doi:10.1029/2002JD003035, 2004.

Hibbins, R. E., and M. J. Jarvis, A long-term comparison of wind and tide measurements in the upper mesosphere recorded with an imaging Doppler interferometer and SuperDARN radar at Halley, Antarctica, *The Tsunami Threat - Research and Technology, 8*(5), 1367-1376, 2008.

Hines, C. O., Internal Atmospheric Gravity Waves at Ionospheric Heights, *Canadian Journal of Physics, 38*, 1441-1481, 1960.

Hines, C. O., The Upper Atmosphere in Motion, *American Geophysical Union*, Washington, DC, pg 174, 1974.

Hocking, W. K., T. Thayaparan, and J. Jones, Meteor decay times and their use in determining a diagnostic mesospheric temperature-pressure parameter: methodology and one year of data, *Geophysical Research Letters, 24*, 2977-2980, 1997.

Hoffmann, P., W. Singer, and J. Bremer, Mean seasonal and diurnal variations of PMSE and winds from 4 years of radar observations at ALOMAR, *Geophysical Research Letters, 26*, 1525-1528, 1999.

Holton, J. R., The Role of gravity waves induced drag and diffusion in the momentum budget of the mesosphere, *Journal Atmospheric Science, 39*, 791-799, 1982.

Holton, J. R., The Influence of gravity waves breaking on the general circulation of the middle atmosphere, *Journal of Atmospheric Science, 40*, 2497-2507, 1983.

Hoppe, U.-P., C. Hall, and J. Röttger, First observations of summer polar mesospheric backscatter with a 224 MHz radar, *Geophysical Research Letters, 15*, 28-31, 1988.

Hosokawa, K., T. Ogawa, A. S. Yukimatu, N. Sato, and T. Iyemori, Statistics of Antarctica mesospheric echoes observed with the SuperDARN Syowa radar, *Geophysical Research Letters, 31*, L02106, doi:10.1029 2003GL018776, 2004.

Hosokawa, K., T. Ogawa, N. F. Arnold, M. Lester, N. Sato, and A. S. Yukimatu, Extraction of polar mesosphere summer echoes from SuperDARN data, *Geophysical Research Letters, 32*, 10.1029/2005GL022788, 2005.

Hussey,G. C., C. E. Meek, D. Andr é, A. H. Manson, G. J. Sofko, C. M. Hall, A comparison of Northern Hemisphere winds using SuperDARN meteor trail and MF radar wind measurements, *Journal of Geophysical Research 105*, 18053-18066, 2000.

Hussey, G. C., C. E. Meek, D. André, A. H. Manson, G. J. Sofko, C. M. Hall, C. M. A comparison of Northern Hemisphere winds using SuperDARN meteor trail and MF radar wind measurements, *Journal of Geophysical Research: Atmospheres (1984-2012), 105*(D14), 18053-18066, 2002.

Jackel, B. J., D. R. Moorcroft and K. Schlegel, Characteristics of very large aspect angle *E*-region coherent echoes at 933 MHz, *Annales Geophysicae , 15*(1), 54-62, 1997.

Jenkins, B. and M. J. Jarvis, Mesospheric winds derived from SuperDARN HF radar meteor echoes at Halley, Antarctica, *Earth Planets Space, 51*, 685-689, 1999.

Jones, J. and P. Brown, Sporadic meteor radiant distributions: orbital survey results, *Monthly Notices of the Royal Astronomical Society, 265*(3), 524-532, 1993.

Kelly, P. E., D. R. Hansen and P. A. Forsyth, The azimuthal distribution of ultra-high frequency radar echoes from aurora, *Canadian Journal of Physics, 39*(11), 1535-1543, 1961.

Kelley, M. C., The Earth's ionosphere: Plasma physics and electrodynamics, *International Geophysics Series*, vol 43. San Diego: Academic Press, 1989.

Kelley, M. C., The Earth's ionosphere: Plasma physics and electrodynamics, *Academic Press, 2nd Edition, 96*, 2009.

Kelley, M. C., M. Huaman, C. Y. Chen, C. Ramos, F. Djuth, and E. Kennedy, Polar mesosphere summer echo observations at HF frequencies using the HAARP Gakona Ionospheric Observatory, *Geophysical Research Letters, 29*, 12, 10.1029/2001GL013411, 2002.

Kivelson M. G. and C. T. Russell, Introduction to Space Physics, *Cambridge University Press*, Cambridge, 1995.

Kirkwood, S., V. Barabash, P. Chilson, A. Rechou, K. Stebel, P. Espy, G. Witt, and J. Stegman, The 1997 PMSE season - its relation to wind, temperature and water vapor, *Geophysical Research Letters, 25*, 1867-1870, 1998.

Kopp, E., P. Eberhardt, U. Herrmann and L. G. Börn, Positive ion composition of the high-latitude summer D region with noctilucent clouds, *Journal of Geophysical Research: Atmospheres (1984-2012, 90*(D7), 13041-13053, 1985.

La Hoz C., Radar scattering from dusty plasmas, *Physica Scripta, 45*(5), 529-534, 1992.

Larsen, M. F., A shear instability seeding mechanism for quasiperiodic radar echoes, *Journal of Geophysical Research: Space Physics (1978-2012), 105*(A11), 24931-24940, 2000.

Larsen, M. F., Winds and shears in the mesosphere and lower thermosphere: Results from four decades of chemical release wind measurements, *Journal of Geophysical Research: Space Physics (1978-2012), 107*(A8), SIA-28, 2002.

Lee, C. C., J. Y. Liu, C. J. Pan, and C. H. Liu, Doppler velocities obtained by the EISCAT VHF radar and the dynasonde during the PMSE95 campaign, *Journal of Atmospheric Solar-Terrestrial Physics, 63*(2- 3), 19-199, 2001.

Leslie, R. J., Sky glows, *Nature, 32*, 245, 1885.

Lindzen, R. S., Turbulence and stress owing to gravity waves and tidal breakdown, *Journal of Geophysical Research, 86*, 9707-9714, 1981.

Lübken, F. J., and U. von Zahn, Thermal structure of the mesosphere region at polar latitudes, *Journal of Geophysical Research, 96)*, D11, 20841-20857, 1991.

Lübken, F. J., Fricke, K. -H. and M. Langer, Noctilucent clouds and the thermal structure near the arctic mesopause, *Journal of Geophysical Research, 101*, 9489-9508, 1996.

Lübken, F. J., M. Zecha, J. Höffner, and J. Röttger, Temperatures, polar mesosphere summer echoes, and noctlilucent clouds over Spitsbergen (78°N), *Journal of Geophysical Research: Atmospheres (1984-2012) 109*(D11), 2004.

McKinley, D. W. R., Meteor science and engineering, *McGraw-Hill*, New York, 1961.

Milan, S. E., T. B. Jones, T. R. Robinson, E. C. Thomas, and T. K. Yeoman, Interferometer evidence for the observation of ground backscatter from behind the CUTLASS radars, *Annales Geophysicae, 15*, 29-39 1997a.

Milan, S. E., T. K. Yeoman, M. Lester, E. C. Thomas and T. B. Jones, Initial backscatter occurrence statistics from the CUTLASS HF radars, *Annales Geophysicae, 15*, No. 6, 703-718. Springer-Verlag, 1997b.

Milan, S. E. and M. Lester, Spectral and flow angle characteristics of backscatter from decameter irregularities in the auroral electrojets *Advanced Space Research, 23*, 1773-1776, 1999.

Milan, S. E., M. Lester, N. Sato, and H. Takizawa, On the altitude dependence of the spectral characteristics of decametre-wavelength *E*-region backscatter and the relationship with optical auroral forms, *Annales Geophysicae, 19*, No. 2, 205-217, 2001.

Milan, S. E. and M. Lester, A classification of spectral populations observed in HF radar backscatter from the *E*-region electrojets, *Annales Geophysicae, 19*, 189-204, 2001.

Milan, S. E., M. Lester, T. K. Yeoman, T. R. Robinson, M. V. Uspensky, and J. -P. Villain, HF radar observations of high-aspect angle backscatter from the *E*-region, *Annales Geophysicae, 22*, 829-847, 2004.

Moorcroft, D. R., An examination of radio-auroral aspect sensitivity, *Canadian journal of physics, 63*(7), 1005-1012, 1985.

Moorcroft, D. R., A statistical study of UHF auroral backscatter at large magnetic aspect angle: A reanalysis of unpublished results from 1968, *Journal of Geophysical Research: Space Physics (1978-2012), 101*(A5), 11005-11011, 1996.

Morris, R.J., D. J. Murphy, A. R. Klekociuk, D. A. Holdsworth, First complete season of PMSE observations above Davis, Antarctica, and their relation to winds and temperatures, *Geophysical Research Letters, 34*(5), L05805.1-L05805.5, 2007.

Nappo, C. J., An introduction to atmospheric gravity waves, *Academic Press, An Elsevier Science Imprint*, 2002.

Nussbaumer, V., Fricke, K. H., Langer, M., Singer, W., and Zahn, U. V., First simultaneous and common volume observations of noctilucent clouds and polar mesosphere summer echoes by lidar and radar, *Journal of Geophysical Research: Atmospheres (19842012), 101*(D14), 19161-19167, 1996.

Ogawa, T., N. F. Arnold, S. Kirkwood, N. Nishitani, and M. Lester, Finland HF and Esrange MST radar observations of polar mesosphere summer echoes, *Annales Geophysicae, 21*(4), pp 1047-1055, 1999.

Ogawa, T., N. Nishitani, N. Sato, H. Yamagishi, and A. S. Yukimatu, *Upper mesosphere summer echoes detected with the Antarctic Syowa HF radar*, Geophys. Res. Lett., 29(7), 10.1029/- 2001GL014094, 2002.

Ossakow, S. L. and P. K. Chaturvedi: Current convective instability in the diffuse aurora, *Geophysical Research Letters, 6*, 323, 1979.

Palmer, J. R., Rishbeth, H., Jones, G. O. L., and Williams, P. J. S., A statistical study of polar mesosphere summer echoes observed by EISCAT, *Journal of Atmospheric and Terrestrial Physics, 58*(1), 307-315, 1996.

Ponomarenko P. V., J. -P. St. Maurice , J. P. Waters, R. G. Gillies, A. V. Koustov, Refractive index effects on the scatter volume location and Doppler velocity estimates of ionospheric HF backscatter echoes, *Annales Geophysicae, 27*(11), 4207-4219, 2009.

Ponomarenko P. V., J. -P. St. Maurice , G. C. Hussey, A. V. Koustov, HF ground scatter from the polar cap: Ionospheric propagation and ground surface effects, *Journal of Geophysical Research, 115*(106), A10310, doi:10.1029/2010JA015828. 106, 2010.

Ponomarenko, P. V., A. V. Koustov, J. -P. St. Maurice and J. Wild, Monitoring the F region peak electron density using HF backscatter interferometry, *Geophysical Research Letters, 38*, No. 21, 2011.

Ponomarenko, P. V., B. Iserhienrhien, J.-P. St. Maurice, Morphology and possible origins of near-range HF backscatter at high and mid latitudes, *Journal of Geophysical Research*, Under Review, 2015.

Rapp, M., B. Strelnikov, A. Müllemann, F.-J. Lübken, and D. C. Fritts, Turbulence measurements and implications for gravity wave dissipation during the macwave/midas rocket program, *Geophysical Research Letters, 31*(24), doi:10.1029/2003GL019325, 2004.

Rapp, M., and G. E. Thomas, Modeling the microphysics of mesospheric ice particles: Assessment of current capabilities and basic sensitivities, *Journal of Atmospheric and Solar-Terrestrial Physics, 68*, 715-744, 2006.

Ribeiro, A. J., J. M. Ruohoniemi, P. V. Ponomarenko, L. B. Clausen, J. B. Baker, R. A. Greenwald, K. Oksavik and S. de Larquier, A comparison of SuperDARN ACF fitting methods. Radio Science, *Radio Science, 48*(3), 274-282, 2013.

Röttger, J., C. La Hoz, M. C. Kelley, U. P. Hoppe, and C. Hall, The structure and dynamics of polar mesosphere summer echoes observed with EISCAT 224 MHz radar, *Geophysical Research Letters, 15*, 1353-1356, 1988.

Röttger, J., M. T. Rietveld, C. La Hoz, T. Hall, M. C. Kelley, and W. E. Swartz, Polar mesosphere summer echoes observed with the EISCAT 933-MHz radar and the CUPRI 46.9-MHz radar, their similarity to 224-MHz radar echoes and their relationship to turbulence and electron density profiles, *Radio Science, 25*, 671-687, 1990.

Röttger, J., Polar mesosphere summer echoes: Dynamics and aeronomy of the mesosphere, *Advances in Space Research, 14*(9), 123-137, 1994.

Rüster, R. and K. Schlegel, Non-magnetic aspect sensitive auroral echoes from the lower E region observed at 50 MHz, *Journal of Geophysical Research: Space Physics, 17*(10), 1284-1292, 1999.

Schlegel, K., Measurements of electron density fluctuations during the ROSE rocket flights, *Journal of atmospheric and terrestial physics, 54*(6), 715-723, 1992.

Schlegel, K., Coherent backscatter from ionospheric E-region plasma irregularities, *Journal of Atmospheric and Terrestrial Physics, 58*, 933-941, 1996.

Schlegel, K. and A. V. Gurevich, Radar backscatter from plasma irregularities of the lower E-region induced by neutral turbulence, *Annales Geophysicea, 15*, 870-877, 1997.

Schunk R.W. and A.F. Nagy, Ionospheres, physics, plasma physics and chemistry, *Cambridge Atmospheric and Space Science Series*, 2000.

Scoular G., P. V. Ponomarenko, J.-P. St.-Maurice, A new type of Doppler velocity fluctuations in HF ground scatter from the polar cap, *Geophysical Research Letters, 40*(19), 4992-4997, 2013.

Singer, W., U. von Zahn, and J. Weiß, Diurnal and annual variations of meteor rates at the arctic circle, *Atmospheric Chemistry and Physics, 4*(5), 1355-1363, 2004.

Singer, W., Bremer, J., Weiβ, J., Hocking, W. K., Höffner, J., Donner, M., and Espy, P, Diurnal and annual variations of meteor rates at latitudes between 69 N and 35 S. In 17th ESA Symposium on European rocket and balloon programmes and related research, *In*

17th ESA Symposium on European Rocket and Balloon Programmes and Related Research, 590, 151-156, 2005.

Singer, W., R. Latteck, L. F. Millan, N. J. Mitchell, , J. Fiedler, Radar backscatter from underdense meteors and diffusion rates, *Earth, Moon and Planets, 102*(1-4), 403-409, 2008.

St Maurice, J. -P. and A. M. Hamza, Small scale irregularities at high latitudes. In "characterising the ionosphere", *Technical Report RTO-TR-IST-051, ed. G. Wyman*, 2009. Neuilly-sur-Seine, France: RTO. Available from: http://www.rto.nato.int/abstracts.aspx .

St Maurice, J. -P. and A. M. Hamza, A new nonlinear approach to the theory of E region irregularities, *Journal of Geophysical Research: Space Physics (1978-2012) 106)*(A2), 1751-1759, 2001.

Sudan, R. N., J. Akinrimisi, and D. T. Farley, Generation of small-scale irregularities in the equatorial electrojet, *Journal of Geophysical Research, 78*, 1, 240-248, 1973.

Sudan, R. N. Nonlinear theory of type I irregularities in the equatorial electrojet, *Geophysical Research Letters, 10*(10), 983-986, 1983a.

Sudan, R. N., Unified theory of type I and type II irregularities in the equatorial electrojet, *Journal of Geophysical Research: Space Physics, (1978-2012), 88*(A6), 4853-4860, 1983b.

Szasz, C. J. Kero, A. Pellinen-Wannberg, J. D. Matthews, N. J. Mitchell and W. Singer, Latitudinal variations of diurnal meteor rates, *Earth, Moon, and Planets, 95*(1-4), 101-107, 2005.

Thomas, R. M, P. S. Whitham, W. G. Elford, Response of high frequency radar to meteor backscatter, *Journal of Atmospheric and Terrestrial Physics, 50*, 703-724, 1988.

Tsunoda, R. T., High-latitude F region irregularities: A review and synthesis, *Reviews of Geophysics, 26*, 4, 719-760, 1988.

Tsutsumi, M., A. S. Yukimatu, D. A. Holdsworth, and M. Lester, Advanced SuperDARN meteor wind observations based on raw time series analysis technique, *Radio Science, 44*(2), RS2006, http://dx.doi.org/10.1029/2008RS003994, 2009.

Vlaskov, V. A., E. Turunen, and A. A. Bogolubov, Investigation of PMSE characteristics by partial reflection radar at 2.7 MHz, *Paper GAB51F-01, presented by IUGG XXI General Assembly, Boulder, Colorado*, 1995.

Villain, J.-P., R.A. Greenwald, K.B. Baker, and J.M. Ruohoniemi, HF radar observations of E region plasma irregularities produced by oblique electron streaming, *Journal of Geophysical Research, 92*(12), 327-12,342, 1987.

Wallace, J. M., and P. V. Hobbs, Atmospheric science: an introductory survey *Academic press*, vol. 92, 2006.

Wayne, R. P., Chemistry of atmospheres, an introduction to the chemistry of the atmospheres of Earth, the planets and their aatellites, *Oxford University Press*, Second Edition, 1991.

Weiss, A. A., J. W. Smith, E. G. and Bowen, A southern hemisphere survey of the radiants of sporadic meteors, *Monthly Notices of the Royal Astronomical Society, 121*(1), 5-16, 1960.

Witt, G., Height, structure and displacements of noctilucent clouds, *Tellus, 14*, 1-18, 1962.

Younger, P. T., I. Astin, D. J. Sandford and N. J. Mitchell, The sporadic radiant and distribution of meteors in the atmosphere as observed by VHF radar at Arctic, Antarctic and equatorial latitudes, *Annales. Geophysicae, 27*(7), 2831-2841, 2009.

Yukimatu, A.S. and M. Tsutsumi, A new SuperDARN meteor wind measurement: Raw time series analysis method and its application to mesopause region dynamics, *Geophysical Research Letters, 29*(20), 1981, 2002 doi: 10.1029/2002GL015210. Also see Correction, Yukimatu, A. S. and Tsutsumi, M. (2002), *Geophysical Research Letters, 30*(1), doi: 10.1029/2002GL016560.

Yukimatu, A.S., Correction to "A new SuperDARN meteor wind measurement: Raw time series analysis method and its application to mesopause region dynamics", by Akira Sessai Yukimatu and Masaki Tsutsumi, *Geophysical Research Letters, 30*(1), 2003.

Zecha, M., J. Röttger, W. Singer, P. Hoffmann and D. Keuer, Scattering properties of PMSE irregularities and refinement of velocity estimates, *Journal of Atmospheric and Solar-Terrestrial Physics, 63*(2), 201-214, 2001.

Zecha, M. and J. Röttger, Occurrence of polar mesosphere summer echoes at very high latitudes, *Annales Geophysicae, 27*(3), 1331-1342, 2009. Copernicus GmbH.